Bottom-Up Synthesis of MnO_2 Nanosheets and Applications to Functional Nanocomposites

Kazuya Kai

2012

PREFACE

The present thesis is a compilation of studies on the "Bottom-Up Synthesis of MnO_2 Nanosheets and Applications to Functional Nanocompoistes" which were carried out by the author under the supervision of Professor Hiroshi Kageyama at the Department of Energy and Hydrocarbon Chemistry, Graduate School of Engineering, Kyoto University during 2008−2012.

This work is indebted to the continuous help of many researchers. The author would like to express his deepest thanks and sincere gratitude to Professor Hiroshi Kageyama for cheerful and continuous guidance, precious suggestions, fruitful discussion throughout this work, and for providing him a prime opportunity to study as a Ph.D student.

The author is also deeply grateful to Professor Gunzi Saito, and Dr. Yukihiro Yoshida (Research Institute, Meijo University), whose fruitful discussion and comments were of great value for this work. The author's heartfelt appreciation goes to Dr. Yoji Kobayashi (Graduate School of Engineering, Kyoto University) for his dedicated guidance and discussion.

The author would like to acknowledge Professor Takeshi Abe, (Kyoto University), Professor Yoshiharu Uchimoto (Kyoto University), Dr. Kohei Miyazaki (Kyoto University), and Dr. Yuki Yamada (Tokyo University) for their helpful suggestions and discussion.

The author also wishes to thank Professor Jun Kawamata (Yamaguchi University) and his laboratory members, in particular Mr. Tetsuo Ishigaki and Mr. Yu Furukawa for their contribution to this work.

The author would like to express his gratitude to Professor Hideki Yamochi (Kyoto University) and his laboratory members, especially Dr. Yoshiaki Nakano, Dr. Manabu Ishikawa, and Dr. Takaaki Hiramatsu.

It remains to the author to thank all the members of Professor Kageyama's laboratory for their hearty support and encouragement. A special debt of gratitude goes to the author's colleagues: Dr. Yoshitami Ajiro, Dr. Takeshi Yajima, Dr. Yoshihiro Tsujimoto, Dr. Ryo Horikoshi, Mr. Atsushi Kitada, Mr. Takafumi Yamamoto, Mr. Tatsunori Sakaguchi, Mr. Takashi Watanabe, Mr. Yuji Sumida, Mr.

Fumitaka Takeiri, Mr. Masatoshi Okura, Mr. Shingo Mitsuoka, Mr. Shota Kawasaki, Mr. Koshiko Masaki, Mr. Hajime Suzuki, Mr. Ryuta Yoshii, Mr. Kousuke Nakano, Mr. Kei Asai, Mr. Naoyuki Abe, Dr. Cedric Tassel, Dr. G. Subodh, Ms. Liis Seinberg, Mr. Guillaume Bouilly, and Ms. Asako Okumiya.

The author would like to thank the Global COE program “Integrated Materials Science”, and Research Fellowships of JSPS for Young Scientists for the financial support during student life.

Finally, the author wishes to express his special thanks to his parents for their warm encouragement and deep understanding toward accomplishing this work.

Kazuya Kai

Kyoto, Japan

March 2012

Contents

General Introduction

Background of the work

1. Low-Dimensional Materials; Fundamental Interests and Applications.

Two-dimensional (2D) layered materials have attracted intense research interests in both the fundamental and industrial applications. For example, the layered inorganic materials such as cuprates,[1] and $[CuCl]LaNb_2O_7$[2] exhibit unusual physical properties (e.g. high-temperature superconductivity[1] and spin-liquid,[2] respectively) relating to the quantum fluctuation enhanced by low-dimensional electronic structures. For application example of 2D-systems, the giant magnetoresistance (GMR) devises comprised of alternately stacked 2D ferromagnetic(Fe)/nonmagnetic(Cr) superlattices[3] are applied in magnetic heads in hard disk drives, and facilitate increase in storage capacity of memories.

2. New Class of 2D-Materials; Exfoliated Inorganic Nanosheets

The other example of the 2D material is not a layered compound, but an exfoliated material. Recently, exfoliated graphite, so called "graphene",[4] which is a strictly 2D material consisted of flat

monolayer of carbon atoms tightly packed into a two-dimensional (2D) honeycomb lattice has triggered keen interest due to their unique physical properties (e.g. quantum hall effect,[5] and massless Dirac fermions behavior,[6] etc.) completely differed from the bulk graphite. Except for graphene, a wide variety of ultra-thin films (~ 1 nm in thickness) consisted of exfoliated inorganic layered compounds, so-called "nanosheets" are obtained via soft-chemical ion-exchange reaction using various layered inorganic compounds (e.g., $RbCa_2Nb_3O_{10}$, K_xMnO_2, $Al_{1/3}Mg_{2/3}(OH)_2 \cdot 1/3NO_3$, etc.)[7] (Figure 1a). These nanosheets are obtained as colloidal suspensions reflecting their charge-bearing nature, and characterized by uniform thickness defined by crystal structure of the primary inorganic host layers (Figure 1b). The charge-bearing and colloidal natures of the nanosheets allow to construct several nanostructures (e.g., randomly-stacked structure, thin film, multilayered thin film or heterostructure, etc.) or layered organic/inorganic hybrids through the electrostatic interactions.[7b,7c] Such electrostatic aspects of the nanosheets enable the build-up of new functional materials consisting of 2D building blocks, by means of low-cost and low-energy procedures.

3. Historical Background of the Nanosheets

The exfoliation phenomena of the layered inorganic compounds have been known for clay minerals (montmorillonite, hectorite, and saponite, etc.) from 1950s.[8] The exfoliation mechanism was understood as infinite-interlayer expansion through volume increased phase (Osmotic swelling phase), which is induced by intercalation of large excess amount of solvent molecules (Figure 2).[9] Such solvent (H_2O) intercalation and swelling are only observed for the layered inorganic compounds with very weak interlayer interaction. Thus, in the past, it is considered that the exfoliation phenomena are characteristic natures of the clay minerals because of their very low layer charge density.

To exfoliate the other layered compounds except for clay minerals, the controlling of the interactions between interlayer cations, solvents, and host layeres are essentially required. Since 1970s, exfoliation of a wide range of inorganic layered compounds, including layered metal chalcogenides, phosphates, oxides, and layered double hydroxides (LDHs) have been achieved through an appropriate combination of interlayer cations and solvents (see Table 1). For example,

$Ca_2Na_{n-3}Nb_nO_{3n+1}$ (n = 3, and 4) nanosheets are obtained via exfoliation using alkylammonium (as exfoliating reagent) and butanol (as solvent).[40] Other examples are shown in Table 1. These appropriate combinations are different from each compound, and lack versatility.

More versatile exfoliation method for other layered inorganic compounds was accomplished by Keller *et al.* in 1994,[16] and fundamental study of this exfoliation mechanism are examined by Sasaki *et al.*, in detail.[10a] The schematic diagram of the multi-step reaction is shown in Figure 3. The remarkable points of this method are as follows; 1) ion-exchange reaction (acid-base reaction) between interlayer cations and basic organic cations and 2) the utilization of ternary alkylammonium ions as exfoliating reagents. Here, the interlayer H^+ ions of the acidified samples are exchanged with ternary alkylammonium ions. This ion-exchange reaction is facilitated by acid-base reaction (e.g., eliminated interlayer H^+ ions are trapped by OH^- ions in solution). Furthermore, the positive charge on N^+ of intercalated ternary alkylammonium ions are shielded by aklylchains, and allow to decrease the coulombic interaction between negative host layer and positive organic cations. Such a decrease in interaction between interlayer cations and host layers destabilizes the layered structure, and facilitates the exfoliation reaction. Almost all of exfoliations of the transition metal oxide nanoshees have been achieved by this multi-step process. However, this process requires at least 3-reaction steps including the synthesis of mother compound (template), protonation, and acid-base reactions. This strategy results in the long-reaction times (up to several weeks to 1 month) and low yields (typically 30 % ~ 40%; non-exfoliated materials are involved as impurity).

All of nanosheets obtained by exfoliation of layered metal chalcogenides, phosphates, and oxides are negatively charged, while the positively charged nanosheets are only known for the nanosheets obtained via exfoliation of layered double hydoroxides ($Mg_{2/3}Al_{1/3}(OH)_2 \cdot 1/3NO_3$, etc.).[56-63] The exfoliation of LDHs is also achieved via multi-step ion-exchange reactions, however, the exfoliation mechanism of LDHs is still unclear.

4. Application of the Nanosheets

Nanosheets possess a wide range of functionalities. So far, several functional metal oxide nanosheets, such as photocatalytic (TiO_2,[10a] Nb_6O_{17},[11] $LaNb_2O_7$,[12] $Ca_2Nb_3O_{10}$,[10b] etc.), acid-catalytic (Nb_3O_8,[11] $TiNbO_5$,[13] Ti_2NbO_7,[14] $TaWO_6$[15] ,etc.), electron conductive (RuO_2, MoO_3),[16,17] redoxable

(RuO_2, MnO_2),[18,19] ferromagnetic ($Co_{0.2}Ti_{0.8}O_2$,[20a] $Fe_{0.2}Ti_{0.8}O_2$,[20a] $Ti_{(5.2-2x)/6}Mn_{x/2}O_2$[20b]), dielectric($TiO_2$,[21a] $Ca_2Nb_3O_{10}$,[21b] etc.), photochromic ($W_{11}O_{36}$),[22] and fluorescent ($Eu_{0.56}Ta_2O_7$,[23] $La_{2/3-x}Eu_xTa_2O_7$,[24] $Sm_{0.05}Nb_2O_7$[25]) nanosheets have been obtained (Figure 4). Such functional nanosheets can improve their properties via regulation of suitable nanostructures.

Nanosheets can provide considerably large specific surface areas reflecting its ultra-thin nature, therefore they have potential applications to the high-efficient catalysis or electrode materials because these reaction efficiencies were strongly affected by catalytically and electrochemically active surface area.[13,26–28] When the cationic species (e.g. alkali metal or organic cations, etc.) are added into the transition metal oxide nanosheet suspensions, the nanosheets are stacked electrostatically and form lamellar aggregates as precipitates. These restacked materials exhibit mesoporous structures and increased specific surface areas.[13] Especially, mesopores facilitate transport of ions and molecules, hence the reaction rate of catalytic or electrochemical reaction can be improved effectively.

Ebina *et al.* fabricated restacked material of $K^+/Ca_2Nb_3O_{10}$ by addition of K^+ ions into photocatalytic $Ca_2Nb_3O_{10}$ nanosheets suspensions, and reported their enhanced photocatalytic activities of about 5 times faster H_2 gas evolution rate compared with non-exfoliated $KCa_2Nb_3O_{10}$ (Figure 5).[26] Wang *et al.* studied electrochemical performances of lamellar aggregate Li^+/MnO_2, and revealed that the obtained lamellar aggregates exhibited good cycling performances with high discharge capacity comparable to the theoretical capacity of $LiMnO_2$.[27] And also, Sugimoto *et al.* obtained supercapacitor electrode using electronic conductive RuO_2 nanosheets, and reported their large capacitance (660 F/g) with high rate capabilities; this capacitance is about 3 times larger than conventional supercapacitor electrodes consisted of activated carbons (Figure 6).[31] These reports indicates that the stacked nanosheets can effectively utilize their surface for catalytic or electrochemical reactions.

The constant thickness, charge bearing and colloidal natures of the nanosheets enable to make thin film or multilayer assembly using low-cost and low-energy solution processes; electrostatic deposition (ED) [14] and Langmuir-Blodget (LB)[29] methods are representative (Figure 7). The ED method is conducted by alternate dipping of substrate in nanosheets suspensions and aqueous solution of polyelectrolytes (Figure 7a). This method is facile and speedy, and does not require any special apparatus. On the other hand, LB method transfers monolayer film formed on air-water

interface (LB film) to the substrate (Figure 7b). In terms of the controllability of packing density of the nanosheets by surface pressure, more smooth and atomically uniform nanosheets thin film with high dense characteristic can be obtained by this method (Figure 8). In principle, both solution processes can regulate their thickness and stacking sequences by stepwise controlling of the film growths.[7c,20a,21b] The obtained nanoarchitecture can possess several functions. For example, transparent electron-conductive film was obtained via electrostatic deposition of RuO_2 nanosheets on SiO_2 substrate.[13] High- κ dielectric capacitors with high capacity and low leak current are provided by LB deposited insulating $Ca_2Nb_3O_{10}$ nanosheets on $SrRuO_3$ substrate.[21] Furthermore, ferromagnetic thin films are achieved by electrostatic-deposited ferromagnetic $Ti_{0.8}Co_{0.2}O_2$ nanosheets on SiO_2. For familiar examples, a glass window coated by TiO_2 nanosheets is applied in stain-resistant hydrophilic windows.[30]

The layer-by-layer assembly using various kinds of nanosheets allows forming the multilayered heterostructure with precisely controlled stacking sequences and film thicknesses. This feature explores controllable physical properties depending on superlattice structure. Sakai *et al.* made a heterostructure thin film through the electrostatic sequential deposition of TiO_2 and MnO_2 nanosheets, and revealed that there is photo induced charge transfer between TiO_2 and MnO_2 layers. The charge transfer rate was dependent on the stacking sequences.[31] Osada *et al.* investigated the ferromagnetic properties of the heterostructure thin film composed of $Ti_{0.8}Co_{0.2}O_2$ and $Ti_{0.6}Fe_{0.4}O_2$ by means of magnet circular dichromism (MCD) spectroscopy, and the MCD response was increased by up to 30 times depending on stacking sequence.[20a] There is magnetic interaction between the stacked nanosheets. These results demonstrate that the heterostructures and their functionalities can be rationally designed through the selection of nanosheets and the combination with heterogeneous species, with precise control over the artificial arrangement at a molecular scale.

Outline of the Work

In Chapter 1, the bottom-up one-pot synthesis of the MnO_2 nanosheets is presented. MnO_2 nanosheets suspensions were prepared via chemical oxidation of $MnCl_2$ using H_2O_2, in the presence of tetramethylammonium cations in aqueous solution. The structure and physical properties of MnO_2

nanosheets and their lamellar aggregates are analyzed in detail. It is revealed that the obtained MnO_2 nanosheets have same structures and characteristics for the nanosheets obtained by exfoliation of layered manganese oxide, K_xMnO_2. The author demonstrated that the MnO_2 nanosheets can be obtained at room temperature, in short reaction time and high yield through simple one-pot method.

In Chapter 2, Co substituted manganese oxide nanosheets, $(Mn_{1-x}Co_x)O_2$ have been synthesized via a simple one-pot method. The substitution effects on the structural, photo absorption, and magnetic properties of the nanosheets and their lamellar aggregates are investigated. The formation of $(Mn_{1-x}Co_x)O_2$ nanosheets were confirmed by AFM, SEM, and XRD, and the solubility limit was deduced that $x \sim 0.20$. The magnetic moments of these lamellar aggregates $K_y(Mn_{1-x}Co_x)O_2 \cdot zH_2O$ are consistent with chemical compositions estimated by EDS. From the variation of magnetic moments and chemical compositions, the author concluded that the average valence of transition metal ions is insensitive to the substitution, and this indicates that the the charge density of inorganic layer is inert upon Co-for-Mn substitution.

In Chapter 3, *n*-butylammonium/MnO_2 layered hybrid was synthesized via simple one-pot method, and its reaction mechanism was investigated in detail. The reaction methodology was hinted at by bottom-up one-pot approach to access MnO_2 nanosheets (e.g., this one-pot synthesis uses a primary amine in place of the quaternary ammonium salt). Through the structural, spectroscopic, and pH analysis, it is revealed that reaction mechanism involves following 3 reaction steps: (1) formation and crystal growth of β-Mn(III)OOH, (2) topotactic oxidation of β-MnOOH to form the protonated layered manganese oxide $H_xMnO_2 \cdot yH_2O$, and (3) ion-exchange of interlayer H^+ (or H_3O^+) with *n*-butylammonium and formation of layered C4/MnO_2. Such a feature is reasonable to assume the formation mechanism of the MnO_2 nanosheets due to the similarity in synthetic method.

In Chapter 4, the first viscoelastic nanocomposite composed of negatively charged MnO_2 nanosheets was fabricated by a room-temperature one-pot process. The nanocomposite can be easily deformed by applying an external stress; for example, mechanical stress gives a free-standing thin film with a thickness of less than 100 nm. The rheological character of the composite was investigated by frequency dependence of shear-loss moduli, and dynamic viscosity, and the results

are consistent with the viscoelastic character of the composite. The ionic conductivity and its activation energy of the composite increases and decreases respectively, with relative humidity increase; it is indicative of the Grotthuss-like proton conduction, and it is associated with the water network formed near the acidic MnO_2 surfaces. The structure of the composite is analyzed by XRD and IR in detail, and revealed that the composite are composed of layered nanocomposites consisted of MnO_2 layer and surface-attached organo-siloxane groups on it, and these nanocomposite slabs are connected with each other though van der Waals interaction of surface alkylchaines. It appears that (i) a trimethoxysilyl group and (ii) double long alkyl groups (both for reducing inter-slab interactions) are indispensable for obtaining the viscoelastic nanocomposite in the present system. By the aid of (iii) a quaternized ammonium group (for charge compensation), the present procedure would open up an exploration of new and more versatile viscoelastic nanocomposites composed of negatively charged transition metal oxide nanosheets with a wide variety of metal elements, intralayer structures, and compositions.

In Chapter 5, MnO_2/carbon nanocomposite comprised of single-layer MnO_2 nanosheets and acetylene black (AB) was assembled by simply mixing of MnO_2 nanosheets colloidal suspension and AB suspensions. MnO_2 nanosheets were synthesized by one-pot procedure, and adsorbed on AB aggregates as a single-layer (monosheets) through the electrostatic interactions. The XRD of the MnO_2/AB composite only exhibited in-plane reflections of MnO_2 sheet and peaks originated from AB, and demonstrated that the MnO_2 nanosheets were adsorbed onto the AB surface as single-layer. SEM and TEM measurements showed that the lateral sizes of MnO_2 nanosheets are larger than the sizes of AB aggregates, and MnO_2 sheets are covered over the outer surface of AB aggregates. The galvanostatic charge-discharge measurement and cyclic voltammetry taken in organic electrolyte demonstrate that the MnO_2/AB composite exhibits an excellent specific capacity and capacitance of 400 mAh/g and 739 F/g at a current density of 10 μ A/cm^2 and a scan rate of 1 mV/s, respectively. The obtained large specific capacity can be associated with high yield character of the one-pot process, which can utilize the nanosheet surface for charge-storage more effectively.

References

[1] (a) Park, C.; Snyder, R. L. *J. Am. Chem. Soc.* **1995**, *78*, 3171. (b) Muller-Buschbaum, H. K. *Angew. Chem. Int. Ed.* **1989**, *28*, 1472. (c) Sleight, A. W. *Science* 1**988**, *242*, 1519.

[2] (a) Kageyama,H.; Yasuda J.; Kitano, T.; Totsuka, K.; Narumi, Y.; Hagiwara, M.; Kindo, K.; Baba, Y.; Oba, N.; Ajiro, Y.; Yoshimura, K. *J. Phys. Soc. Jpn.* **2005**, *74*, 3155. (b) Kageyama, H.; Kitano, T.; Oba, N.; Nishi, M.; Nagai, S.; Hirota, K.; Viciu, L.; Wiley, J. B.; Yasuda, J.; Ajiro, Y.; Yoshimura, K. *J. Phys. Soc. Jpn.* **2005**, *74*, 1702.

[3] Baibich, M. N.; Broto, J. M.; Fert, A.; Nguyen V. D. F.; Petroff, F.; Eitenne, P.; Creuzet, G.; Friederich, A.; Chazelas, J. *Phys. Rev. Lett.* **1988**, *61*, 2472.

[4] (a) Novoselov, K. S.; Geim, A. K.; Morozov, S. V.; Jiang, D.; Zhang, Y.; Dubonos, S. V.; Grigorieva, I. V.; Firsov, A. A. *Science*, **2004**, *306*, 666. (b) Geim, A. K.; Novoselov, K. S. *Nature*, **2007**, *6*, 183.

[5] Zhang, Y.; Tan, J. W.; Stormer, H. L.; Kim, P *Nature* **2005**, *438*, 201..

[6] Novoselov, K. S. *Nature* **2005** *438*, 197.

[7] (a) Schaak, R. E.; and Mallouk, T. E. *Chem. Mater.* **2002,** *14,* 1455. (b) Sasaki, T. *J. Ceram. Soc. Jpn.* **2007,** *115,* 9. (c) Osada, M.; Sasaki, T. *J. Mater. Chem.* **2009,** *19*, 2503.

[8] Norrish, K. Disscuss. *Faraday Soc.* **1954**, *18*, 120.

[9] Blackmore, A. V.; Warkentin, B. P. *Nature* **1960**, *186*, 823.

[10] (a) Sasaki, T.; Watanabe, M.; Hashizume, H.; Yamada, H.; Nakazawa, H. *J. Am. Chem. Soc.* **1996,** *118,* 8329. (b) Ebina, Y.; Sasaki,T.; Watanabe, M. *Solid State Ionics* **2002,** *151,* 117.

[11] Nakato, T.; Miyamoto, N.; Harada, A. *Chem. Comm.* **2004**, *1*, 78.

[12] Maeda, K.; Mallouk, T. E. *J. Mater. Chem.* **2009**, *19*, 4813.

[13] Takagi, A.; Yoshida, T.; Lu, D.; Kondo, J. N.; Hara, M.; Domen, K.; Hayashi, S. *J. Am. Chem. Soc.* **2003,** *125,* 5479.

[14] Keller, S. W.; Kim, H-N.; Mallouk, T. E. *J. Am. Chem. Soc.* **1994,** *116,* 8817.

[15] Li, X.-L.; Lin, B.-Z.; Xu, B.-H.; Chen, Z.-J.; Wang, Q.-Q.; Kuang, J.-D.; Zhu, H. *J. Mater. Chem.* **2010**, *20*, 3924.

[16] Sato, J.; Kato, H.; Kimura, M.; Fukuda, K.; Sugimoto, W. *Langmuir* **2010,** 26, 18049.

[17] Oh, E-J.; Kim, T. W.; Lee, K. M.; Song, M-S.; Jee, A-Y.; Lim, S. T.; Ha, H-W.; Lee, M.; Choy, J-H.; Hwang, S-J. *ACS Nano* **2010**, *8*, 4437.

[18] Fukuda, K.; Saida, T.; Sato, J.; Yonezawa, M.; Takasu, Y.; Sugimoto, W. *Inorg. Chem.* **2010,** *49,*

4391.

[19] Liu, Z-h.; Ooi, K.; Kanoh, H.; Tang, W-p.; Tomida, T. *Langmuir* **2000,** *16,* 4154.

[20] (a) Osada, M.; Ebina, Y.; Takada, K.; Sasaki, T. *Adv. Mater.* **2006**, *18*, 295. (b) Dong, X.; Osada, M.; Ueda, H.; Ebina, Y.; Kotani, Y.; Ono, K.; Ueda, S.; Kobayashi, K.; Takada, K.; Sasaki, T. *Chem. Mater.* **2009,** *21,* 4366.

[21] (a) Osada, M.; Ebina, Y.; Funakubo, H.; Yokoyama, S.; Kiguchi, K.; Sasaki, T. *Adv. Mater.* **2006**, *18*, 1023. (b) Osada, M.; Akatsuka, K.; Ebina, Y.; Funakbo, H.; Ono, K.; Takada, K.; Sasaki, T. *ACS Nano*, **2010,** *4,* 5225.

[22] Fukuda, K.; Akatsuka, K.; Ebina, Y.; Ma, R.; Takada, K.; Nakai, I.; Sasaki, T. *ACS Nano*, **2008,** *8,* 1689.

[23] Ozawa, T. C.; Fukuda, K.; Akatsuka, K.; Ebina, Y.; Sasaki, T.; Kurashima, K.; Kosuda, K. *J. Phys. Chem. C*, **2008**, 112, 1312.

[24] Ozawa,T. C.; Fukuda, K.; Akatsuka, K.; Ebina,Y.; Sasaki,T.; Kurashima, K.; Kosuda, K. *J. Phys. Chem. C* **2008**, *112*, 1312.

[25] Ozawa, T. C.; Fukuda, K.; Ebina, Y.; Kosuda, K.; Sato, A.; Michiue, Y.; Kurashima, K.; Sasaki, T. *Sci. Technol. Adv. Mater.* **2011**, *12*, 044601.

[26] Ebina, Y.; Sasaki, T.; Harada, M.; Watanabe, M. *Chem. Mater.* **2002,** *14,* 4390.

[27] Wang, L.; Takada, K.; Kajiyama, A.; Onoda, M.; Michiue, Y.; Zhang, L.; Watanabe, M.; Sasaki, T. *Chem. Mater.* **2003,** *15,* 4508.

[28] (a) Sugimoto, W.; Iwata, H.; Yasunaga, Y.; Murakami, Y.; Takasu, Y. *Angew. Chem. Int. Ed.* **2003,** *42*, 4092.

[29] Muramatsu, M.; Akatsuka, K.; Ebina, Y.; Wang, K.; Sasaki, T.; Ishida, T.; Miyake, K.; Haga, M-a. *Langmuir* **2005,** *21,* 6590.

[30] Shichi, T.; Katsumata, K-h. *Hyoumengijutsu* **2010,** *61,* 30.

[31] Sakai, N.; Fukuda, K.; Omomo, Y.; Ebina, Y.; Takada, K.; Sasaki, T. *J. Phys. Chem. C* **2008,** *112,* 5197.

[32] Murphy, D. W.; Hull Jr, G.W. *J. Chem. Phys.* **1975**, *62*, 973.

[33] Leaf, A.; Schöllhorn, R. *Inorg. Chem*. **1977**, *16*, 2950.

[34] Joensen, P.; Frindt, R. F.; Morrison, S. R. *Mater. Res. Bull*. **1986**, *21*, 457.

[35] Alberti, G.; Casciola, M.; Costantino, U. *J. Colloid Interface Sci.* **1985**, *107*, 256.

[36] Yamamoto, N.; Okuhara, T.; Nakato, T. *J. Mater. Chem.* **2001**, *11*, 1858.

[37] Okamoto, Y.; Ida, S.; Hyodo, J.; Hagiwara, H.; Ishihara, T. *J. Am. Chem. Soc.* **2011**, *133*, 18034.

[38] Abe, R.; Shinohara, K.; Tanaka, A.; Hara, M. Kondo, J.N.; Domen, K. *J. Mater. Res*. 1998, *13*, 861.

[39] Harada, M.; Sasaki, T.; Ebina, Y.; Watanabe, M. *J. Photochem. Photobiol. A: Chem*. **2002**, *148*, 273.

[40] Tanaka, T.; Ebina, Y.; Takada, K.; Kurashima, K.; Sasaki, T. *Chem. Mater.* **2003**, *15*, 3564.

[41] Miyamoto, N.; Kuroda, K.; Ogawa, M. *J. Mater. Chem.* **2004**, *14*, 165.

[42] Treacy, M. M. J.; Rice, S. B.; Jacobson, A. J.; Lewandowski, J. T. *Chem. Mater*. **1990**, *2,* 279.

[43] Takagi, A.; Yoshida, T.; Lu, D.; Kondo, J. N.; Hara, M.; Domen, K.; Hayashi, S. *J. Phys. Chem. B* **2004**, *108*, 11549.

[44] Ida,S.; Ogata,C.; Eguchi, M.; Youngblood, W. J.; Mallouk, T. E.; Matsumoto, Y. *J. Am. Chem. Soc.* **2008**, *130*, 7052.

[45] Ozawa, T.C.; Fukuda, K.; Akatsuka, K.; Ebina, Y.; Kurashima, K.; Sasaki, T. *J. Phys. Chem. C* **2009**, *113*, 8735.

[46] Leroux, F.; Adachi-Pagano, M.; Intissar, M.; Chauvière, S.; Forano, C.; Besse, J-P. *J. Mater. Chem*. **2001**, *11*, 105.

[47] Nazar, L. F. ; Liblong,S. W.; Yin, X. T. *J. Am. Chem. Soc.* **1991**, *113*, 5889.

[48] Kim, D. S.; Ozawa, T. C.; Fukuda, K.; Ohshima, S.; Nakai, I.; Sasaki, T. *Chem. Mater.* **2011**, *23*, 2700.

[49] Varoon, K.; Zhang, X.; Elyassi, B.; Brewer, D. D. ; Gettel, M.; Kumar, S.; Lee, J. A.; Maheshwari,S.; Mittal, A.; Sung, C.-Y.; Cococcioni, M.; Francis, L. F.; McCormick, A. V.; Mkhoyan, K. A.; Tsapatsis, M. *Science* **2011**, *334*, 72.

[50] Hibino, T.; Jones, W. *J. Mater. Chem*. **2001**, *11,*1321.

[51] Singh, M.; Ogden, M. I.; Parkinson, G. M.; Buckley, C. E.; Connolly, J. *J. Mater. Chem.* **2004**, *14,* 871.

[52] Brock, S. T.; Sanabria, M.; Suib, S. L. *J. Phys. Chem. B* **1999**, *103*, 7416.

[53] Ozge, A.; Unal, U.; Ida, S.; Goto, M.; Matsumoto, Y *J. Solid State Chem.* **2008**, *181,* 3257.

[54] Liang, J.; Ma, R.; Iyi, R.; Ebina, Y.; Takada, K.; Sasaki, T. *Chem. Mater.* **2010**, *22*, 371.

[55] Abell, G.; Coronado, E.; Martí-Gastaldo, C.; Pinilla-Cienfuegos, E.; Ribera, A. *J. Mater. Chem.* **2010**, *20*, 7451.

[56] Woo, M. A.;Song, M.-S.; Kim, T. W.; Kim, I. Y.; Ju, J.-Y.; Lee, Y. S.; Kim, S. J.; Choya, J-H.; Hwang, S.-J. *J. Mater. Chem.* **2011**, *21*, 4286.

Figures

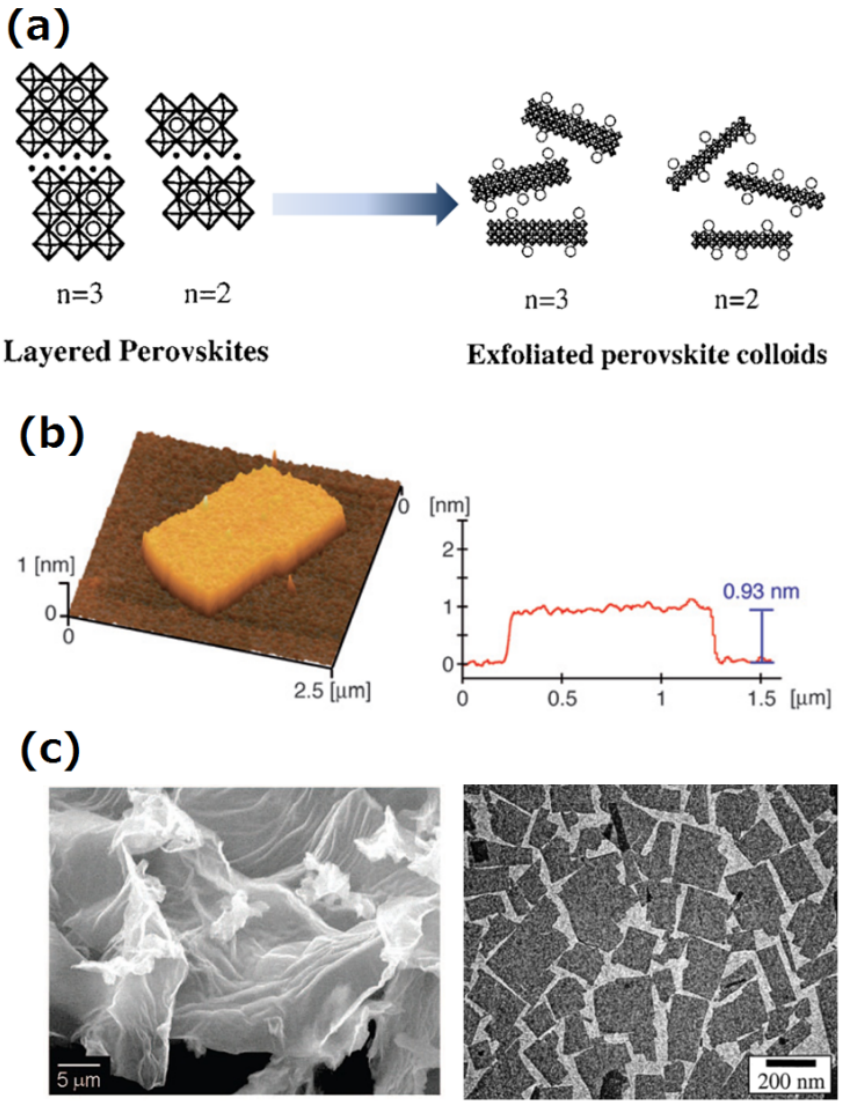

Figure 1. (a) Reaction scheme of exfoliation into metal oxide nanosheets. (b) Atomic force microscopy (AFM) image of $Ti_{0.91}O_2$ nanosheets (left), and height profile (right). (c) Scanning electrom microscopy (SEM) image of MnO_2 nanosheets (left), and transmission electron microscopy (TEM) image of $Ca_2Nb_3O_{10}$ nanosheets (right)

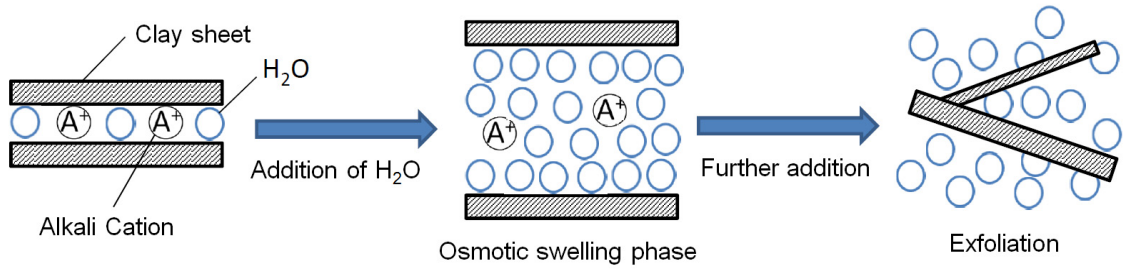

Figure 2. Exfoliation process of the clay compound.

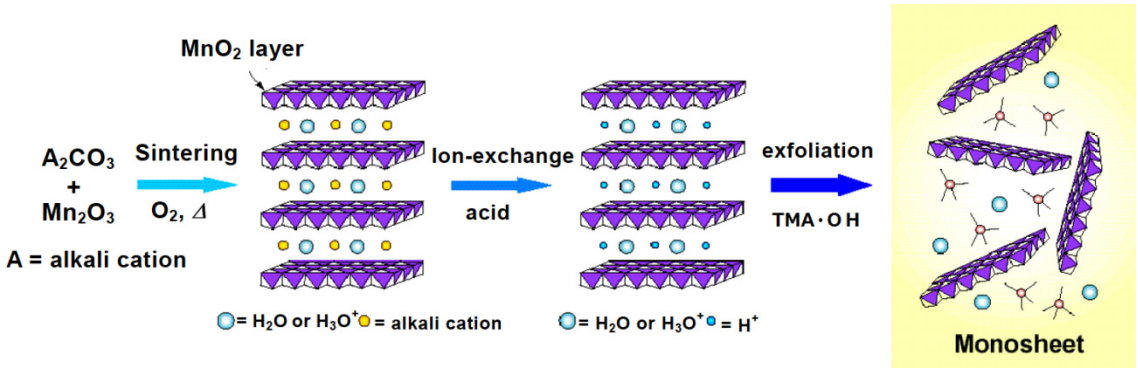

Figure 3. Reaction scheme of exfoliation reaction of layered metal oxide. This is an example for the layered manganese oxide (birnessite).

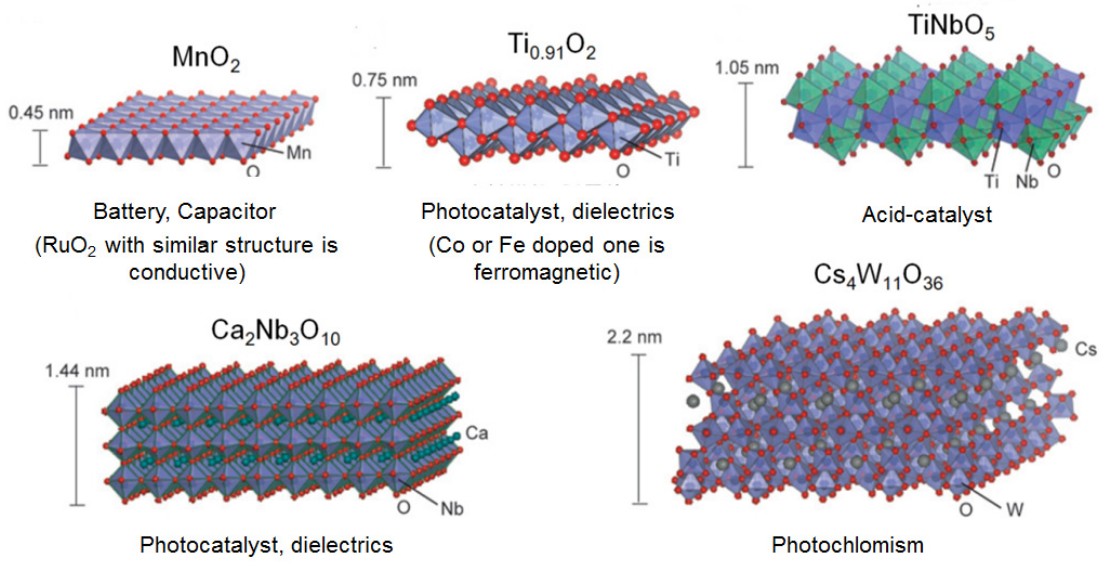

Figure 4. Representative structures of various functional nanosheets

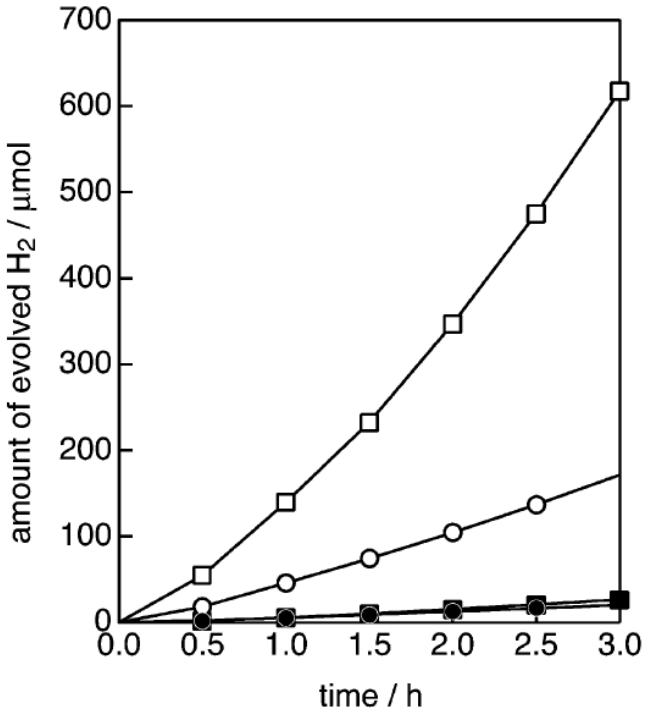

Figure 5. Hydrogen gas generation from aqueous methanol solutions: (■) restacked aggregates, $K^+/Ca_2Nb_3O_{10}$; (□) $K^+/Ca_2Nb_3O_{10}$ with Pt loading of 0.1 wt %; (●) starting compound of $KCa_2Nb_3O_{10}$; (○) $KCa_2Nb_3O_{10}$ with Pt loading of 0.1 wt %.

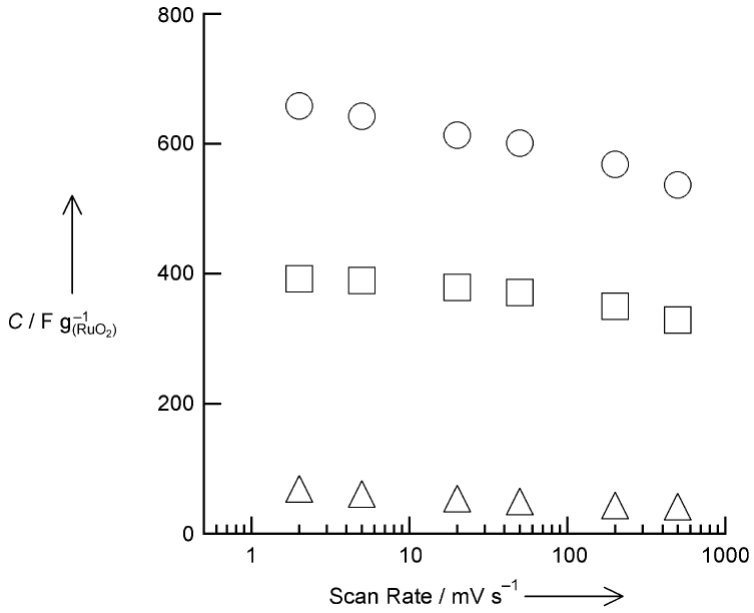

Figure 6. The specific capacitance as a function of the scan rate for rutile-type RuO_2 (△), layered ruthenic acid (□), and exfoliated ruthenic acid nanosheets (○) in 0.5m H_2SO_4 at 25°C.

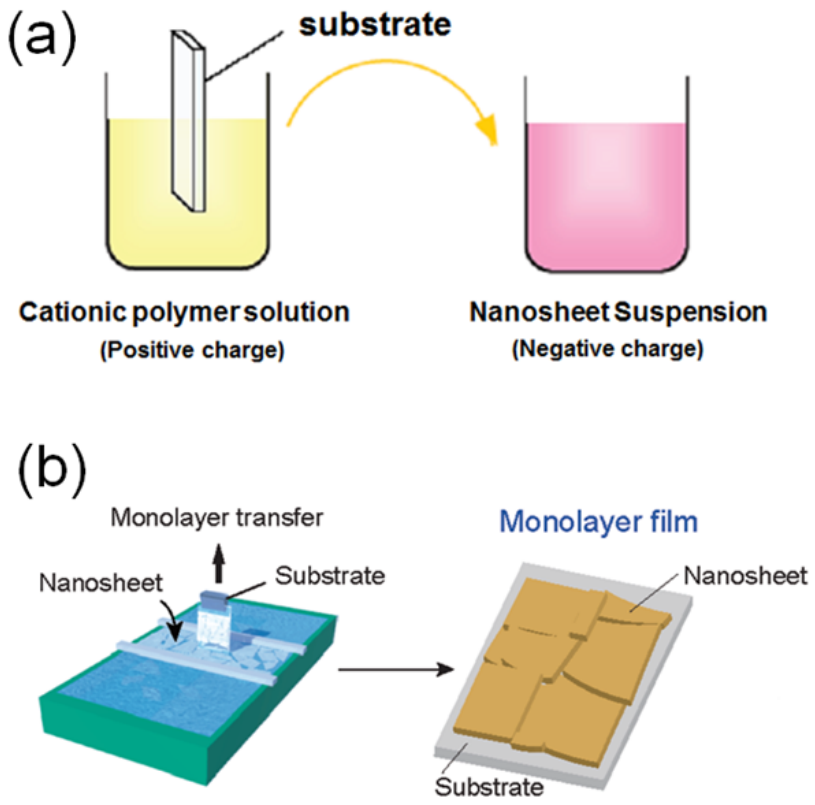

Figure 7. Fabrication procedures for multilayer films comprised of nanosheets. (a) Electrostatic deposition (ED) method; Substrate was dipped into the aqueous cationic polymer solution, and then into the nanosheets suspension. (b) Langmuir-Blodget (LB) method; monolayer film formed on air-water interface are transferred onto the substrate.

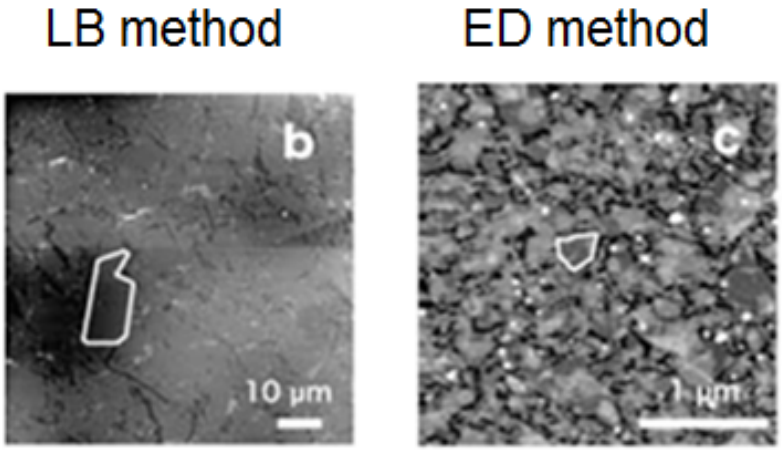

Figure 8. AFM images of the monolayer film obtained by LB method (left) and ED method (right). White line indicates the lateral size of single nanosheet.

Table 1. Examples of the inorganic nanosheets and appropriate combinations of exfoliating reagent and solvent.

Categoly	Host layer	Reported year [ref.]	Exfoliating reagent / solvent
Clay minerals	$(Al,Mg)_2Si_4O_{10}(OH)_2$	1954 [8]	LiCl / H_2O
Chalcogenides	TaS_2	1974 [32]	H^+ / H_2O
	TiS_2	1977 [33]	Alkali metal ion / H_2O
	NbS_2	1977 [33]	Alkali metal ion / H_2O
	MoS_2	1986 [34]	Li^+ / H_2O
Phosphates	α-$Zr(PO_4)_2$	1985 [35]	n-propylammonium / H_2O
	$VOVP_4$	2001 [36]	acrylamide / butanol
Oxides	$LaNb_2O_7$	2009 [12]	TBA^+ / H_2O
	$Ca_2Nb_3O_{10}$	2002 [19]	amino-acid / H_2O
	Ca_2Nb3-$xRhxO_{10-\delta}$	2011 [37]	TBA^+ / H_2O
	$Sr_2Nb_3O_{10}$	2009 [12]	TBA^+ / H_2O
	$Ca_2Na_{n-3}NbnO_{3n+1}$ (n = 3, 4)	1990 [38]	alkylammonium / acetone
	TiO_2	1996 [10a]	TBA^+ / H_2O
	$Ti_{(5.2-2x)/6}Mn_{x/2}O_2$	2009 [20b]	TBA^+ / H_2O
	$Ni_{0.4}Ti_{1.6}O_2$	2002 [39]	TBA^+ / H_2O
	$Fe_{0.8}Ti_{1.2}O_2$	2002 [40]	TBA^+ / H_2O
	Ti_3O_7	2003 [41]	propylammonium / H_2O
	$Ti_{1.73}O_4$	2003 [42]	TBA^+ / H_2O
	Nb_3O_8	2004 [11]	TBA^+ / H_2O
	Nb_6O_{17}	2004 [11]	TBA^+ / H_2O
	$K_2Nb_60_{17}$	1994 [14]	TBA^+ / H_2O
	$TiNbO_5$	2003 [13]	TBA^+ / H_2O
	$TiTaO_5$	2003 [43]	TBA^+ / H_2O
	Ti_2NbO_7	1994 [14]	TBA^+ / H_2O
	$TaWO_6$	2010 [15]	TBA^+ / H_2O
	$Gd_{1.6}Eu_{0.4}Ti_3O_{10}$	2008 [44]	ethylammonium / H_2O
	$La_{0.95}Eu_{0.05}Nb_2O_7$	2008 [44]	ethylammonium / H_2O
	$La_{0.7}Tb_{0.3}Ta_2O_7$	2008 [44]	ethylammonium / H_2O

Oxides	$Eu_{0.56}Ta_2O_7$	2008 [23]	TBA^+ / H_2O
	$La_{2/3-x}Eu_xTa_2O_7$	2011 [24]	TBA^+ / H_2O
	$Sm_{0.05}Nb_2O_7$	2009 [25]	TBA^+ / H_2O
	MnO_2	2000 [45]	TBA^+ / H_2O
	$Mn_{1/3}Co_{1/3}Ni_{1/3}O_2$	2009 [46]	TMA^+ / H_2O
	RuO_2	2010 [18]	TBA^+ / H_2O
	MoO_3	1991 [17]	Li^+ / H_2O
	Mo_2O_4	2011 [47]	TBA^+ / H_2O
	$W_{11}O_{36}$	2008 [22]	TBA^+ / H_2O
	Zeolite	2011 [48]	polystyrene/porystyrene (melt)
LDHs	$Zn_{1-x}Al_x(OH)_2$	2001 [49]	dodecylsulfonate / butanol
	$Mg_{1-x}Al_x(OH)_2$	2001 [50]	glycine / holmamide
	$LiAl_2(OH)_6$	2004 [51]	alkylsulfonate/ butanol
	$Co(OH)_2$	2008 [52]	ClO_4^- / holmamide
	$Ni_{1-x}Ga_x(OH)_2$	2008 [53]	glycine / holmamide
	$Ni_{1-x}Co_x(OH)_2$	2010 [54]	NO_3^- / holmamide
	$Ni_{1-x}Fe_x(OH)_2$	2010 [55]	NO_3^- / holmamide
	$Zn_{1-x}Co_x(OH)_2$	2011 [56]	NO_3^- / holmamide

Chaper 1:

Room-temperature Synthesis of Manganese Oxide Monosheets

1.1 Introduction

Nanosized materials with different morphologies, such as nanoparticles and clusters (zero-dimension; e.g. fullerenes), and nanotubes and nanowires (one-dimension; e.g. carbon nanotubes), have become increasingly important as potential systems for both fundamental interests and industrial applications.[1] Nanosheets are a new class of two-dimensional nanomaterials that are characterized by a thickness on the order of nanometers and by lateral dimensions of submicro- to micrometers.[2] So far, a wide variety of transition-metal oxide nanosheets such as $Ca_2Nb_3O_{10}$,[3] Nb_6O_{17},[4] $Ti_{1-\delta}O_2$,[5] and MnO_2,[6] to name only a few, have been discovered and investigated extensively due to the rich chemistry and physics of the bulk counterparts.[2] The utmost feature of the nanosheets is their exceptionally high specific surface area, rendering them promising candidates for a variety of applications, especially in photocatalysis and

electrodes of electrochemical devices.[2] Furthermore, the self-assembling ability of the nanosheets allows to form restacked lamellar aggregates with a disordered and porous nature,[7] leading to enhanced properties as found in $H_4Nb_6O_{17}$[8] and $HTiNbO_5$[9] for photocatalysis, Li/MnO_2[10] for electrodes of lithium-ion batteries, and $H/RuO_{2.1}$[11] for double-layer capacitors.

However, there have been several hurdles to be overcome in the possible future applications as follows: the synthesis of metal oxide nanosheets until very recently requires multistep processing, involving a high-temperature solid-state reaction (to yield a thermodynamically stable precursor phase, e.g. K/MnO_2), a protonation of interlayer alkali metal ions (to yield e.g. H/MnO_2), and an acid-base reaction with aqueous solution of quaternary ammonium cations (to finally yield negatively-charged nanosheets, e.g. $MnO_2^{\delta-}$ in the form of colloidal suspension). This top-down approach is cost and time consuming. Moreover, it is fairly difficult to exfoliate the protonated compounds completely into the single-layer nanosheets (monosheets). In practice, nanosheets previously obtained possess a wide thickness distribution. It has been highly desired to obtain monosheets as a main product, because they possess a large specific surface area and also serve as primitive building units to construct well-defined self-assemblies with functional organic and/or inorganic counterions. In this work, the author has established a novel single-step route to synthesize the MnO_2 monosheets within a day in a high yield. During the author's study, a single-step synthesis of $Ti_{1-\delta}O_2$ monosheets with uniform shape and size was reported by Yoon and his co-workers,[12] using titanium(IV) tetraisopropoxide in tetramethylammonium (TMA) hydroxide aqueous solution. While their processing requires the application of heat under reflux to access the $Ti_{1-\delta}O_2$ monosheets, the author's present reaction readily proceeds at room temperature (RT). In addition, the MnO_2 monosheets have been receiving much attention for their potential applications in electrochemistry and catalysis, mainly due to the low cost and safety hazards of manganese. Lamellar stacked Li/MnO_2 and layer-by-layer assembled poly(ethylenimide)/MnO_2, both of which are prepared from the MnO_2 monosheets, have been employed as electrodes for lithium-ion batteries[10] and double-layer capacitors,[13] respectively, and exhibited

improved performances associated with their porous structures. It is thus apparent that such rapid and facile RT processing promotes the works toward practical use of the MnO_2 monosheets.

1.2. Experimental Section

A. Synthesis

Solvents (water, methanol, acetonitrile, and chloroform) were distilled prior to use. $MnCl_2 \cdot 4H_2O$ (99.9%, Wako Pure Chemical), TMA·OH (1.0 M in H_2O, Aldrich), H_2O_2 (30wt% in H_2O, Santoku Chemical), and HBF_4 (48wt% in H_2O, Aldrich) were commercially available and used without purification. Commercially available TTF was purified by sublimation twice. BEDO-TTF was synthesized according to the literature procedure[28] and recrystallized twice from cyclohexane. $(TTF)_3(BF_4)_2$ was prepared using the chemical oxidation of TTF by H_2O_2 in the presence of HBF_4 in acetonitrile, according to literature procedure.[25] $(BEDO\text{-}TTF)_2BF_4$ was prepared in the same manner as $(TTF)_3(BF_4)_2$.

1.2.1 Preparation of Colloidal Birnessite Monosheets

Typically, 20 mL of a mixed aqueous solution of 0.6 M TMA·OH and 3 wt% H_2O_2 was added to 10 mL of 0.3 M $MnCl_2 \cdot 4H_2O$ aqueous solution within 15 seconds. The resulting dark brown suspension was stirred vigorously overnight in the open air at RT, which is accompanied by O_2 gas generation. Dried aggregate was separated by filtration (MILLIPORE, Type-JH, 0.45 μm pore size), washed with copious amount of distilled water and methanol, and then air-dried at RT. No trace of Cl was detected from EDS of the dried aggregate (Figure 1.1).

1.2.2. Preparation of Self-Assembled Potassium-Type Birnessites

Self-assembly of MnO_2 monosheets was induced by mixing the colloidal suspension of the monosheets with a KCl aqueous solution. Typically, 50 mL of 1 M KCl aqueous solution was added dropwise

within an hour to 50 mL of colloidal suspension of MnO_2 monosheets (2×10^{-2} M) at 40 °C. Immediately after the addition, flocculation occurred in the mixed solution. After standing at RT for a week, the resulting black precipitate was filtered off, washed with copious amount of distilled water and methanol, and air-dried at RT (Yield 94%). The K/Mn ratio was estimated to be 0.20 on the basis of EDS (Figure 1.2).

1.2.3. Preparation of Self-assembled Organic-Inorganic Layered Hybrid TTF/MnO_2

Typically, 0.50 g (0.64 mmol) of powdered $(TTF)_3(BF_4)_2$ was added to 300 mL of colloidal suspension of MnO_2 monosheets (3×10^{-3} M) during N_2 bubbling at RT. After stirring for a few minutes, flocculation occurred in the mixed solution. The resulting black precipitate was filtered off, washed with acetonitrile, and air-dried at RT (Yield 78%). The TTF/Mn ratio was estimated to be 0.15 on the basis of EDS (Figure 1.3), and the Infrared (IR) absorption spectrum indicates no trace of BF_4 anions (Figure 1.5).

1.2.4. Preparation of Self-assembled Organic-Inorganic Layered Hybrid BEDO-TTF/MnO_2

1.5 g (2.1 mmol) of powdered $(BEDO\text{-}TTF)_2BF_4$ was added to 300 mL of colloidal suspension of MnO2 monosheets (6.7×10–2 M) during N_2 bubbling at RT. After stirring for a day, flocculation occurred in the mixed solution. The resulting black precipitate was filtered off, washed with acetonitrile, and air-dried at RT (Yield 94%). The BEDO-TTF/Mn ratio was estimated to be 0.21 on the basis of EDS (Figure 1.4), and the Infrared (IR) absorption spectrum indicates no trace of BF_4 anions (Figure 1.6).

1.2.5. Fabrication of LB Films

Fused silica substrates for depositing the films were cleaned with detergent followed by several rinses with water, and sonicated in fresh lots of water three times for 30 min each. Their surfaces were made hydrophilic by treating with piranha solution (H_2O_2 : H_2SO_4 = 7:3) for 90 min followed by sonication

and rinsing in water. The π–A isotherm measurements and film fabrications were carried out employing a USI Co. Ltd. Model FDS-23 LB trough equipped with a Wilhelmy plate for pressure sensing. A diluted aqueous suspension of MnO_2 monosheets (0.01 g L^{-1}) was used as a subphase. After standing for an hour, the surface of the subphase was compressed at a rate of 5 cm^2 per minute by moving the barrier. The compressed film was deposited onto hydrophilic silica substrate at a surface pressure of 10 mN m^{-1} by the vertical deposition method. All experiments were carried out at 20 °C, and high purity water (<0.1 μS sec^{-1}) was used for all operations.

B. Measurements

SEM and EDS experiments were conducted with a JEOL JSM-5510LVN Scanning Electron Microscope operated at 20 kV. Samples are mounted on carbon tape. A Seiko SPA400 AFM instrument was employed to visualize a surface topography of the nanosheets. Measurements were carried out in tapping mode with a silicon-tip cantilever having a force constant of 20 N m^{-1}. Samples were deposited onto fluorinated mica substrate (Fluoro-Phologopite, Topy Industry Ltd.) precoated with polyethyleneimine by spin-coating (1,000 rpm for 15 seconds and 2,000 rpm for 30 seconds) of 0.1 g L^{-1} colloidal suspension. Powder XRD measurements were carried out with a MAC Science M18XHF diffractometer using Cu Kα radiation at a scanning rate of 0.01° s^{-1} in a 2θ range of 5–80°. UV-Vis absorption spectra were taken in a quartz cell with light path length of 1 cm on a Shimadzu UV-3100 spectrophotometer (250–800 nm). Time acquisition of the absorption spectra was measured using an Ocean Optics HR-2000 spectrophotometer. FT-IR spectra were taken in dispersed KBr pellets on a Perkin-Elmer 1000 Series spectrophotometer (400–7,800 cm^{-1}). A Quantum Design MPMS-XL superconducting quantum interference device (SQUID) magnetometer was used to collect DC magnetic susceptibility data between 1.9 and 300 K. The AC magnetic susceptibilities for 1.9–20 K were determined in the range of 1 Hz to 1 kHz using a Quantum Design MPMS-5S SQUID magnetometer.

1.3 Results and Discussions

1.3.1 Formation of MnO_2 Monosheets

The author's approach follows the preparation of lithium- and sodium-type birnessites by using hydrogen peroxide (H_2O_2) as an oxidizing agent for Mn^{2+} ions.[14] Here the author used, in addition to H_2O_2, TMA·OH in aqueous solution of manganese(II) chloride ($MnCl_2$, Figure 1.9a) which readily gave dark brown suspension in open air at RT (Figure 1.9b). The observation of Tyndall light scattering in the suspension confirms the colloidal dispersion of the product, and no precipitation was observed in 3 days. Such suspension was obtained even when trivalent manganese(III) acetylacetonate ($Mn(acac)_3$) was used instead of divalent $MnCl_2$, presumably as a reflection of the hydrolysis of $Mn(acac)_3$. In relation, the formation of spinel $LiMn_2O_4$ and orthorhombic $LiMnO_2$ was found by making use of the hydrolysis of $Mn(acac)_3$ in LiOH aqueous solution.[15]

Because of the difficulties in confirming the presence of MnO_2 monosheets in the colloidal suspension, their dried aggregates were observed using electron microscopic technique (Figure 1.10). Scanning electron microscopy (SEM) image of freeze-dried aggregate of the product showed flexible flaky form with lateral dimension of micrometers, as typically shown in Figure 1.11a. The sheet-like structure was also evident from a tapping-mode atomic force microscopy (AFM) image of the sample deposited by spin-coating of the colloidal suspension onto fluorinated mica substrate precoated with polyethyleneimine (Figure 1.11c). The lateral dimension of the sample lies in the range of 50–500 nm, which is much larger than $Ti_{1-\delta}O_2$ monosheets obtained by the single-step approach by Yoon et al. (< 30 nm).[14] The height profile scan demonstrates a fairly flat surface of the sheets with an approximate thickness of 0.9 nm. The dimensions are comparable to those of the MnO_2 monosheets obtained by the conventional processing,[16] suggesting a successful formation of the monosheets. Given a thickness of the MnO_2 monosheet (0.52 nm), the hydration on both sides of the monosheets can reasonably explain the observed thickness, as discussed in ref. 21. Furthermore, the AFM image displays stepwise structure with a step of *ca.* 0.7 nm, in consistency with the thickness expected from the MnO_2 monosheet

hydrated on the top. The most remarkable observation in this study is that the majority of coverage area is composed of the monosheets (Figure 1.11d). The author notes that replacing the TMA cation with a more bulky tetrabutylammonium cation while keeping the other conditions produces the similar results. When primary *n*-butylamine was used instead of quaternary tetraalkylammonium cations, on the other hand, the black precipitate of layered hybrid *n*-butylammonium/MnO_2 was readily obtained. This result will be reported in a separated paper.[18]

Figure 1.12 is the absorption spectra in the range of 250–800 nm as a function of concentration of the colloidal suspension. An absorption band attributable to the *d–d* transition of Mn ions in the MnO_6 octahedra of the MnO_2 monosheets[15,19] was observed at around 380 nm. This band follows the Beer's law in the measured concentration range (inset of Figure 1.12), and the molar extinction coefficient at 380 nm is estimated to be 9.6×10^3 M^{-1} cm^{-1} provided that the composition is $(TMA)_{0.20}MnO_2\cdot0.2H_2O$ (*vide infra*). The energy and intensity of the band are comparable to those obtained by the conventional multistep processing.[16]

A similar strategy to obtain metal oxide nanosheets without a high-temperature treatment was recently implemented by Oaki and Imai.[20] They employed ethylenediaminetetraacetate (EDTA) as chelating agents for Mn^{2+} ions so as to inhibit the rapid precipitation of $Mn(OH)_2$. Here the Mn^{2+} ions were oxidized slowly by dissolved oxygen in the solution. However, the precipitate is far from monosheets but consists of multi-layers with a thickness of at least 10 nm (i.e., more than 10 layers), and the whole processing requires 3–5 days. In the author's processing, on the other hand, H_2O_2 serves as an oxidizing agent to form MnO_2 monosheets in alkaline medium, and TMA cations, previously used for the exfoliation of layered H/MnO_2,[6,21] would play an essential role during the course of two-dimensional growth of the monosheets; namely, the cations serve not only to inhibit the flocculation of the monosheets but also to exfoliate the locally-aggregated monosheets in the suspension. Although the author do not have information about the production mechanism of the MnO_2 monosheets as the *d-d* absorption band appears and saturates within the measurement limit of the time acquisition measurement system (*ca.* 0.2 sec), the author believe that the author's rapid and facile processing

promotes the practical use of the MnO_2 monosheets in lithium ion batteries, catalysts, selective adsorbents and so on, and also is generally applied to the fabrication of the other metal oxide monosheets.

1.3.2. Structural and Physical Properties of Dried Aggregate

In order to obtain further evidence of the formation of MnO_2 monosheets, powder X-ray diffraction (XRD) of dried sample of the colloidal suspension, which was separated by filtration, washing with copious amount of distilled water and methanol, and then air-drying at RT, was measured. The XRD pattern is indexed as a hexagonal unit cell and has intense (00*l*) reflections associated with preferred orientation of the sample (Figure 1.13a), which is similar to that of the dried aggregate TMA/MnO_2 obtained by the conventional processing.[21,22] The interlayer spacing of 0.95 nm indicates the flocculation of the MnO_2 monosheets together with TMA and water molecules,[21,22] which should be mainly driven by electrostatic interactions between negatively-charged monosheets and TMA cations. Together with this observation, the elemental analysis (Calcd: C, 9.12; H, 2.68; N, 2.66%. Found: C, 9.16; H, 2.67; N, 2.69%) lets us to conclude that the composition of the dried aggregate is formulated as $(TMA)_{0.20}MnO_2 \cdot 0.2H_2O$, which yields the valence state on Mn of *ca.* +3.8.

Figure 1.14 a displays the temperature dependence of DC susceptibility (χ) for the dried aggregate in an applied magnetic field of 1 kOe. Above 20 K, it follows the Curie-Weiss expression with $\chi = C(T - \theta)^{-1}$, with Curie constant ($C$) of 1.44 emu K mol^{-1} and Weiss temperature (θ) of –36.4 K. As seen in the inset of Figure 1.14a, a susceptibility cusp was observed at around 10 K, below which there is a distinct difference between the zero field cooled (ZFC) and field cooled (FC) susceptibilities. The cusp was also observed in both in-phase (χ') and out-of-phase (χ'') components of the AC susceptibility, and show an increase of *ca.* 1 K with increasing frequency (ν) in going from 1 Hz to 1 kHz (Figure 1.14b for χ'). The frequency shift in T_f (peak temperature of χ') is diagnostic for a glassy effect such as spin-glass or superparamagnetism, and is defined as $\gamma = \Delta T_f / [T_f(0)\Delta(\log \nu)]$, where $T_f(0)$ is the peak temperature extrapolated at $\log \nu = 0$. The calculated small γ value (0.035) strongly indicates that the behavior is not

due to the superparamagnetism, but arises from the spin-glass forming.[23] This behavior should be inherent to the geometrical frustration caused by the triangular arrangement of the mixed valence $Mn^{4+/3+}$ ions in the MnO_2 layer. A similar trend was observed for K/MnO_2, H/MnO_2, and TMA/MnO_2 obtained by the conventional processing (Figures 1.15 – 1.17).

1.3.3. Self-Assembly of MnO_2 Monosheets

Since the MnO_2 monosheets have a negative charge as mentioned above, the electrostatic interactions with organic and/or inorganic cations would bring about the self-assembling to yield lamellar aggregates using the present colloidal suspension. In the following, the preparation of lamellar aggregates formed with alkali and π-conjugated organic cations, and Langmuir-Blodgett (LB) films deposited onto hydrophilic silica substrate were presented.

1.3.3.1. Potassium-Type Birnessite

A self-assembled potassium-type birnessite was readily precipitated in nearly quantitative yield, by adding an excess amount of KCl to the colloidal suspension as seen in Figure 1.8c. In comparison with the dried aggregate TMA/MnO_2, XRD pattern (Figure 1.13b) and SEM image (Figure 1.11b) of the self-assembled K/MnO_2 allow to assert that it has a layered structure as well, but the interlayer spacing is much reduced to 0.70 nm, which is comparable to that of the potassium-type birnessite previously reported.[26] The K/Mn ratio was estimated to be 0.20 on the basis of energy-dispersive X-ray spectroscopy (EDS, Figure 1.2), and the valence state on Mn of *ca.* +3.8 is in good agreement with that of the dried aggregate.

1.3.3.2. Organic-Inorganic Layered Hybrids

Layered hybrids composed of TTF and bis(ethylenedioxy)-TTF (BEDO-TTF) (Scheme 1.1), which have afforded a number of organic metals including superconductors,[24,25] were immediately obtained by adding powdered $(TTF)_3(BF_4)_2$[26] and $(BEDO\text{-}TTF)_2BF_4$ in the colloidal suspension. Provided that the

molecular lengths of TTF and BEDO-TTF are *ca.* 0.9 and 1.3 nm, respectively, the significantly expanded interlayer spacings of 1.45 and 1.84 nm (Figures 1.13c,d) suggest the formation of the layered hybrids with TTF analogues orienting almost perpendicular to the MnO_2 layers. According to the S/Mn ratios estimated from EDS (Figures 1.3 and 1.4), the composition of the hybrids can be formulated as $(TTF)_{0.15}MnO_2 \cdot 1.0H_2O$ and $(BEDO\text{-}TTF)_{0.21}MnO_2 \cdot 1.6H_2O$, in which the water contents were estimated from the thermogravimetric analyses. UV-Vis absorption spectra of the hybrids dispersed in the compressed KBr disk show a low-energy band at around 5×10^3 cm^{-1} (Figures 1.5 and 1.6). This band can be assigned to the intermolecular transition between partially-charged TTF analogues, suggesting that these hybrids can be potentially a metal[24,25] though the semiconducting behavior was observed possibly due to the inhomogeneous packing of TTF analogues.

1.3.3.3. Langmuir-Blodgett (LB) Films

Figure 1.18a shows the surface pressure-area (π–A) isotherm of the diluted colloidal suspension of MnO_2 monosheets (0.01 g L^{-1}). A clear solid-condensed phase was observed as the case of $Ti_{1-\delta}O_2$ monosheets.[27] The LB films were fabricated on fused silica substrate by the LB deposition method without any amphiphilic additives at the air-water interface. UV-Vis spectra of the films for each deposition process display an absorption band at around 368 nm (Figure 1.18b) as those of the colloidal suspensions, and the absorbance of the band linearly increases with each deposition process (inset of Figure 1.18b). Since the AFM observation of the film fabricated by single deposition process reveals that the majority of coverage area is composed of the MnO_2 monosheets, it appears that about one layer of monosheets was transferred for each deposition process. XRD pattern of the film with 30 layers, which displays a reflection at $2\theta = 12°$ corresponding to the interlayer spacing of 0.73 nm (Figure 1.19), confirms the regular stacking of the MnO_2 monosheets, although the sort of interlayer cations is unclear at the present stage.

1.4. Conclusions

In this study, the author found a rapid and facile route to access a colloidal suspension of MnO_2 monosheets in a high yield. Despite the author's single-step approach cuts the processing time to less than a day and eliminates the treatments with the use of special equipments, their structural, spectroscopic, and magnetic properties are comparable to those of the MnO_2 monosheets (or their aggregate) obtained by the conventional multistep processing. Also, the author's processing empowers to fabricate the high-purity organic-inorganic layered hybrids and LB films composed of the MnO_2 monosheets. Further works, particularly on the applications of the author's processing into the fabrication of other metal oxide monosheets, are in progress.

References

[1] (a) *Handbook of Nanostructured Materials and Nanotechnology*; Nalwa, H. S., Ed.; Academic Press: New York, 2000. (b) *Nanomaterials Chemistry*; Rao, C. N. R.; Mueller, A.; Cheetham, A. K., Ed.; Wiley-VCH Verlag: Weinheim, 2007.

[2] (a) Schaak, R. E.; Mallouk, T. E. *Chem. Mater.* **2002**, *14*, 1455. (b) Sasaki, T. *J. Ceram. Soc. Jpn.* **2007**, *115*, 9.

[3] Fang, M.; Kim, C. H.; Saupe, G. B.; Kim, H.-N.; Waraksa, C. C.; Miwa, T.; Fujishima, A.; Mallouk, T. E. *Chem. Mater.* **1999**, *11*, 1526.

[4] Abe, R.; Shinohara, K.; Tanaka, A.; Hara, M.; Kondo, J. N.; Domen, K. *J. Mater. Res.* **1998**, *13*, 861.

[5] Sasaki, T.; Watanabe, M.; Hashizume, H.; Yamada, H.; Nakazawa, H. *J. Am. Chem. Soc.* **1996**, *118*, 8329.

[6] Liu, Z.-h.; Ooi, K.; Kanoh, H.; Tang, W.-p.; Tomida, T. *Langmuir* **2000**, *16*, 4154.

[7] Ebina, Y.; Sasaki, T.; Harada, M.; Watanabe, M. *Chem. Mater.* **2002**, *14*, 4390.

[8] Domen, K.; Ebina, Y.; Ikeda, S.; Tanaka, A.; Kondo, J. N.; Maruya, K. *Catal. Today* **1996**, *28*, 167.

[9] Takagaki, A.; Sugisawa, M.; Lu, D.; Kondo, J. N.; Hara, M.; Domen, K.; Hayashi, S. *J. Am. Chem. Soc.* **2003**, *125*, 5479.

[10] Wang, L.; Takada, K.; Kajiyama, A.; Onoda, M.; Michiue, Y.; Zhang, L.; Watanabe, M.; Sasaki, T. *Chem. Mater.* **2003**, *15*, 4508.

[11] Sugimoto, W.; Iwata, H.; Yasunaga, Y.; Murakami, Y.; Takasu, Y. *Angew. Chem. Int. Ed.* **2003**, *42*, 4092.

[12] Tae, E. L.; Lee, K. E.; Jeong, J. S.; Yoon, K. B. *J. Am. Chem. Soc.* **2008**, *130*, 6534.

[13] Zhang, X.; Yang, W.; Evans, D. G. *J. Power Sources* **2008**, *184*, 695.

[14] (a) Feng, Q.; Sun, E.; Yanagisawa, K.; Yamasaki, N. *J. Ceram. Soc. Jpn.* **1997**, *105*, 564. (b) Feng, Q.; Higashimoto, Y.; Kajiyoshi, K.; Yanagisawa, K. *J. Mater. Sci. Lett.* **2001**, *20*, 269. (c) Cai, J.; Liu, J.; Suib, S. L. *Chem. Mater.* **2002**, *14*, 2071.

[15] Barriga, C.; Calero, A.; Morales, C. J.; Tirado, J. L. *React. Solids* **1989**, *7*, 263.

[16] Omomo, Y.; Sasaki, T.; Wang, L.; Watanabe, M. *J. Am. Chem. Soc.* **2003**, *125*, 3568.

[17] Sasaki, T.; Ebina, Y.; Kitami, Y.; Watanabe, M.; Oikawa, T. *J. Phys. Chem. B* **2001**, *105*, 6116.

[18] Kai, K.; Yoshida, Y.; Kageyama, H.; Saito, G. *J. Chem. Soc., Dalton Trans.* **2011**, in press.

[19] (a) Gao, Q.; Giraldo, O.; Tong, W.; Suib, S. L. *Chem. Mater.* **2001**, *13*, 778. (b) Wang, L.; Omomo, Y.; Sakai, N.; Fukuda, K.; Nakai, I.; Ebina, Y.; Takada, K.; Watanabe, M.; Sasaki, T. *Chem. Mater.* **2003**, *15*, 2873.

[20] Oaki, Y.; Imai, H. *Angew. Chem. Int. Ed.* **2007**, *46*, 4951.

[21] Yang, X.; Makita, Y.; Liu, Z.-h.; Sakane, K.; Ooi, K. *Chem. Mater.* **2004**, *16*, 5581.

[22] Brock, S. L.; Sanabria, M.; Suib, S. L.; Urban, V.; Thiyagarajan, P.; Potter, D. I. *J. Phys. Chem. B* **1999**, *103*, 7416.

[23] Mydosh, J. A. *Spin Glass*; Taylor & Francis: London, 1993.

[24] Saito, G.; Yoshida, Y. *Bull. Chem. Soc. Jpn.* **2007**, *80*, 1.

[25] Horiuchi, S.; Yamochi, H.; Saito, G.; Sakaguchi, K.; Kusunoki, M. *J. Am. Chem. Soc.* **1996**, *118*, 8604.

[26] Wudl, F. *J. Am. Chem. Soc.* **1975**, *97*, 1962.

[27] Muramatsu, M.; Akatsuka, K.; Ebina, Y.; Wang, K.; Sasaki, T.; Ishida, T.; Miyake, K.; Haga, M. *Langmuir* **2005**, *21*, 6590.

[28] Suzuki, T.; Yamochi, H.; Srdanov, G.; Hinkelmann, K.; Wudl, F. *J. Am. Chem. Soc.* **1989**, *111*, 3108.

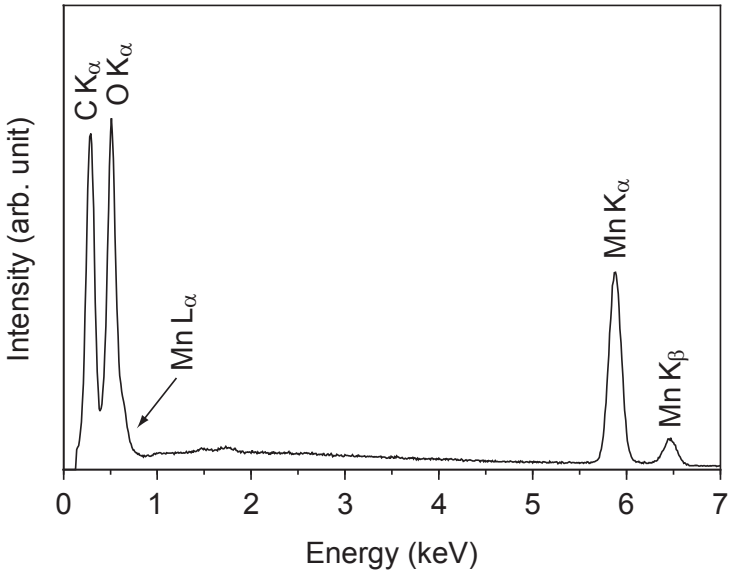

Figure 1.1. EDS spectrum of colloidal aggregate TMA/MnO_2. No trace of Cl, which is included in a starting material $MnCl_2$, was detected.

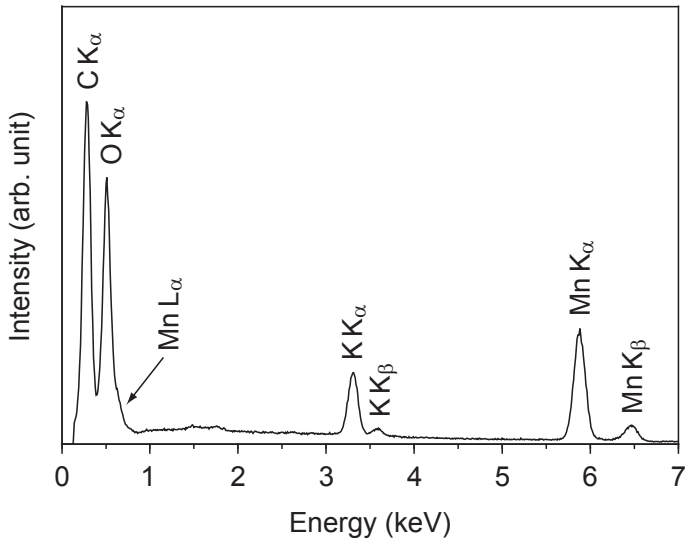

Figure 1.2. EDS spectrum of self-assembled K/MnO_2. The K/Mn ratio was estimated to be 0.20.

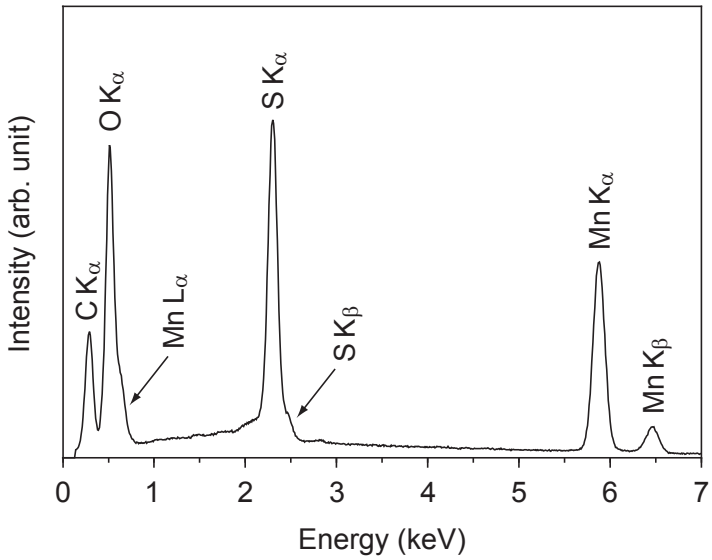

Figure 1.3. EDS spectrum of self-assembled organic-inorganic layered hybrid TTF/MnO_2. The TTF/Mn ratio was estimated to be 0.21.

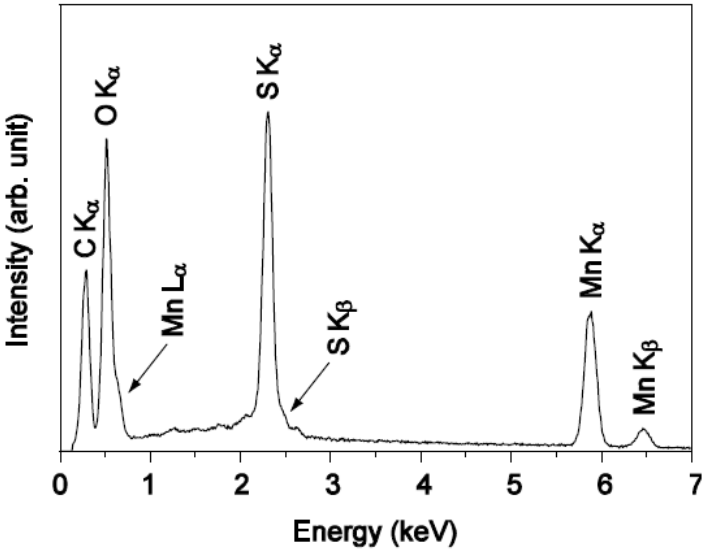

Figure 1.4. EDS spectrum of self-assembled organic-inorganic layered hybrid BEDO-TTF/MnO2. The BEDO-TTF/Mn ratio was estimated to be 0.21.

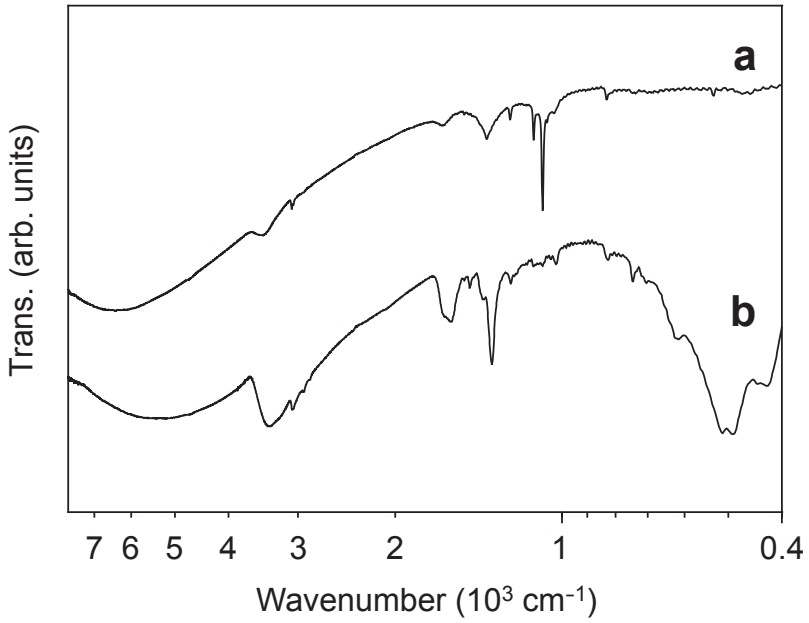

Figure 1.5. Infrared spectra measured in compressed KBr pellets. (a) Spectrum of starting material $(TTF)_3(BF_4)_2$. (b) Spectrum of self-assembled organic-inorganic layered hybrid TTF/MnO_2. A broad band at around 500 cm^{-1} is ascribed to Mn–O stretching mode. An intense B–F stretching signal of BF_4 anions (1,084 cm^{-1}) is disappeared in b. A broad band at around 6,000 cm^{-1} observed for both spectra is ascribed to the intermolecular transition between partially-charged TTF molecules.

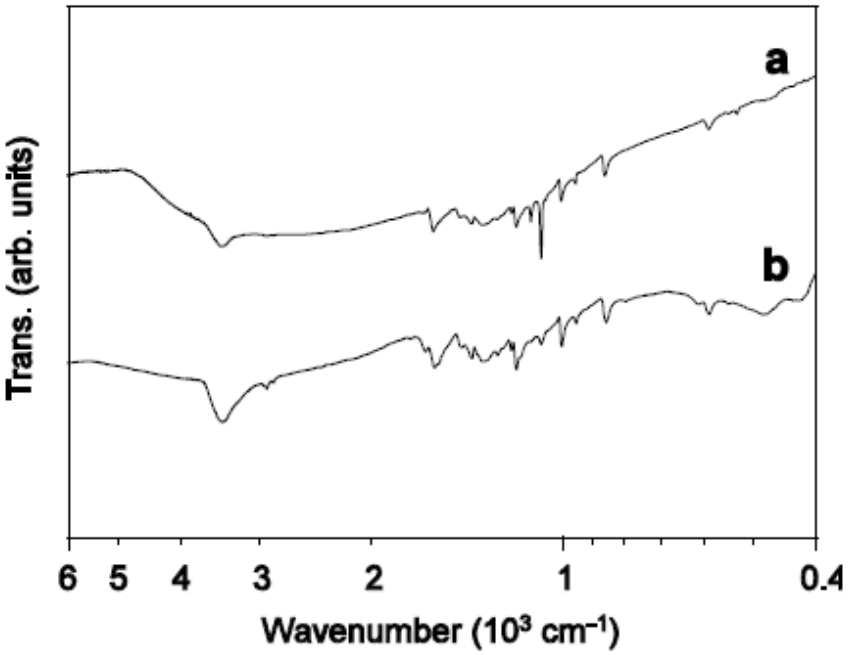

Figure 1.6. Infrared spectra of (a) starting material $(BEDO\text{-}TTF)_2BF_4$ and (b) self-assembled organic-inorganic layered hybrid BEDO-TTF/MnO_2 measured in compressed KBr pellets. A broad band at around 500 cm^{-1} is ascribed to Mn–O stretching mode. An intense B–F stretching signal of BF_4 anions (1,084 cm^{-1}) and signals of TMA cations (948, 1,488, and 2,800–3,100 cm^{-1}) are disappeared in (b). A broad band at around 4,000 cm^{-1} observed for both spectra is ascribed to the intermolecular transition between partially-charged BEDO-TTF molecules.

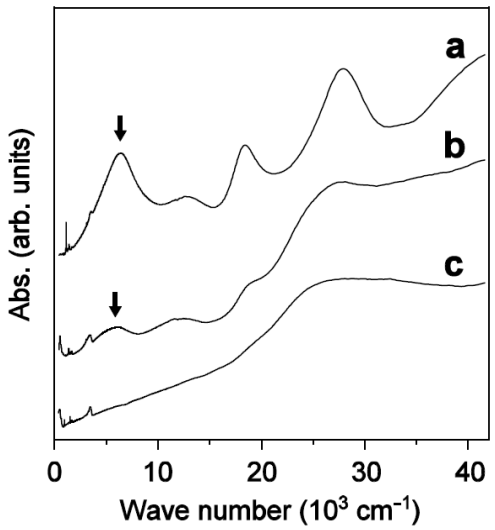

Figure 1.7. UV-Vis spectra of (a) starting material $(TTF)_3(BF_4)_2$, (b) self-assembled organic-inorganic layered hybrid TTF/MnO_2, and (c) dried aggregate TMA/MnO_2 measured in compressed KBr pellets. A broad absorption band at around 6,000 cm^{-1} (arrows) is ascribed to the intermolecular transition between partially-charged TTF molecules.

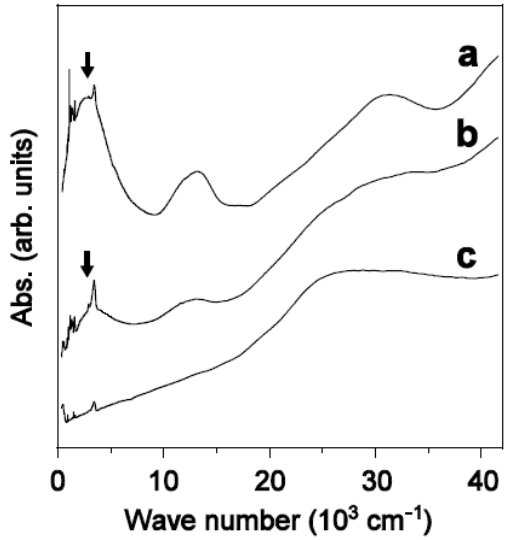

Figure 1.8. UV-Vis spectra of (a) starting material $(BEDO\text{-}TTF)_2BF_4$, (b) self-assembled organic-inorganic layered hybrid BEDO-TTF/MnO_2, and (c) dried aggregate TMA/MnO_2 measured in compressed KBr pellets. A broad absorption band at around 4,000 cm^{-1} (arrows) is ascribed to the intermolecular transition between partially-charged BEDO-TTF molecules.

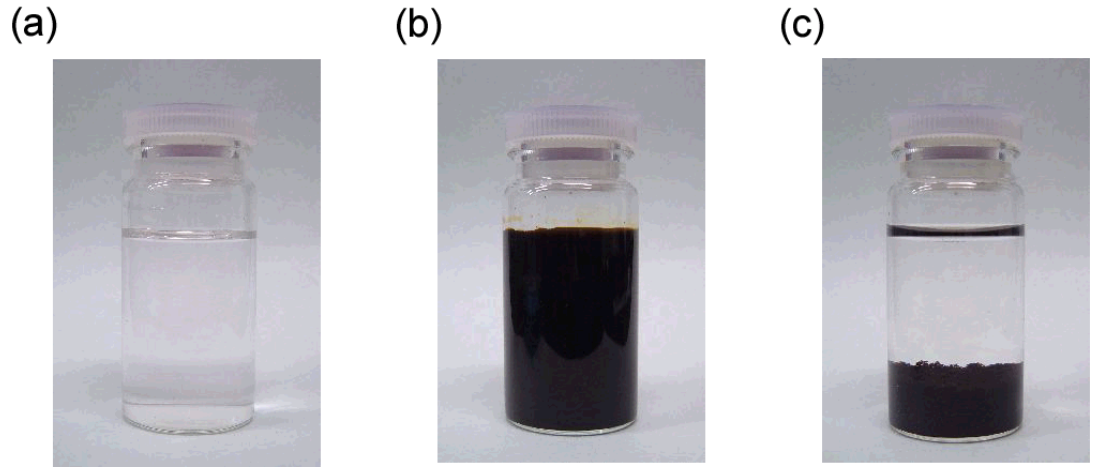

Figure 1.9. Photographs of (a) pale pink $MnCl_2$ aqueous solution, (b) dark brown colloidal suspension of MnO_2 monosheets obtained by adding a mixed aqueous solution of TMA·OH and H_2O_2 to the $MnCl_2$ solution, and (c) black potassium-type birnessite precipitated by adding a KCl aqueous solution to the colloidal suspension.

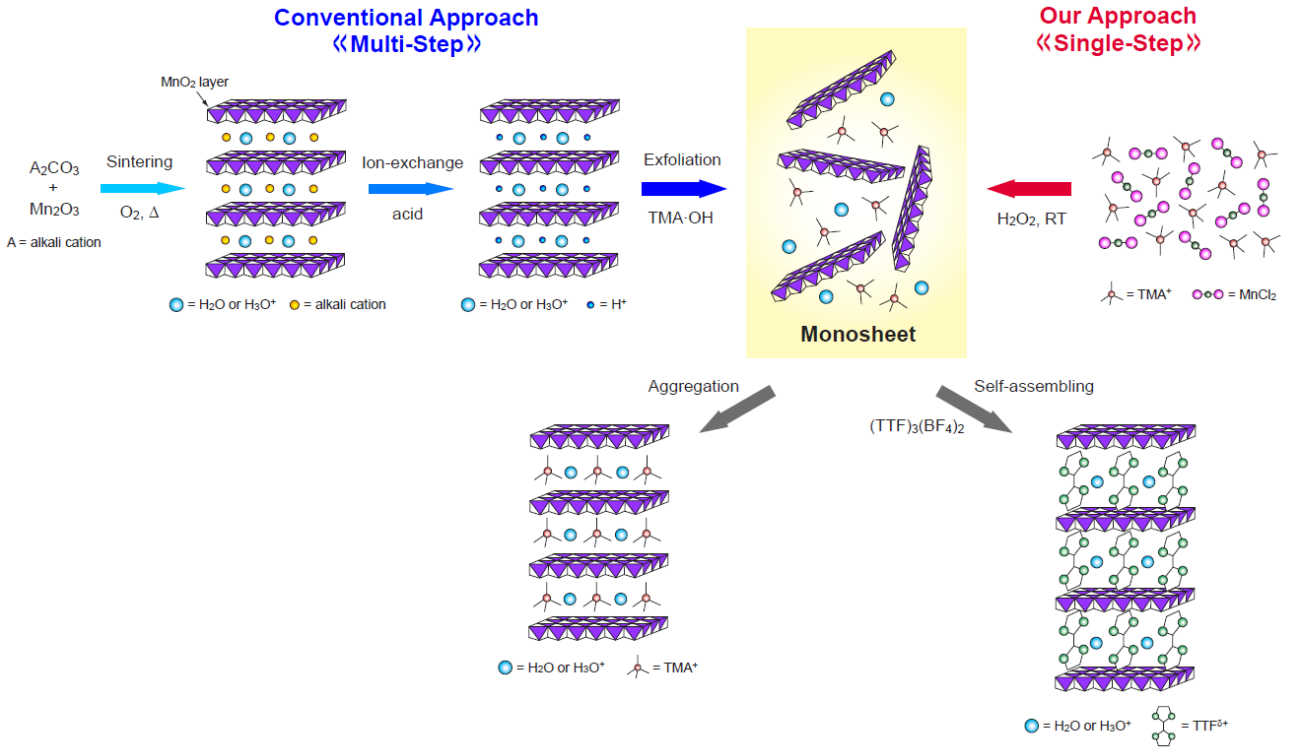

Figure 1.10. Schematic figure emphasizing the difference between the conventional multi-step (top-down) and my single-step approaches to obtain MnO_2 monosheets.

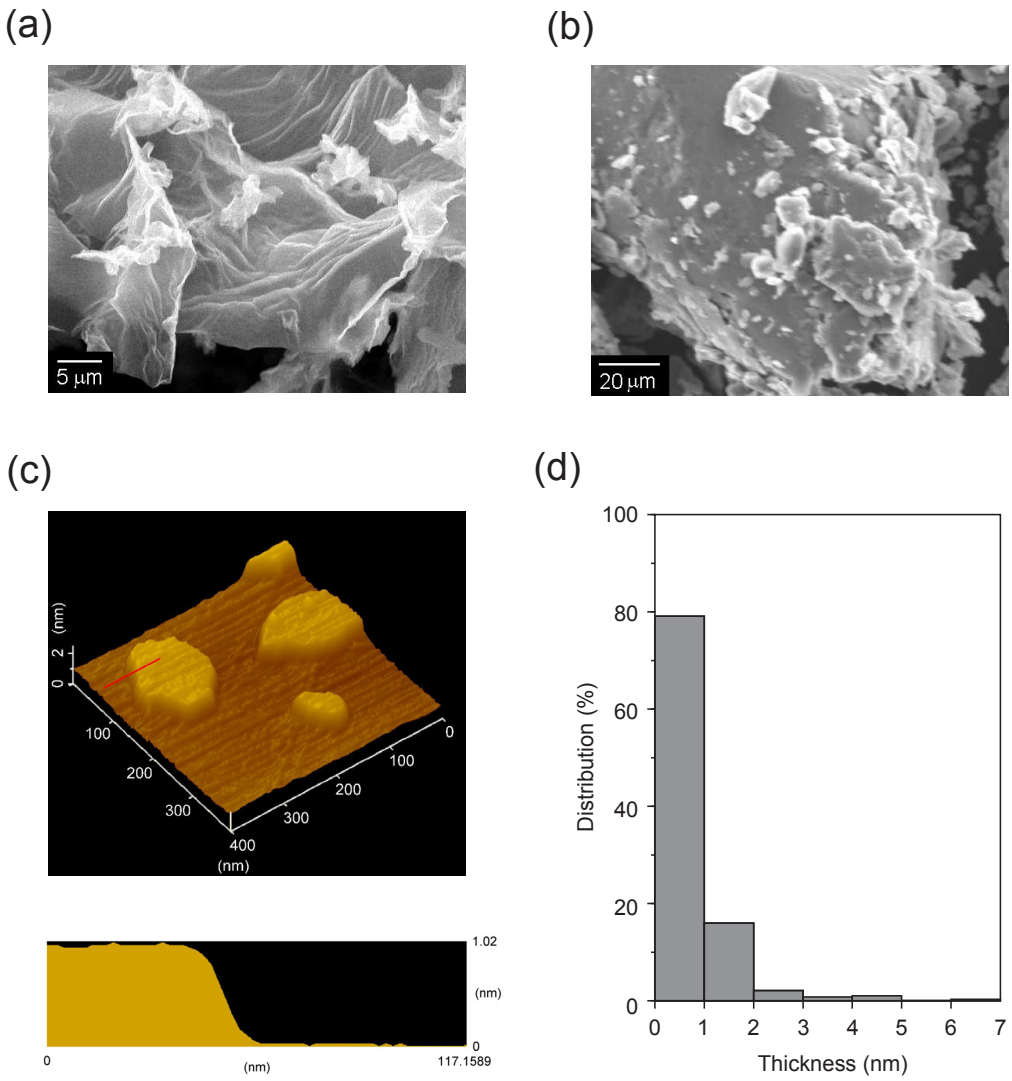

Figure 1.11. SEM image of (a) freeze-dried aggregate of MnO_2 monosheets and (b) self-assembled K/MnO_2. (c) Tapping-mode AFM image of MnO_2 monosheets and height profile along the red line in the image. The monosheets are deposited onto fluorinated mica substrate precoated with polyethyleneimine by spin-coating (1,000 rpm for 15 seconds and 2,000 rpm for 30 seconds) of 0.1 g L^{-1} colloidal suspension. (d) Histogram of thickness of the MnO_2 sheets on the substrate.

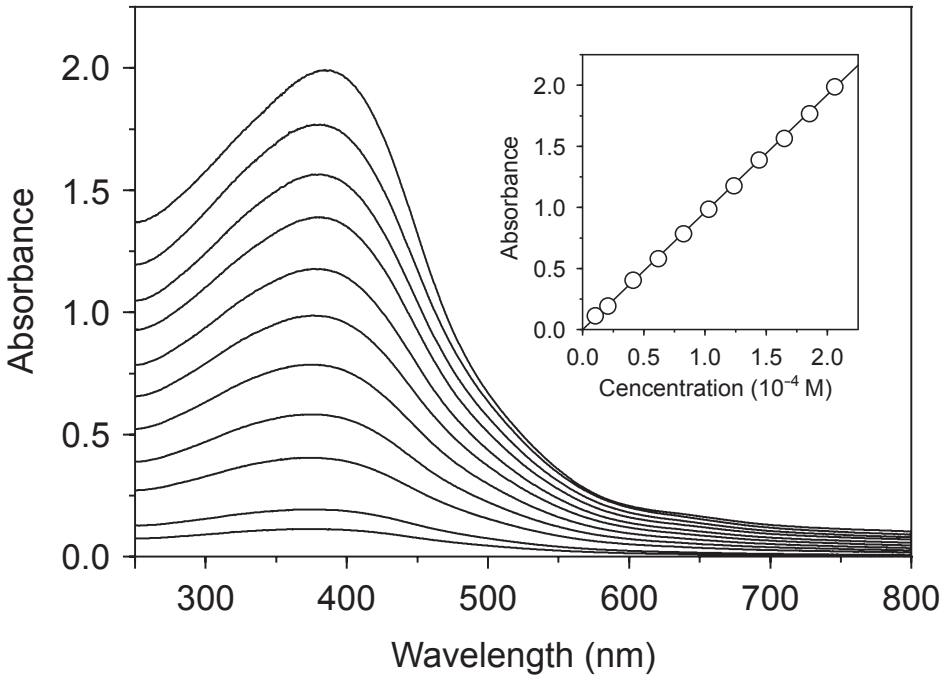

Figure 1.12. UV-Vis absorption spectra of colloidal suspension as a function of the nanosheet concentration. The concentrations from bottom to top are 1.03×10^{-5}, 2.06×10^{-5}, 4.12×10^{-5}, 6.18×10^{-5}, 8.24×10^{-5}, 1.03×10^{-4}, 1.24×10^{-4}, 1.44×10^{-4}, 1.65×10^{-4}, 1.85×10^{-4}, and 2.06×10^{-4} M, respectively. The inset shows the plot of absorbance at 380 nm against monosheet concentration, and the solid line corresponds to the fit indicating the molar extinction coefficient of 9.6×10^{3} M^{-1} cm^{-1}.

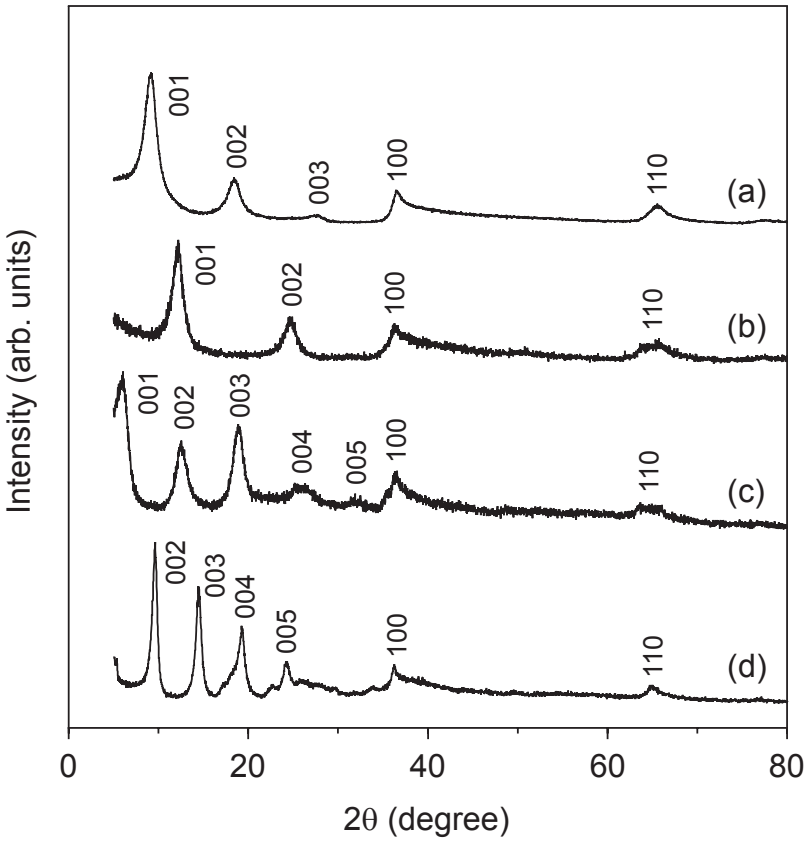

Figure 1.13. Powder X-ray diffraction patterns of (a) dried aggregate TMA/MnO_2, (b) self-assembled K/MnO_2, (c) self-assembled TTF/MnO_2, and (d) self-assembled BEDO-TTF/MnO_2.

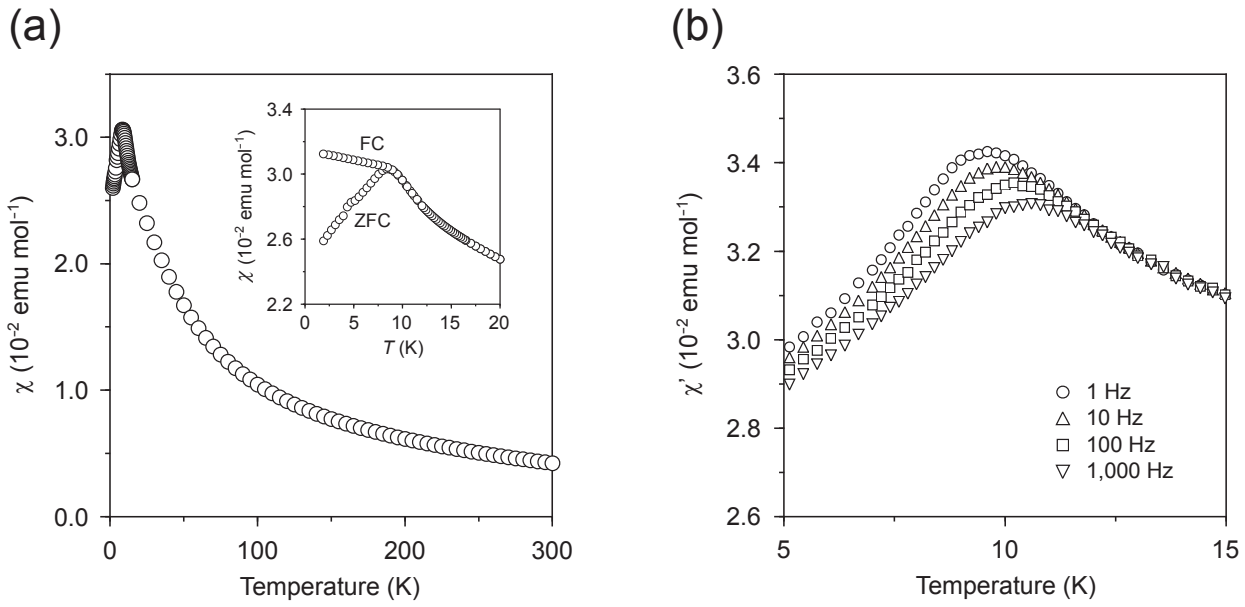

Figure 1.14. Temperature dependence of magnetic susceptibility of the dried aggregate TMA/MnO_2. (a) DC magnetic susceptibility (χ) under an applied magnetic field of 1 kOe. Above 20 K, the χ value follows the Curie-Weiss law with Curie constant of 1.44 emu K mol^{-1} and Weiss temperature of –36.4 K. The inset shows the low-temperature range of χ showing the difference between the zero field cooled (ZFC) and field cooled (FC) susceptibilities. (b) In-plane AC magnetic susceptibility (χ') at different frequencies (1, 10, 100, and 1,000 Hz).

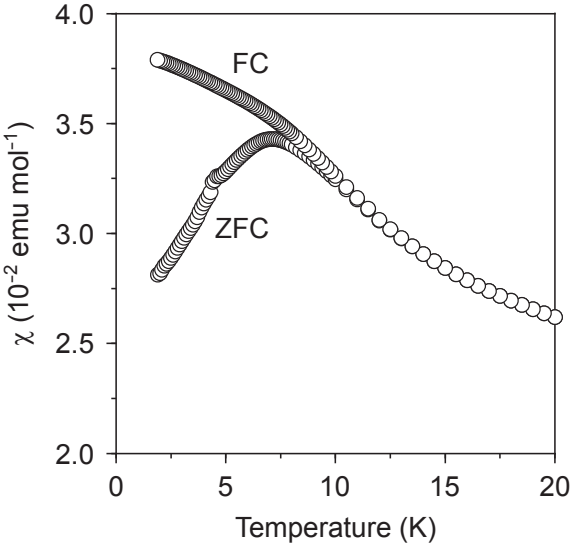

Figure 1.15. Temperature dependence of DC magnetic susceptibility (χ) of $K_{0.45}MnO_2 \cdot H_2O$ obtained by the sintering method. An applied magnetic field is 1 kOe. Spin glass behavior was observed as colloidal aggregate TMA/MnO_2 (Fig. 1.14).

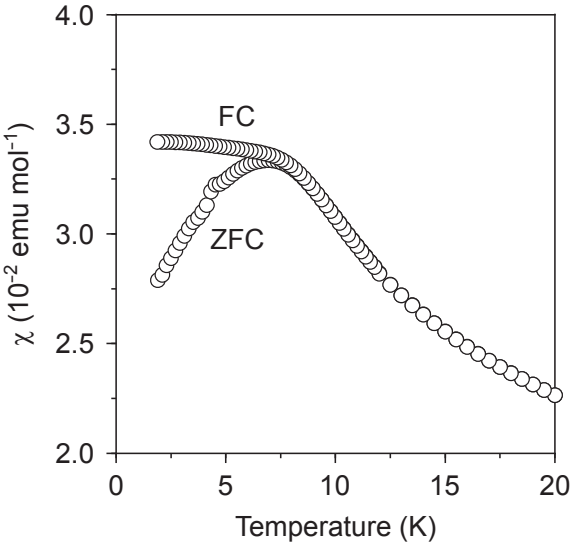

Figure 1.16. Temperature dependence of DC magnetic susceptibility (χ) of $H_{0.2}MnO_2 \cdot 0.63H_2O$ obtained by the acid treatment of sintered $K_{0.45}MnO_2 \cdot H_2O$. An applied magnetic field is 1 kOe. Spin glass behavior was observed as colloidal aggregate TMA/MnO_2 (Fig. 1.15).

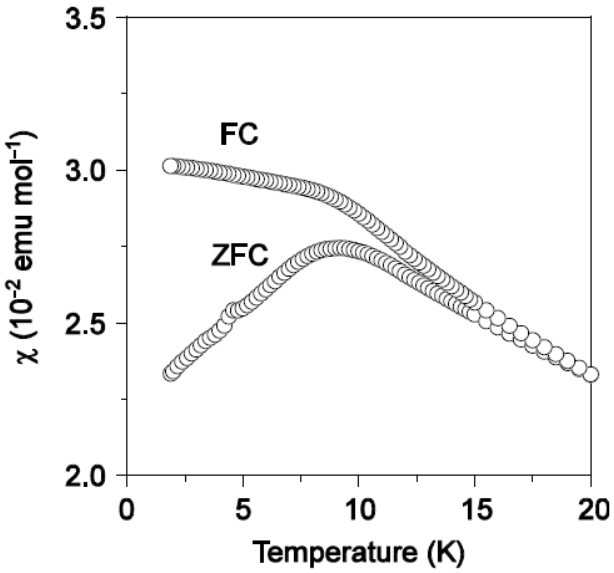

Figure 1.17. Temperature dependence of DC magnetic susceptibility (χ) of colloidal aggregate $TMA_{0.20}MnO_2 \cdot 0.2H_2O$, which was fabricated using the MnO_2 monosheets obtained by the conventional top-down approach. An applied magnetic field is 1 kOe. Spin glass behavior was observed at around 10 K as dried aggregate TMA/MnO_2 obtained by my processing (Figure 1.13).

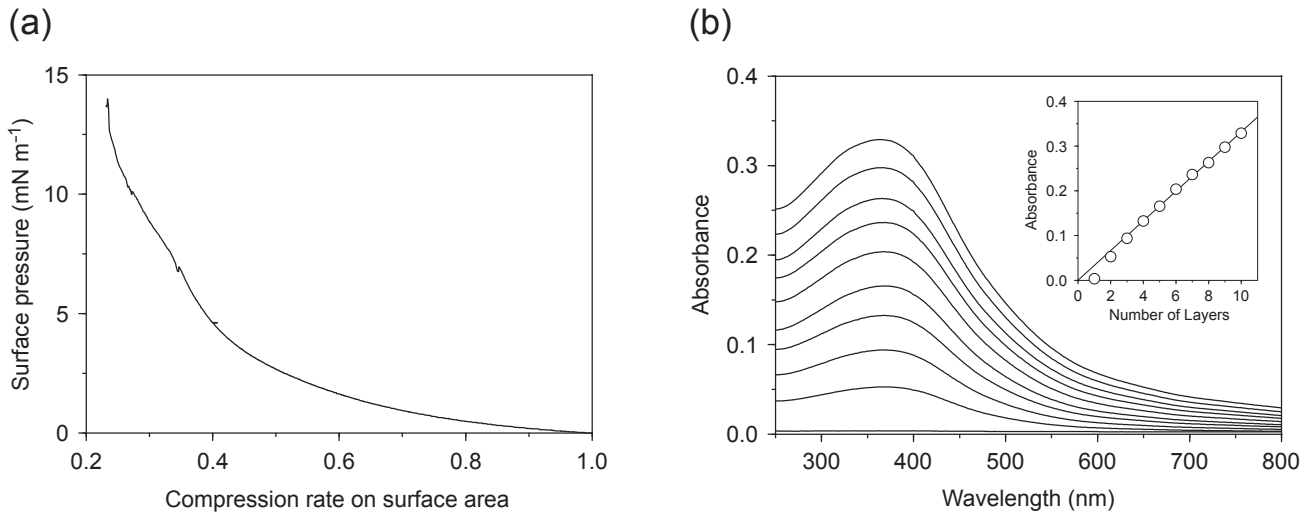

Figure 1.18. (a) Surface pressure-area (π–A) isotherm of the MnO_2 monosheets in the diluted suspension (0.01 g L^{-1}). The initial surface area of the subphase was 130 cm^2. The values in the horizontal axis of the isotherm indicate the relative surface area against the initial one. (b) UV-Vis absorption spectra of the LB films as a function of the number of layers (1–10). The inset shows the plot of absorbance at 368 nm against the number of layers.

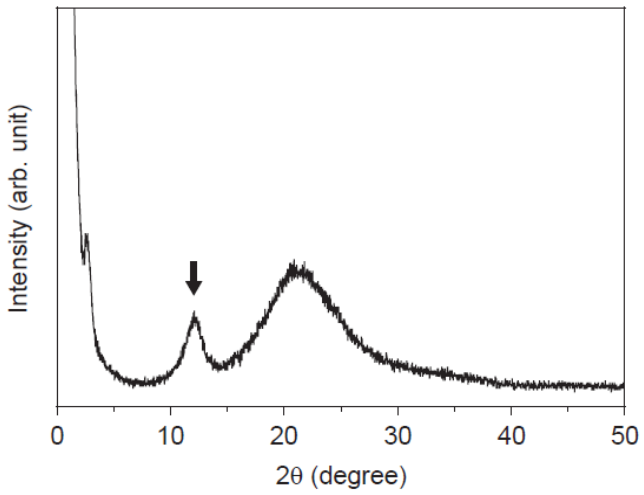

Figure 1.19. Powder XRD pattern of LB film with 30 layers of MnO_2 monosheets. A peak at around 2 θ = 12° (arrow) can be readily assigned to the (001) reflection, corresponding to the interlayer spacing of 0.73 nm. A broad peak centered at 2θ = 21° is originated from the fused silica substrate.

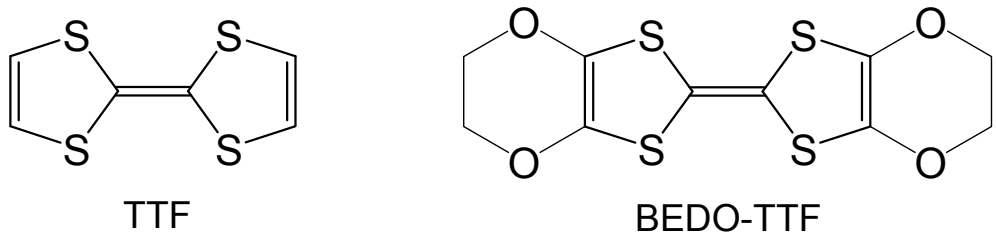

Scheme 1.1. Molecular structures of TTF and BEDO-TTF.

Chaper 2:

One-Pot Synthesis of Co-Substituted Manganese Oxide Nanosheets and Physical Properties of These Lamellar Aggregates

2.1 Introduction

Layered transition-metal (TM) oxides such as $RbCa_2Nb_3O_{10}$,[1] K_xMnO_2,[2] and $Cs_xTi_{2-x/4}\square_{x/4}O_4$[3] have exchangeable alkali cations between chemically inert metal-oxide layers (i.e., $[Ca_2Nb_3O_{10}]^-$, $[MnO_2]^{x-}$, $[Ti_{2-x/4}\square_{x/4}O_4]^{x-}$). Reactions with bulky organic molecules in aqueous solution at low temperatures allow these TM oxides to exfoliate into ultra-thin objects, termed often as 'nanosheets'.[4] The utmost feature of the TM oxide nanosheets is their exceptionally high specific surface area, rendering them promising candidates for a variety of applications, especially photocatalysis[5] and electrodes of electrochemical devices.[6-8] Another point of interest is a turbostratic structure when the nanosheets are aggregated; It is known that a $LiMnO_2$ cathode, obtained by the aggregation of MnO_2 nanosheets, suppresses the undesired phase transformation to a cubic spinel phase during Li charge/discharge process.[6]

However, the synthesis of TM oxide nanosheets usually requires multistep processing, involving a high-temperature solid-state reaction (to yield a thermodynamically stable phase, e.g. $RbCa_2Nb_3O_{10}$), a protonation of interlayer alkali metal ions (to yield, e.g. $HCa_2Nb_3O_{10}$), and an acid-base reaction with aqueous solution of quaternary ammonium cations (to finally yield negatively-charged nanosheets, e.g. $[Ca_2Nb_3O_{10}]^-$, in the form of colloidal suspension). Such a multi-step processing would be cumbersome considering future applications.

Recently, two reports were directed toward simplifying synthetic procedure; titanic and manganese oxide nanosheets.[9,10] Tae *et al.* reported on a rapid single-step synthesis of TiO_2 nanosheets through hydrolysis of titanium (IV) tetraisopropoxide in a tetramethyl ammonium hydroxide (TMA·OH) solution.[9] The author also showed a rapid single-step synthesis of MnO_2 nanosheets by oxidazing Mn(II) ions in a TMA·OH solution at room temperature.[10] Since the latter method uses $Mn(II)Cl_2$ aq as a manganese source, the addition of other soluble TM chloride may offer a possibility to change and control the chemical composition of the nanosheets. In particular, the $(Mn,Co)O_2$ system would be interesting as a partial Co-for-Mn substitution in $LiMnO_2$ is known to reduce the structural instability and improve the cycling performance as a cathode with a stable capacity of about 200 mAh/g.[11] In this study, a one-pot synthesis of the solid solution $(Mn_{1-x}Co_x)O_2$ nanosheets was presented. The substitution effects on structural, photo absorption, and magnetic characteristics were also investigated.

2.2. Experimental Section

A. Synthesis and Sample Preparation

Typically, for the synthesis of $(Mn_{1-x}Co_x)O_2$ (x = 0.00, 0.05, 0.11, 0.15, 0.20, 0.26, and 0.29) nanosheets, 20 mL of a mixture of 1.2 M H_2O_2 and 1.2 M TMA·OH was added into a 10 mL of 0.6 M MCl_2 aqueous solution consisted of $MnCl_2$ and $CoCl_2$ in a nominal mole ratio x_0, where x_0 =

Co/(Co+Mn). The resulting suspensions were stirred vigorously overnight in open air at 40 °C to let the reaction proceed further.

Lamellar aggregates of $K_y(Mn_{1-x}Co_x)O_2 \cdot zH_2O$ were obtained by mixing the colloidal suspensions of as-prepared $(Mn_{1-x}Co_x)O_2$ nanosheets with a KCl aqueous solution; typically, 10 mL of suspensions of $(Mn_{1-x}Co_x)O_2$ nanosheets (0.1 M) was added dropwise into 50 mL of 1 M KCl aqueous solution within 1 minute at 40 °C. Immediately after the addition, flocculation occurred in the mixed solution, and the black precipitates were formed. The precipitates were filtered off, washed with copious amounts of distilled water, and then air-dried for 1 day.

B. Characterization

A Seiko SPA400 atomic force microscopy (AFM) instrument was employed to visualize the surface topography of the nanosheets. Measurements were carried out in tapping mode with a silicon-tip cantilever having a force constant of 20 Nm^{-1}. Samples were deposited onto fluorinated mica substrate (Fluoro-Phologopite, Topy Industry Ltd.) precoated with poly(ethyleneimine) by spin-coating (1000 rpm for 15 s and 2000 rpm for 30 s) of a 0.1 g L^{-1} colloidal suspension. UV-Vis absorption spectra were taken in a quartz cell with light path length of 1 cm using a Shimadzu UV-3100 spectrophotometer (200-800 nm). Powder X-ray diffraction (XRD) measurements were carried out with a MAC Science M18XHF diffractometer using Cu $K\alpha$ radiation in a 2θ range of 5–80 °. The powder sample was placed on a glass slide. Scanning electron microscopy (SEM) and energy dispersive X-ray spectroscopy (EDS) experiments were conducted with a JEOL JSM-5510LVN instrument operating at 20 kV. TG/DTA thermograms were taken on a Shimadzu DTG-60M instrument under nitrogen atmosphere at a 10 °C min^{-1} heating rate. The samples for SEM and EDS measurements were mounted on a carbon tape. A Quantum Design MPMS-XL superconducting quantum interference device (SQUID) magnetometer was used to collect DC magnetic susceptibility data between 2 K and 300 K.

2.3 Results and Discussions

2.3.1 Synthesis and Morphology of Nanosheests

After mixing MCl_2 and $TMA{\cdot}OH/H_2O_2$ solutions, red-purple solutions readily became dark-brown, and then, with further stirring for 6 hours, changed into semitransparent colloidal suspensions. All the obtained suspensions showed Tyndall light scatterings, strongly suggesting the formation of nanoobjects dispersed in the aqueous suspensions. Additionally, the color change from yellowish brown to dark-yellowish brown with increasing x_0 also indicates a probable substitution of Mn by Co in the nanoobjects, as seen in Figure 2.1. Sheet-like structures were evident in SEM for freeze-dried samples (Figure 2.2). Thus it is possible that the suspensions consist of colloidal particles with thin film morphologies.

Shown in Figure 2.3 is an AFM image of the colloidal particles for x_0 = 0.20 deposited onto fluorinated mica substrate. It displays a sheet-like structure with a uniform thickness of 0.9 nm and lateral sizes of several tens to hundreds nanometer. The 0.9 nm thickness is identical to that of non-substituted MnO_2 nanosheets.[10] The lateral size is also comparable to that of MnO_2 nanosheets. Additionally, homogeneous distributions of Mn and Co in these nanosheets were confirmed by EDS mapping for freeze-dried samples.

2.3.2 Structural and Compositional Analysis of Lamellar Aggregates

Figure 2.4 shows XRD profiles of lamellar aggregates obtained by adding nanosheets suspensions into KCl aqueous solution. All the patterns showed similar features to the non-substituted sample of x_0 = 0.00.[10] For example, the XRD pattern of the x_0 = 0.20 sample shows two basal reflections of 001 to 002 centered at 12.31 ° and 24.86 ° respectively, and asymmetrical in-plane reflections of 100 and 110 at 36.76 ° and 66.04 ° in a hexagonal unit cell; the cell constants are determined to be a = 2.824(4) Å and c = 7.17(14) Å. The asymmetrical in-plane reflections are characteristic of the turbostratic stacking

patterns of MO_2 sheets.[6] Thus following the discussion in ref [10], the author conclude the formation of the layered aggregates of K/(Mn,Co)O_2 comprised of (Mn,Co)O_2 layer with interlayer K^+ ions in monolayer hydrated phase.

The cell volume of these lamellar aggregates is plotted as a function of x_0 in Figure 2.5. For $0.00 \leq x_0 \leq 0.20$, the cell volume shrinks linearly with increasing x_0. Given almost constant values of y and z (estimated by EDS and TG, see the next paragraph), the linear dependence in this region strongly indicates a successful formation of the solid solution, and is in accordance with the smaller effective ionic radius of Co^{3+} (0.545 Å, in low-spin state) as compared with Mn^{3+} (0.58 Å, in low-spin state) with an octahedral coordination.[14] On the other hand, beyond $x_0 = 0.20$, the lattice parameter does not change any more. A similar feature, namely, the deviation from the Vegard's law for $x_0 > 0.2$, is observed in the band gap energy of the (Mn,Co)O_2 nanosheets colloids deduced from the absorption threshold in UV-Vis spectra (see the next section). Thus, the author conclude that the solubility limit is $x_0 \sim 0.20$; hereafter, the compositional and physical properties are discussed for only $x_0 \leq 0.20$ samples.

Chemical compositions for all the lamellar aggregates ($0.00 \leq x_0 \leq 0.20$) were estimated by the EDS analysis, and the result is summarized in Table 1. The water content z was estimated to be 0.75 - 1.0 based on the weight loss at around 150 °C in TGA profiles. The chemical compositions of metal ions, K, Mn, and Co, were calculated based on the assumptions that all Co ions are replaced at the Mn-site in the MnO_2 layer and that the potassium ions are the only source of positive charge for the interlayer species. Note that these lamellar aggregates should not contain other cations such as H^+ or H_3O^+ in the interlayer because of the basic condition for flocculating the nanosheets (i.e. alkaline solution of TMA·OH). It is seen that x in $K_y(Mn_{1-x}Co_x)O_2 \cdot zH_2O$ is nearly equal to the nominal ratio x_0 (Table 1), and the potassium content y is around 0.20 independent with x, indicating that the average valence of transition metal ions is about +3.80. Namely, the charge density of inorganic layer is inert upon Co-for-Mn substitution.

2.3.3 Optical properties of $(Mn_{1-x}Co_x)O_2$ *Nanosheets*

Figure 2.6 shows UV-Vis absorption spectra of the 0.1 mM colloidal suspensions of $(Mn_{1-x}Co_x)O_2$ nanosheets ($0.00 \leq x \leq 0.20$). A pronounced absorption centered at around 380 nm and a weak absorption centered at around 650 nm can be seen. The 380 nm absorption is also seen in the non-substituted MnO_2 nanosheets,[10] and this absorption can be identified as d-d transition of Mn^{4+} ions in an octahedral coordination.[12] The 650 nm absorption, not found in the non-substituted sample, can be assigned to d-d transition of octahedrally coordinated Co^{3+} ions.[13] Notably, the absorption intensity at 380 nm hardly changes upon substitution. This indicates that the total amount of Mn^{4+} in the nanosheets kept remained. On the contrary, the absorption intensity at around 650 nm becomes greater with increasing Co content (Figure 2.7). Knowing that the charge density of the nanosheet is inert upon Co substitution, it can be considered that the Co ions are in a trivalent state.

The effect of the Co substitution on the electronic structures can be seen in the absorption edge for the 380 nm peak. For $x = 0.00$, the absorption edge is located at 513 nm corresponding to a band gap energy of 2.43 eV, and this value is close to that of non-substituted MnO_2 nanosheets (2.2 eV) as measured by electrochemical method.[12] The Co substituted nanosheets exhibit absorption edges at a shorter wavelength, thereby corresponding to a larger band gap. For example, the band gap energy for $x = 0.20$ is estimated as 2.61 eV. Such a blue-shift in adsorption edges can be attributed to the increased crystal field stabilization energy, through the M-O bond shrinkage. As shown in Figure 2.8, for $0.00 \leq x \leq 0.20$, the band gap energy changes linearly with x. Note that, beyond $x = 0.20$, the band gap is constant, consistent with the lattice parameter evolution that conclude that the solubility limit is $x \sim 0.20$ (Figure 2.9).

2.3.3 Magnetic Properties of Lamellar Aggregates

The temperature dependence of magnetic susceptibilities $\chi(T)$ of lamellar aggregates, $K_y(Mn_{1-x}Co_x)O_2 \cdot zH_2O$ ($0.00 \leq x \leq 0.20$) in both zero-field cooling (ZFC) and field-cooling (FC) processes measured at 0.1 T is presented in Figure 2.10. All of the curves exhibit a Curie-Weiss behavior at high

temperatures (T > 20 K) and a spin-glass like behavior below 10 K. The effective magnetic moment μ_{eff} and Weiss-temperature θ calculated from the Curie-Weiss fitting are shown in Table 1. It is seen that μ_{eff} and θ vary systematically upon substitution. The effective magnetic moment shows a gradual decrease with increasing Co (Figure 2.11a). The reduction rate $\Delta\mu_{eff}/\Delta x = 2.51\mu_B$ might be explained in terms of the replacement of the low-spin Mn^{3+} ion (μ_{eff} = 2.83 μ_B) vs. the low-spin Co^{3+} (μ_{eff} = 0), as indicated by EDS analysis and UV-Vis spectra. The decrease in θ with x (or increase in antiferromagnetic interaction) would be explained by the enhanced M-O-M superexchange interactions arising from the shortened M-O bond length

2.4 Conclusions

The author have synthesized the $(Mn_{1-x}Co_x)O_2$ nanosheets through one-pot method using mixed solution consisted of $MnCl_2$ and $CoCl_2$. The cell volumes of these lamellar aggregates showed linier shrinkage upon the Co substitution, in the region of $0.00 \leq x \leq 0.20$. The composition x can be controlled continuously by nominal mole ratio x_0 of the starting solution. The charge density of inorganic layer is inert upon Co-for-Mn substitution. The substitution effects were observed in UV-Vis spectra and magnetic properties; the increase of optical band gap energies and antiferromagnetic interactions are suggested.

References

[1] (a) Schaak, R. E.; Mallouk, T. E. *Chem. Mater.* **2002**, *14*, 1455. (b) Kodenkandath, T. A.; Kumbhar, A. S.; Zhou, W. L.; Wiley, J. B. *Inorg. Chem.* **2001**, *40*, 710.

[2] (a) Omomo, Y.; Sasaki, T.; Wang, L.; Watanabe, M. *J. Am. Chem. Soc.* **2003**, *125*, 3568. (b) Liu, Z.-h.; Ooi, K.; Kanoh, H.; Tang, W.-p.; Tomida, T. *Langmuir* **2000**, *16*, 4154.

[3] (a) Sasaki, T.; Watanabe, M. *J. Am. Chem. Soc.* **1998**, *120*, 4682. (b) Sasaki, T.; Watanabe, M.; Hashizume, H.; Yamada, H.; Nakazawa, H. *J. Am. Chem. Soc.* **1996**, *118*, 8329.

[4] Sasaki, T. *J. Ceram. Soc. Jpn.* **2007**, *115*, 9.

[5] (a) Domen, K.; Ebina, Y.; Ikeda, S.; Tanaka, A.; Kondo, J. N.; Maruya, K. *Catal. Today* **1996**, *28*, 167. (b) Takagaki, A.; Sugisawa, M.; Lu, D.; Kondo, J. N.; Hara, M.; Domen, K.; Hayashi, S. *J. Am. Chem. Soc.* **2003**, *125*, 5479.

[6] Wang, L.; Takada, K.; Kajiyama, A.; Onoda, M.; Michiue, Y.; Zhang, L.; Watanabe, M.; Sasaki, T. *Chem. Mater.* **2003**, *15*, 4508.

[7] Sugimoto, W.; Iwata, H.; Yasunaga, Y.; Murakami, Y.; Takasu, Y. *Angew. Chem. Int. Ed.* **2003**, *42*, 4092.

[8] Kadoma, Y.; Uchimoto, Y.; Wakihara, M. *J. Phys. Chem. B* **2006**, *110*, 174.

[9] Tae, E. L.; Lee, K. E.; Jeong, J. S.; Yoon, K. B. *J. Am. Chem. Soc.* **2008**, *130*, 6534.

[10] Kai, K.; Yoshida, Y.; Kageyama, H.; Saito, G.; Ishigaki, T.; Furukawa, Y.; Kawamata, J. *J. Am. Chem. Soc.* **2008**, *130*, 15983.

[11] Franger, S.; Bach, S.; Pereira-Ramos, J. P.; Baffier, N. *Ionics* **2000**, *6*, 470.

[12] Sakai, N.; Ebina, Y.; Takada, K.; Sasaki, T. *J. Electrochem. Soc.* **2005**, *152*, E384.

[13] Ghosh, P.; Mahanty, S.; Raja, M. W.; Basu, R. N.; Maiti, H. S.; *J. Mater. Res.* **2007**, *22*, 1162.

[14] Shannon, R. D. *Acta Cryst.***1976**, *A32*, 751.

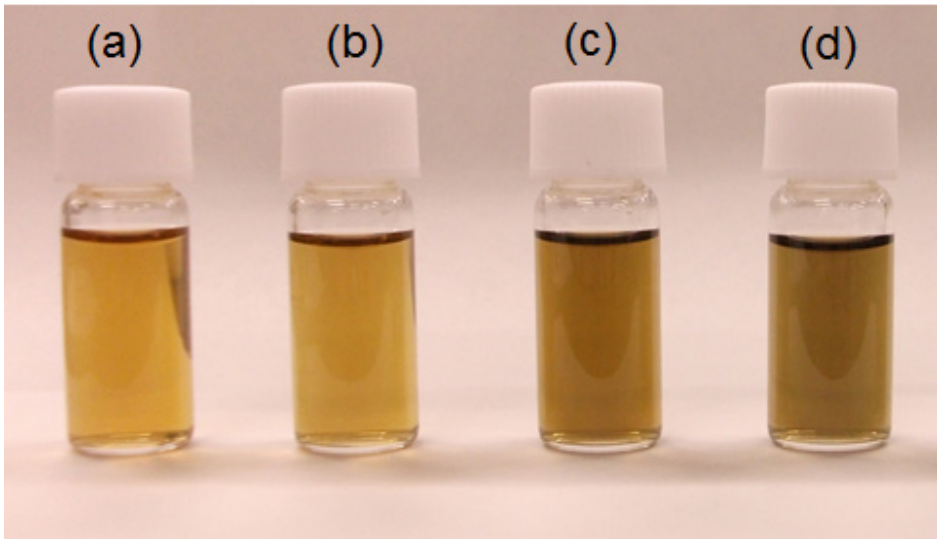

Figure 2.1. Photographs of colloidal suspension of $(Mn_{1-x}Co_x)O_2$ nanosheets (0.1 mM). (a) x_0 = 0.05, (b) x_0 =0.11, (c) x_0 = 0.15, (d) x_0 = 0.20, respectively. x_0 indicates the nominal ratio of the cobalt ions.

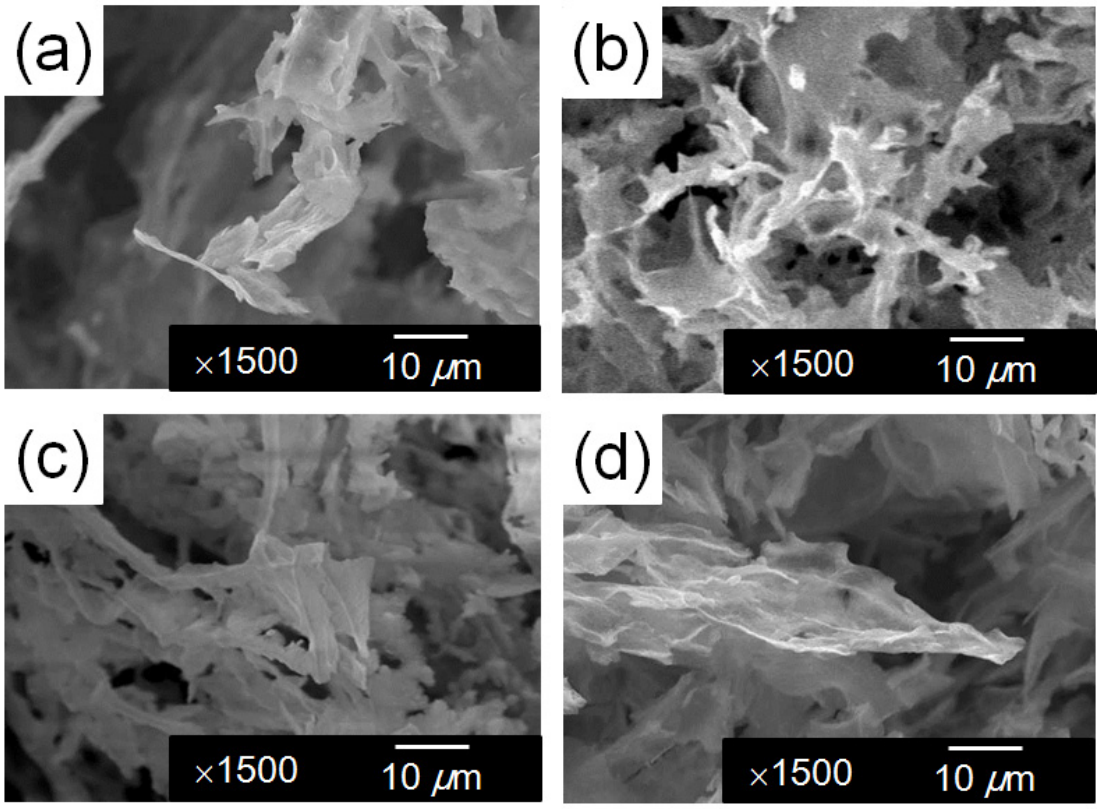

Figure 2.2. SEM images of freeze-dried aggregate of TMA/$(Mn_{1-x}Co_x)O_2$. (a) x_0 = 0.05, (b) x_0 =0.11, (c) x_0 = 0.15, (d) x_0 = 0.20, respectively.

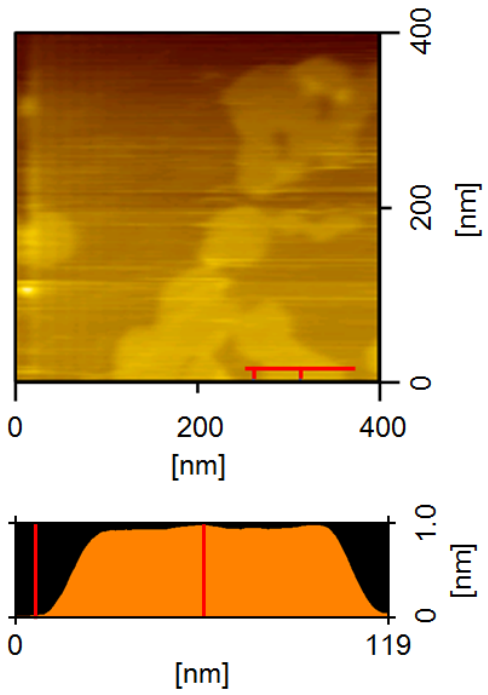

Figure 2.3. (top) Tapping-mode AFM image of $(Mn_{1-x}Co_x)O_2$ monosheets (x_0 = 0.20), and (down) height profile along the red line in the image.

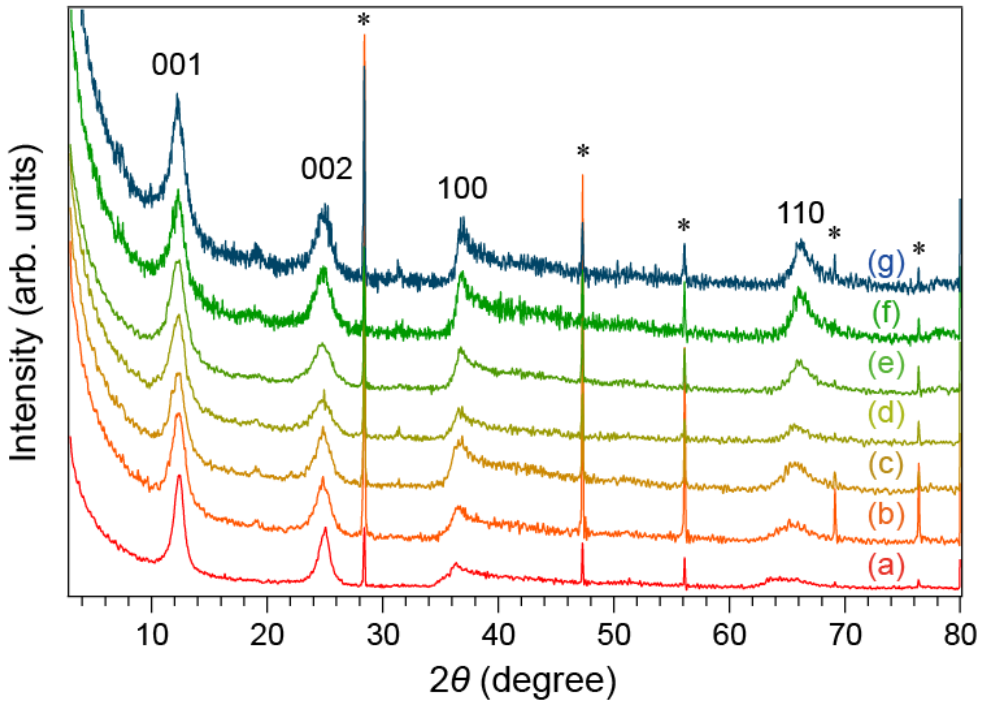

Figure 2.4. Powder X-ray diffraction patterns of lamellar aggregates of $K(Mn_{1-x}Co_x)O_2 \cdot zH_2O$. (a) x = 0, (b) x = 0.05, (c) x = 0.11, (d) x = 0.15, (e) x = 0.20, (f) x = 0.26, (g) x = 0.30, respectively.

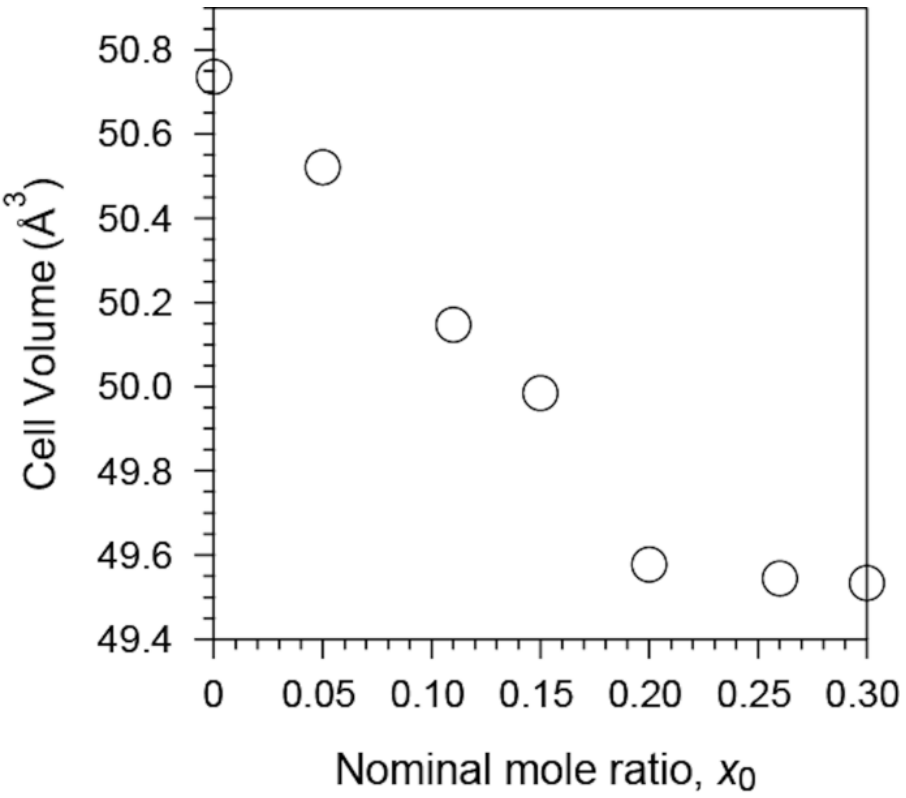

Figure 2.5. Variation in cell volume of the lamellar aggregates, with x_0 ($0 \leq x_0 \leq 0.29$).

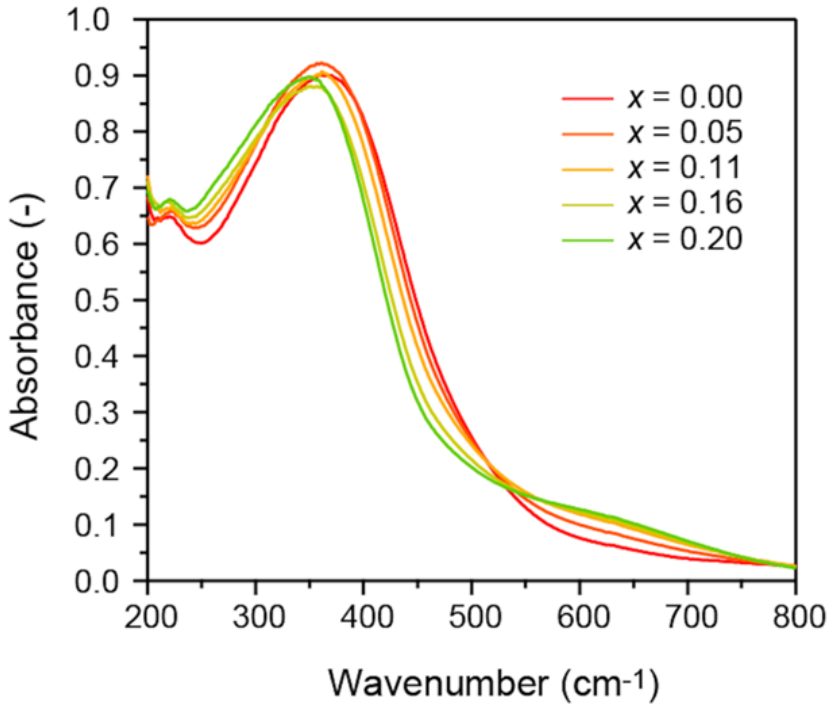

Figure 2.6. UV-Vis absorption spectra of the colloidal suspension of $(Mn_{1-x}Co_x)O_2$ nanosheets (0.1 mM, $0 \leq x \leq 0.20$).

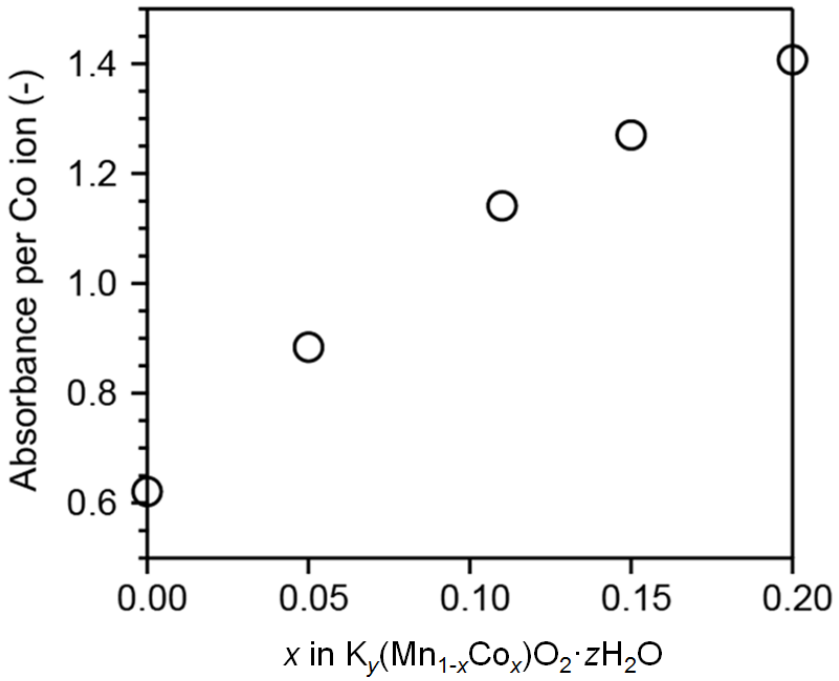

Figure 2.7. Variation in adsorption intensity at 650 nm with composition x ($0 \leq x \leq 0.2$) per Co ions.

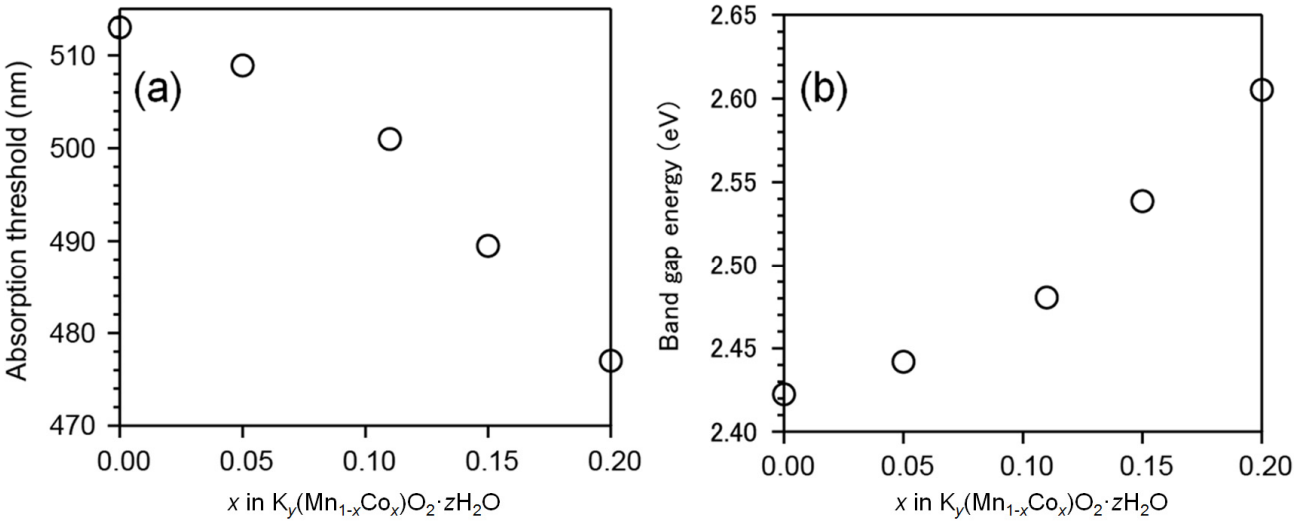

Figure 2.8. Variation in (a) adsorption threshold, and (b) band gap energies of Mn ions, with composition x ($0 \leq x \leq 0.2$).

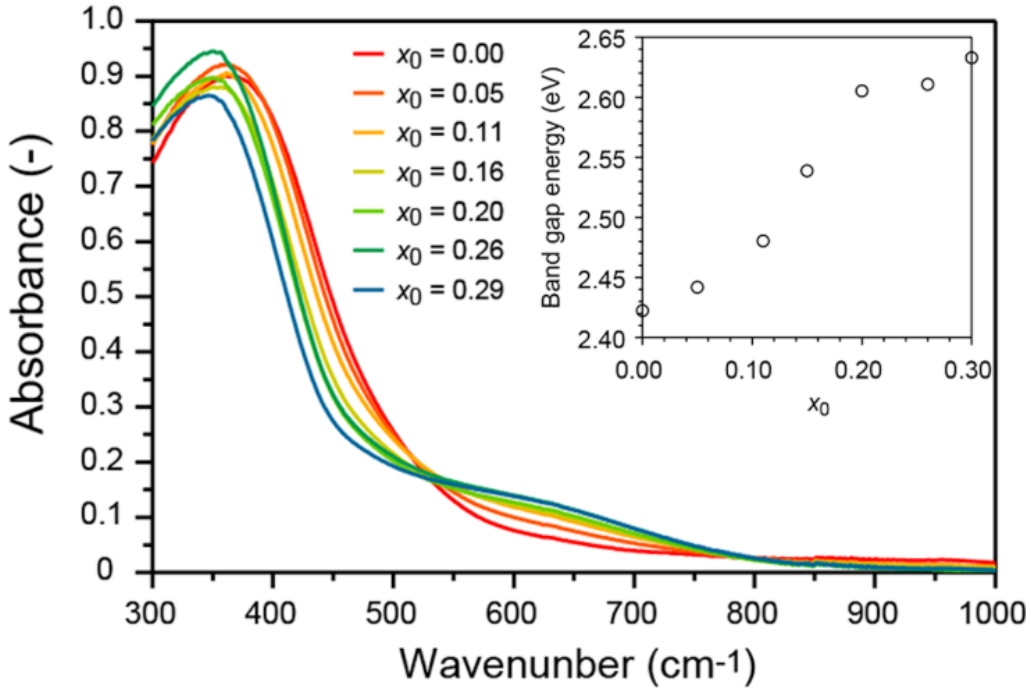

Figure 2.9. UV-Vis absorption spectra of the colloidal suspension with $0 \leq x_0 \leq 0.29$ (0.1 mM). Inset: variation in band gap energies of Mn ions, with x_0.

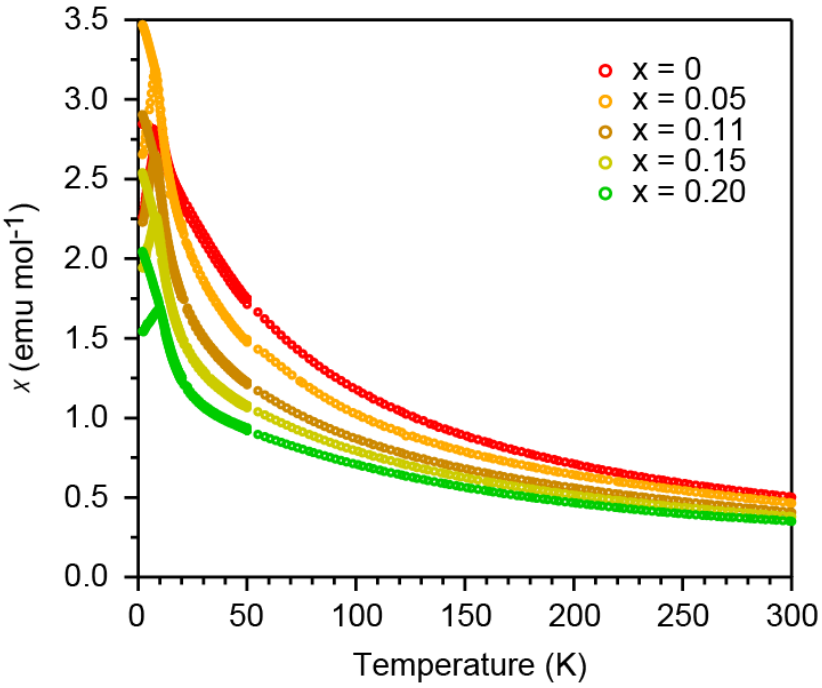

Figure 2.10. Temperature dependence of magnetic susceptibility of the dried aggregate, $K_y(Mn_{1-x}Co_x)O_2 \cdot zH_2O$ ($0 \leq x \leq 0.2$). The data were collected under an applied of 0.1 T.

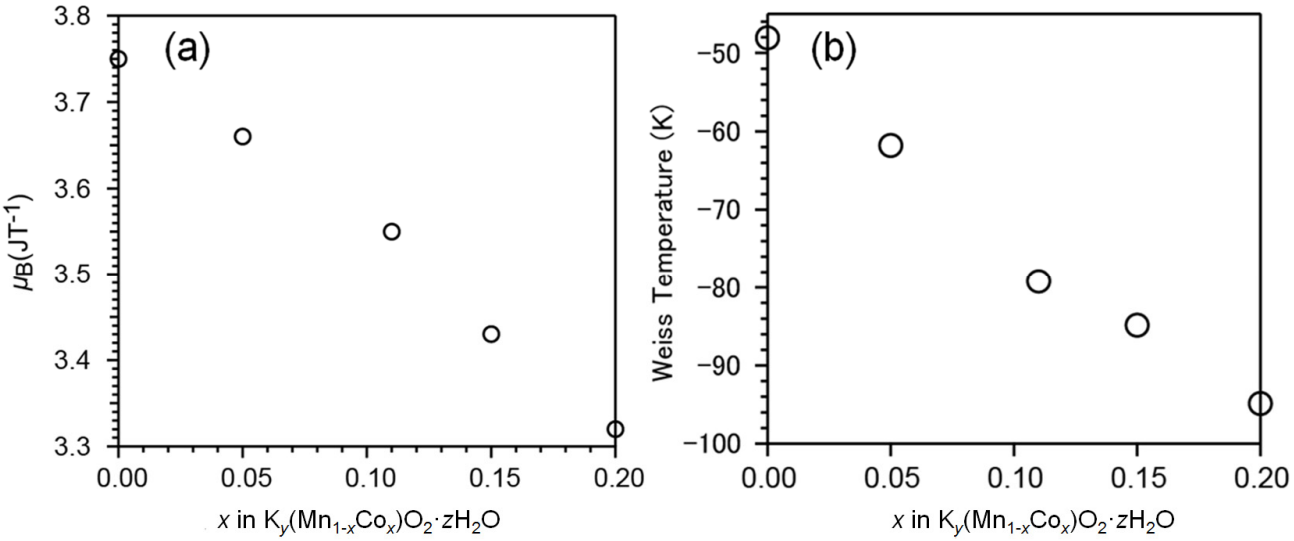

Figure 2.11. Variation of magnetic moment, μ_B, with a composition x ($0 \leq x \leq 0.2$).

Table 2.1. Compositions of $K_y(Mn_{1-x}Co_x)O_2 \cdot zH_2O$ (determined by EDX), cell volume, and magnetic parameters (Weiss temperature and effective magnetic moment).

x_0	Composition	Cell volume (Å^3)	Weiss temperature (K)	μ_{eff}/μ_B
0.00	$K_{0.21}MnO_2$	50.74 (3)	- 48.06 (1)	3.75
0.052	$K_{0.20}(Co_{0.05}Mn_{0.95})O_2$	50.52 (4)	- 61.80 (2)	3.73
0.110	$K_{0.20}(Co_{0.11}Mn_{0.89})O_2$	50.15 (2)	- 78.09 (2)	3.55
0.156	$K_{0.21}(Co_{0.15}Mn_{0.85})O_2$	49.99 (3)	- 84.87 (1)	3.43
0.197	$K_{0.20}(Co_{0.20}Mn_{0.80})O_2$	49.58 (3)	- 94.86 (4)	3.32
0.264	–	49.54 (2)	–	–
0.294	–	49.53 (4)	–	–

Chaper 3:

Preparation and Formation Mechanism of a *n*-Butylammonium/MnO_2 Layered Hybrid *via* a One-Pot Synthesis under Moderate Conditions

3.1 Introduction

Layered inorganic compounds comprising of negatively-charged inorganic host layers and interlayer cations (e.g. layered perovskites,[1] layered oxides with CdI_2-type host layers,[2,3] and clays,[4] etc.) can be modified by soft chemistry procedures, such as (de)intercalation or ion-exchange. In terms of obtaining organic/inorganic layered hybrids, ion-exchange reactions are a common method because of its broad scope to introduce various organic cations. Here, organic cations such as alkyl ammonium are inserted into interlayer galleries by stirring the layered host in a solution of the organic species. Such organic/inorganic layered hybrids have received a tremendous amount of interest due to their structural flexibility and diversity and potential applications in photochemistry (e.g. porphyrin/clay hybrids, tris(2,2'-bipyridyl) ruthenium/niobium oxide hybrids),[5,6] electrochemistry (e.g. polyaniline/MnO_2

hybrids, alkyl ammonium/RuO_2 hybrids),[5,7] catalysis (e.g. alkyl ammonium/zeolite hybrids),[5,8] and so on. However, the organic intercalation is accompanied by large interlayer expansions. Such a process is often energetically uphill, since it requires overcoming the Coulombic interaction between the negative host layers and interlayer precursor cations. Due to this requirement and its template-dependent synthetic strategy, the preparation of these hybrids results in complicated multi-step reaction. The initial step is a synthesis of inorganic hosts through a high temperature solid state or hydrothermal synthesis, and the second is an acid treatment of them. The acid treatment is an extra step, but is at times necessary since the subsequent acid-base reaction can provide the driving force for the next, otherwise sometimes energetically unfavorable intercalation. Additionally, the subsequent acid-base or guest exchange reaction can take up to a week. Therefore, the synthesis of layered hybrids involves complicated reaction steps and long processing times totaling a few weeks as a whole.[1a,9]

Among the layered host materials, layered manganese oxides, $A_xMnO_2{\cdot}yH_2O$ (A = Li, Na, K,…), have much attention due to their potential applications as ion sieves,[10] molecular sieves,[11] cathode materials for Li secondary batteries,[12] and precursors for pillared- or tunnel-structured manganese oxides.[13] Birnessite is a common layered manganese oxide comprised of an inorganic host layer with edge-shared MnO_6 octahedra, interlayer alkali (earth) metal ions, and a single layer of water of crystallization.[14] Several solution processes, such as oxidation,[15] redox precipitation,[16] sol-gel reactions,[17] and hydrothermal processes[18] are known for the synthesis of birnessite, and the mechanistic features of crystallization have been reported.[19] On the other hand, there have been limited reports on the rapid synthesis of organic/MnO_2 layered hybrids. Chen *et al.* synthesized a well-ordered cetyltrimethylammonium/MnO_2 (CTA/MnO_2) via redox reaction between $CTAMnO_4$ and $MnCl_2$ in aqueous solution, by the aid of the micelle-forming ability of CTA^+.[20] In another example, Wang *et al.* synthesized a polyaniline/MnO_2 layered hybrid via reduction of aqueous $KMnO_4$ using oxidative polymerization of aniline. This material exhibits good power characteristics as a cathode material when incorporated into a lithium ion battery, due to its swelled layered structure, small particle size (5-10 nm),

and mesoporous structure (pore size ~ 4 nm).[7a] However, unlike birnessite, the formation mechanisms of these hybrid systems are still unknown.

In this work, a novel one-pot synthetic method for organic/inorganic layered hybrids involving manganese oxide was presented. The reaction methodology was hinted at by the author's recent finding of a room-temperature and single-step route to access MnO_2 nanosheets.[21] While metal oxide nanosheets are generally exfoliated by intercalation of bulky organic cations as the last step of the conventional multi-step reaction, the author's one-pot method produces MnO_2 nanosheets via template-free chemical oxidation of Mn(II) in the presence of tetramethylammonium (TMA^+) cations in aqueous solution (Figure 3.1a). Here, the author modified the one-pot synthesis by using a primary amine in place of the quaternary ammonium salt (Figure 3.1b). The larger van der Waals interaction and stacking ability of *n*-butylamine allows the formation of layered hybrid aggregates instead of exfoliated nanosheets. Such a feature is reasonable to clarify the formation mechanism of the organic/inorganic hybrids, which should be closely related to that of MnO_2 nanosheets due to the similarity in synthetic method. However, how the oxide host layers form is still unknown. The further elucidation of the reaction mechanism will be helpful for optimization of reaction conditions (e.g., reaction time, temperature, and mixing ratio of starting materials), removal of preventable impurities, and synthesis of a variety of organic/MnO_2 systems through the rapid synthetic procedure. From these points of view, the formation mechanism of the layered *n*-butylammonium/MnO_2 hybrid was also investigated.

3.2. Experimental Section

A. Synthesis

1. One-Pot synthesis of C4/MnO_2

Typically, 10 mL of an aqueous solution of 0.6 M $MnCl_2$ was added to 20 mL of a mixture of 1.2 M H_2O_2 and 0.2–2.0 M *n*-butylamine. A black polycrystalline precipitate was obtained immediately after mixing during vigorous stirring (Figure 3.1), irrespective of the nominal molar ratio *r* of *n*-butylamine/Mn. The solution was kept stirring at 40 °C to let the reaction proceed further. The precipitates were recovered at each reaction time by filtration, washed with copious amounts of distilled water, and then air-dried. The samples obtained by this one-pot method are hereafter abbreviated as C4/MnO_2. For comparison, *n*-butylammonium-intercalated MnO_2 was also synthesized by a multi-step reaction including a solid-state and ion-exchange reactions, which required about two weeks.[22,23] This sample prepared by a multi-step process is hereafter abbreviated as m-C4/MnO_2.

2. Synthesis of K_xMnO_2

Potassium-type birnessite (K_xMnO_2) was synthesized according to the literature.[1] To 9 mL of 0.5 M $KMnO_4$ (Wako, 99.3%) was added 1 mL of 0.05 M HNO_3 (Nacalai Tesque, GR) in a 60 mL Teflon vessel. The vessel was sealed in a stainless steel autoclave; then the solution was subjected to mild hydrothermal treatment at 170 °C for 4 days under autogenous pressure. After cooling to room temperature, the resulting black crystallites were separated by filtration, washed with *ca.* 50 mL of distilled water, and then dried overnight *in vacuo* (0.53 g). The K/Mn ratio was estimated to be 0.31 on the basis of EDS, showing the sample to be pure.

3. Synthesis of H/MnO_2

Typically, 0.52 g of K_xMnO_2 was added into 100 mL of 1 M HCl (Aldrich, 99.999%), and the suspension was stirred at room temperature for a week. The resulting blackish brown powder was separated by filtration, washed with *ca.* 50 mL of distilled water, and then dried overnight *in vacuo* (0.45 g). The K/Mn ratio was estimated to be 0.04 on the basis of EDS, indicating that about 90% of potassium ions were replaced by protons.

4. Synthesis of m-C4/MnO_2

Typically, 0.40 g of H/MnO_2 was added into 100 mL of distilled *n*-butylamine, and the suspension was stirred at room temperature for a week. The resulting blackish brown power was separated by filtration, washed with *ca.* 50 mL of distilled water, and then air-dried overnight (0.68 g). The amount of residual potassium remains almost unaltered by the acid-base reaction. Elemental analysis, in support of EDS, indicates the composition of (*n*-butylammonium)$_{0.17}K_{0.04}MnO_2 \cdot 0.3H_2O$ (Anal. Calcd for $C_{0.68}H_{2.64}K_{0.04}Mn_1N_{0.17}O_{2.3}$: C, 7.67; H, 2.50; N, 2.24%. Found: C, 7.64; H, 2.86; N, 2.32%), in which the formal valence on Mn (+3.79) is consistent with that of C4/MnO_2 obtained by the single-step approach.

B. Characterization

Powder X-ray diffraction (XRD) measurements were carried out with a MAC Science M18XHF and a Bruker D8 diffractometer using Cu Kα radiation at a scanning rate of 0.01 ° s^{-1} in a 2θ range of 5–80 °. The sample for the XRD experiments was placed on a glass slide. TG/DTA thermograms were taken on a Shimadzu DTG-60M instrument under nitrogen atmosphere (2 °C min^{-1} heating rate). Scanning electron microscopy (SEM) and energy dispersive X-ray spectroscopy (EDS) experiments were conducted with a JEOL JSM-5510LVN instrument operating at 20 kV. The samples for the SEM and EDS measurements were mounted on a carbon tape. FT-IR spectra were recorded on a Perkin-Elmer 1000 series spectrometer. The samples were pressed as KBr pellets. The pH of the solution was determined with a Horiba Model D51 pH meter.

3.3 Results and Discussions

3.3.1 Characterization of C4/MnO_2

XRD patterns of the as-prepared samples with different r (i.e. molar ratio of amine to manganese) obtained in the 24 hrs reaction are shown in Figure 3.2. The XRD profiles were drastically changed depending on r. At $r > 2.25$, the patterns are essentially identical to that of m-C4/MnO_2 obtained by the multi-step route (Figure 3.2e; a = 2.84 Å and c = 15.2 Å, hexagonal unit cell). This is a strong evidence of the formation of C4/MnO_2 through a one-pot method, that is, the first example of the one-pot synthesis of organic/MnO_2 layered hybrid by oxidizing manganese ions. Hereafter, the characterization, especially focusing on the sample at r = 4.00 will be discussed.

The formed C4/MnO_2 shows multiple higher order reflections between 0 ° and 25 ° with a d-spacing of 15.2 Å (Figure 3.2d). Assuming a layer thickness of MnO_2 (5.2 Å[26]) and the length of n-butylamine (~ 9.8 Å), the interlayer distance of 15.2 Å corresponds to a non-hydrated monolayer arrangement of n-butylammonium, with the alkyl chain almost perpendicular to the MnO_2 layers. The broad and asymmetric reflections at around 36.5°, and 63.6° are indexable as in-plane reflections of 100 and 110, respectively. These asymmetric reflections imply that each MnO_2 layer is shifted randomly and forms a disordered stacking system.[24] Such randomization of the layered structure reflects the lack of interlayer registry caused by the weak van der Waals interaction between the interlayer alkyl chains. There are unindexed peaks represented as an asterisk, which was also observed in the sample obtained by multi-step reaction. The origin of these peaks is unclear, but it may be associated with the orientation or ordering of interlayer organic cations.

The presence of n-butylammonium in the product was also confirmed by FT-IR spectrum (Figure 3.3), which displays CH_2 bending (1470, 1490 cm^{-1}) and C–H stretching (2930, 2960 cm^{-1}) modes. The broad peak at around 3000 cm^{-1}, corresponding to the NH_3^+ stretching mode, means that the interlayer organic molecules were intercalated as ammonium cations instead of neutral amines. In addition, IR absorption peaks at around 500 cm^{-1} could be assigned as Mn–O lattice vibrations as found in K_xMnO_2.[25] These results give strong evidence for the formation of an organic/MnO_2 layered hybrid with intercalated n-butylammonium cations.

SEM image of C4/MnO_2 shows a piled-up morphology consisting of plate-like particles (Figure 3.4a), which supports the formation of a layered product. These particles with a lateral dimension of micrometers are significantly larger than the sub-micron particles of m-C4/MnO_2 (Figure 3.4b). However, there are no distinct changes in the peak width of XRD (Figure 3.2). There is some degree of in-plane (in addition to interlayer) disorder; otherwise the apparent larger particle size of C4/MnO_2 can only be attribute to agglomerated microcrystallites, which seems unlikely. Consistent with the mismatch of XRD peak width and SEM particle size in C4/MnO_2 are the data for CTA/MnO_2,[20] which show sharper XRD peaks but smaller particle sizes.

The TG-DTA experiments for both C4/MnO_2 and m-C4/MnO_2 showed similar profiles Figure 3.5); The 3-step weight losses in TG were observed, the first one at around 120 °C, second one at around 120 - 250 °C, and third one at around 480 °C. The first weight loss was probably originated from the evaporation of surface adsorbed and interlayer water molecules, in consistency with the endothermic peaks in DTA. The second one was exothermic and attributed to the combustion of interlayer n-butylammonium cations. The last one is also exothermic and is due to the conversion to Mn_2O_3 as identified by the XRD experiments (Figure 3.6).

Since the reaction proceeded in alkaline conditions (95% yields), it can be assumed that H^+ or H_3O^+ does not exist in the interlayer and on the surface. Therefore, elemental analysis (C, H, N) of the product can determine *x* and *y* values in (*n*-butylammonium)$_x$$MnO_2 \cdot y H_2O$, and (C, 9.41%; H, 2.93%; N, 2.85%), leading to the composition of (*n*-butylammonium)$_{0.21}$$MnO_2 \cdot 0.3H_2O$, was obtained. No trace of Cl was detected from EDS. The valence of Mn ion estimated from the composition is +3.79, which is in good agreement with that of MnO_2 nanosheets obtained by one-pot method.[21] In comparison, the composition of m-C4/MnO_2 was found to be (*n*-butylammonium)$_{0.17}$$K_{0.04}$$MnO_2 \cdot 0.3H_2O$ (C, 7.67; H, 2.50; N, 2.24%) based on elemental analysis and EDS; generally, the multi-step reaction can not remove the interlayer alkali cations completely.[26] The author's one-pot method quickly and easily yields the alkali metal-free *n*-butylammonium/MnO_2 layered hybrid in almost the same composition as that of m-C4/MnO_2.

3.3.2 Nominal Ratio Dependence

For the product obtained for r = 2.00, the basal spacing of 4.65 Å (Figure 3.2a) as well as the FT-IR spectrum coincides with those of β-MnOOH (JCPDS 24-734; Figure 3.7). The broad absorption near 3000 cm^{-1}, three bands at 821, 955, and 1073 cm^{-1}, and two bands at 499 and 611 cm^{-1} correspond to hydrogen-bonded O–H stretch vibration, hydrogen-bonded O–H deformation vibration, and Mn–O vibration in β-MnOOH, respectively.[27] Of special note are the three hydrogen-bonded O-H deformation vibrations between 800 to 1000 cm^{-1}, which are characteristic for β-MnOOH, and distinguishable from other manganese oxides. The β-MnOOH is not ion-exchangeable with organic cations, making it an undesired product in this case. In contrast, at r = 2.25, additional multiple higher order reflections between 0 ° and 25 °, which correspond to an expanded d-spacing of 15.2 Å appeared (Figure 3.2b), and at $r \geq 2.5$, a single expanded phase was obtained (Figures 3.2c and 3.2d).

What product is formed strongly depends on r, which should correlates with pH. Thus the initial and final pH (or time dependence of pH) were examined. It is found that the initial pH is nearly unvaried with r (pH = 12.07 - 12.25). The nearly constant initial pH is understood, given pKa of 12.5 for *n*-butylamine and the studied r range ($2.0 \leq r \leq 4.0$). As soon as the two solutions were mixed, the pH dropped immediately and then decreased very slowly with time (see Table 2.1 and Figure 2.8). The sudden decrease in pH upon mixing (after 1 minute, pH = 7.98 for r = 2.0 and pH = 10.91 for r = 4.0) is due to the consumption of OH^- ions to form β-MnOOH. The formation of β-MnOOH might be followed by that of $Mn(OH)_2$ although the author could not confirm the presence of $Mn(OH)_2$ in the reaction mixture even when filtering the reaction at 1 min. It is known that $Mn(OH)_2$ is very sensitive to oxidation and H_2O_2 immediately oxidizes $Mn(II)(OH)_2$ into β-Mn(III)OOH.[28]

The gradual decrease in pH (Figure 3.8) is due to slow volatilization of n-butylamine and, for r = 4.0 the H^+ generation by the oxidation of β-MnOOH and the subsequent ion-exchange reaction of $H_xMnO_2 \cdot yH_2O$. The final pH is much lower for a smaller r (pH ~ 7.3 for r = 2.0 and pH ~10.6 for r = 4.0), influencing what product is actually formed. Considering the fact that basic conditions are

necessary for oxidation to form crystalline layered Mn^{4+}-contaning oxide,[29] β-MnOOH would not be further oxidized for a low *r*.

3.3.3 Reaction Time Dependence

The formation process of C4/MnO_2 was also examined by quenching the reaction mixture by filtration/drying at various reaction times. Figure 3.9 shows XRD patterns of products at different reaction times, starting after adding *n*-butylamine/H_2O_2 solution such that $r = 4.00$. Systematic changes of the structure were observed in these XRD patterns. Early in the reaction (< 5 min), the XRD patterns correspond to β-MnOOH with a basal spacing of 4.65 Å (black triangles). The first product obtained at 1 min has a broad diffraction pattern with low crystallinity and small particle size, but after 5 min peaks, especially intralayer reflections, become visible. Both formation and crystal growth of β-MnOOH proceeded simultaneously in the primary stage (< 5 min). The FT-IR spectrum also supports the formation of β-MnOOH (Figure 3.7).

Between 10 and 15 min, an additional broad peak with $d = 7.26$ Å, (opezcircles) and a widely expanded *d* spacing of 15.20 Å appeared (black circles). The *d* spacing of 7.26 Å corresponds to the interlayer spacing of hydrated layered manganese oxide, $H_xMnO_2 \cdot yH_2O$. Such interlayer hydration has been observed in numerous layered oxides (such as, Na_xCoO_2,[3] Na_xNiO_2[30] etc.) after oxidation, with reduced Coulombic interactions between interlayer cations and the negatively charged host layer. Both H_xMnO_2 and β-MnOOH have isostructural inorganic layers consisting of edge-sharing MnO_6 octahedra,[31] and therefore, $H_xMnO_2 \cdot yH_2O$ can be formed via topotactic oxidation of β-MnOOH. The peak intensities of hydrated H_xMnO_2 and β-MnOOH increased and decreased with reaction time, respectively, which means that β-MnOOH gradually converted into H_xMnO_2. Such a decrease of β-MnOOH fraction was also confirmed by the FT-IR spectra (Figure 3.7). A weak diffraction peak with *d* = 15.20 Å corresponds to C4/MnO_2 with a monolayer arrangement of *n*-butylammonium, as already mentioned.

After 30 min of reaction, the peak intensities of C4/MnO_2 increase, and 001 and multiple higher order reflections 002 to 004 appear. Thereafter, there were no distinct changes in the interlayer distances and no additional peaks. This indicates that phase-pure C4/MnO_2 was obtained within an hour. A further decrease in peak width from 30 to 45 min could be explained as an ordering of interlayer alkyl chains, or aging, which has been reported in many preparations of layered manganese oxides in alkaline solution.[32] From these results, the reaction mechanism of C4/MnO_2 can be understood as a process including 3 steps: (1) formation and crystal growth of β-MnOOH, (2) topotactic oxidation of β-Mn(III)OOH to form the protonated layered manganese oxide $H_xMn(III, IV)O_2 \cdot yH_2O$, and (3) quick ion-exchange of interlayer H^+ (or H_3O^+) with *n*-butylammonium and then formation of layered C4/MnO_2; Here, n-butylamine are dissolved mostly as n-butylammonium in H_2O due to their basicity (pKa =12.5), hence the interlayer H^+ ions are exchanged with n-butylammonium ions. This ion-exchange reaction can be facilitated by acid-base reaction (e.g., eliminated interlayer H^+ ions are trapped by OH^- ions in H_2O). All of the products are listed with reaction times in Table 3.1, and the reaction mechanism is schematically shown in Figure 3.10.

3.3.4 Further Application to Other Alkyl Ammonium/MnO_2 Systems

The author also investigated the effect of chain length in alkyl amines. When the shorter ethylamine was used instead of *n*-butylamine, a layered hybrid intercalated with the ethylammonium cations (C2/MnO_2) was obtained with the same conditions (r = 4.00, 24 hrs reaction) as for the synthesis of C4/MnO_2.

XRD analysis of the hybrid gave an interlayer spacing of 13.21 Å (Figure 3.11). This distance is 1.8 Å shorter than C4/MnO_2, and this is slightly greater than the interlayer distance deduced from alkyl chain length (1.2 Å/CH_2 group).[23] This discrepancy possibly stems from the difference in interlayer alkyl chain arrangement, that is, the decreased hydrophobic van der Waals forces between the interlayer alkyl chains in C2/MnO_2 causes randomization of the alkyl chain arrangement. The extinction of the peak

before the 110 reflection, and the broadened basal reflections of C2/MnO_2 could support the randomized arrangement of interlayer organic cations.

When the longer *n*-hexylamine was used, on the other hand, *β*-MnOOH resulted but not the intercalated product. The required alkaline conditions were not achieved due to the poor solubility of *n*-hexylamine in water above $r = 0.40$, and therefore, further oxidation of *β*-MnOOH did not proceed. Consequently, this one-pot method requires high solubility and basicity of the organic species.

3.4 Conclusions

The author firstly synthesized layered alkyl ammonium/MnO_2 hybrids by a one-pot oxidation reaction within a day and without any complex precursors. Unlike previous reports using redox-active organic species or complex Mn precursors, The author's one-pot approach only requires the organic species to be basic and water-soluble. Thus, the author's method is flexible since a range of organic species for intercalation can be added to the reaction mixture. The author have also investigated the formation mechanism of the author's one-pot reaction, and conclude that the following 3 steps are involved: (1) formation and crystal growth of *β*-Mn(III)OOH, (2) topotactic oxidation of *β*-MnOOH to form the protonated layered manganese oxide $H_xMnO_2 \cdot yH_2O$, and (3) ion-exchange of interlayer H^+ (or H_3O^+) with *n*-butylammonium and formation of layered C4/MnO_2. Furthermore, solubility of the alkyl amines is important to form the layered alkyl ammonium/MnO_2 hybrids, and an adequate excess of alkyl amine with respect to manganese ions is necessary.

In terms of expanding the scope of this reaction to other metals, the author suggests that the metal must form a layered metal hydroxide or oxyhydroxide, and be oxidized topotactically so that they are amenable to ion-exchange.

References

[1] Armstrong, A. R.; Bruce, P.G. *Nature*, **1996,** *381,* 499.

[2] Takada, K.; Sakurai, H.; Takayama-Muromachi, E.; Izumi, F.; Dilanian, R. A.; Sasaki, T. *Nature*, **2003**, *422,* 3523.

[3] (a) *Chemistry of Clays and Clay Minerals (Mineralogical Society Monograph No. 6*); Newman, A. C. D., Ed.; Longman Scientific & Technical: London, 1987. (b) Ogawa, M.; Kuroda, K. *Bull. Chem. Soc. Jpn.* **1997**, *70,* 2593.

[4] S. L. Suib, *Chem. Rev.* **1993**, *93,* 803.

[5] (a) Takagi, S.; Shimada, T.; Eguchi, M.; Yui, T.; Yoshida, H.; Tryk, D. A.; Inoue, H. *Langumuir* **2002**, *18*, 2265. (b) Takagi, S.; Eguchi, M.; Tryk, D. A.; Inoue, H. *J. Photochem. Photobiol. C* **2006**, *7*, 104. (c) Miyamoto, N.; Yamada, Y.; Koizumi, S.; Nakato, T. *Angew. Chem. Int. Ed.* **2007**, *46*, 4123. (d) Ogawa, M.; Kuroda, K. *Chem. Rev.* **1995**, *95*, 399.

[6] (a) Wang, Y-G.; Wu, W.; Cheng, L.; He, P.; Wang, C-X.; Xia, Y-Y. *Adv. Mater.* **2008**, *20*, 2166. (b) Sugimoto, W.; Iwata, H.; Yasunaga, Y.; Murakami, Y.; Takasu, Y. *Angew. Chem. Int. Ed.* **2003**, *42*, 4092.

[7] Choi, M.; Na, K.; Kim, J.; Sakamoto, Y.; Terasaki, O.; Ryoo, R. *Nature* **2009**, *461*, 246.

[8] (a) Izawa, H.; Kikkawa, S.; Koizumi, M. *J. Phys. Chem.* **1982**, *86,* 5023. (b) Rebbah, H.; Desgardin, G.; Raveau, B. *Mater. Res. Bull.* **1979**, *14*, 1125. (c) Nedjar, R.; Borel, M. M.; Raveau, B. *Mater. Res. Bull.* **1985, *20***, 1291. (d) Liu, Z-h.; Ooi, K.; Kanoh, H.; Tang, W-p.; Tomida, T. *Langmuir* **2000**, *16*, 4154.

[9] Feng, Q.; Kanoh, H.; Miyai, Y.; Ooi, K. *Chem. Mater.* **1995**, *7*, 1226.

[10] Wong, S. T.; Cheng, S. *Inorg. Chem.* **1992**, *32*, 1165.

[11] Ammundsen, B.; Paulsen, J. *Adv. Mater.* **2001**, *13,* 943.

[12] Feng, Q.; Kanoh, H.; Ooi, K. *J. Mater. Chem.* **1999**, *9*. 319.

[13] Burns, R. G.; Burns, V. M. *Manganese Dioxide Symposium*, Tokyo, 1980, Vol. 2, pp. 97-112.

[14] (a) Feng, Q.; Sun, E.; Yanagisawa, K.; Yamasaki, N. *J. Ceram. Soc. Jpn.* **1997**, *105*, 564. (b) Feng, Q.; Higashimoto, Y.; Kajiyoshi, K.; Yanagisawa, K. *J. Mater. Sci. Lett.* **2001**, *20*, 269. (c) Cai, J.; Liu, J.; Suib, S. L. *Chem. Mater.* **2002**, *14***,** 2071.

[15] (a) Luo, J.; Suib, S. L. *J. Phys. Chem. B* **1997**, *101*, 10403. (b) Ma, Y.; Luo, J.; Suib, S. L. *Chem. Mater.* **1999**, *11,* 1972.

[16] (a) Golf, P. L.; Baffier, N.; Bach, S.; Pereira-Ramos, J. P. *J. Mater. Chem*. **1994**, *4*, 133. (b) Ching, S.; Petrovay, D. J.; Jorgensen, M. L.; Suib, S. L. *Inorg. Chem*. **1997**, *36,* 883.

[17] (a) Morales, J.; Navas, J. J.; Tirado, J. L. *Solid State Ionics*, **1990**, *44,* 125. (b) Hirano, S.; Narita, R.; Naka, S. *Mater. Res. Bull.* **1984**, *19*, 1229.

[18] Luo, J.; Zhang, Q.; Suib, S. L. *Inorg. Chem.* **2000**, *39***,** 741.

[19] Chen, C-H.; Crisostomo, V. M. B.; Li, W-N.; Xu, L.; Suib, S. L. *J. Am. Chem. Soc.* **2008**, *130*, 14390.

[20] Kai, K.; Yoshida, Y.; Kageyama, H.; Saito, G.; Ishigaki, T.; Furukawa, Y.; Kawamata, J. *J. Am. Chem. Soc.* **2008**, *130*, 15983.

[21] Omomo, Y.; Sasaki, T.; Watanabe, M. *Solid State Ionics* **2002**, *151*, 243.

[22] Wortham, E.; Bonnet, B.; Jones, D. J.; Roziére, J.; Burns, G. R. *J. Mater. Chem.* **2004**, *14,* 121.

[23] Wang, L.; Takada, K.; Kajiyama, A.; Onoda, M.; Michiue, Y.; Zhang, L.; Watanabe, M.; Sasaki, T. *Chem. Mater.* **2003**, *15,* 4508.

[24] Buciuman, F.; Patcas, F.; Craciun, R.; Zahn, D. R. T. *Phys. Chem. Chem. Phys.* **1999,** *1*, 185.

[25] Omomo, Y.; Sasaki, T.; Wang, L.; Watanabe, M. *J. Am. Chem. Soc.* **2003**, *125*, 3568.

[26] Feng, X.; Tan, W.; Liu, F.; Fuang, Q.; Liu, X. *Science in China Ser. D* **2005**, *48*, 1438.

[27] *Advanded Inorganic Chemistry, 6th edn.*; Cotton, F. A.; Wilkinson, G.; Murillo, C. A.; Bochmann, M. Ed., John Wiley & Sons: New York, 1999.

[28] (a) Feng, Q.; Sun, E-H.; Yanagisawa, K.; Yamazaki, N. *J. Ceram. Soc. Jpn.* **1997**, *105,* 564. (b) Strobel, P.; Mouget, C. *Mater. Res. Bull.* **1993**, *28*, 93. (c) Portehault, D.; Cassaignon, S.; Baudrin, E.; Jolivet, J-P. *J. Mater. Chem.* **2009**, *19*, 2407. (d) Portehault, D.; Cassaignon, S.; Baudrin, E.; Jolivet, J-P. *J. Mater. Chem.* **2009**, *19*, 7947.

[29] Yang, X.; Takada, K.; Itose, M.; Ebina, Y.; Ma, R.; Fukuda, K.; Sasaki, T. *Chem. Mater.* **2008**, *20,* 479.

[30] Portehault, D.; Cassaignon, S.; Baudrin, E.; Jolivet, J-P. *Cryst. Growth Des*. **2010**, *10*, 2168.

[31] (a) Feng, Q.; Liu, L.; Yanagisawa, K. *J. Mater. Sci. Lett.* **2000**, *19*, 1567. (b) Brock, S. L.; Sanabria, M.; Suib, S. L.; Urban, V.; Thiyagarajan, P.; Potter, I. D. *J. Phys. Chem. B.* **1999,** *103,* 7416.

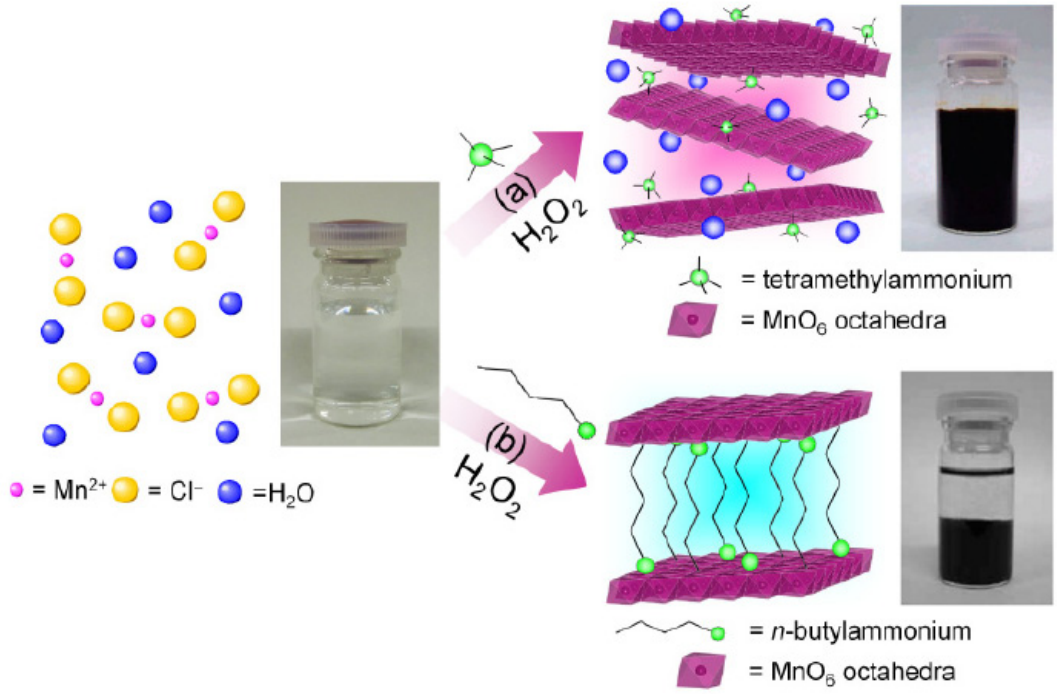

Figure 3.1. Schematic illustration of one-pot synthesis with sample photographs. (a) MnO_2 nanosheets,[21] and (b) organic/MnO_2 layered hybrid could be synthesized via choice of organic spiecies, which mixed with $MnCl_2$ aq. in the presence of an oxidizer, H_2O_2.

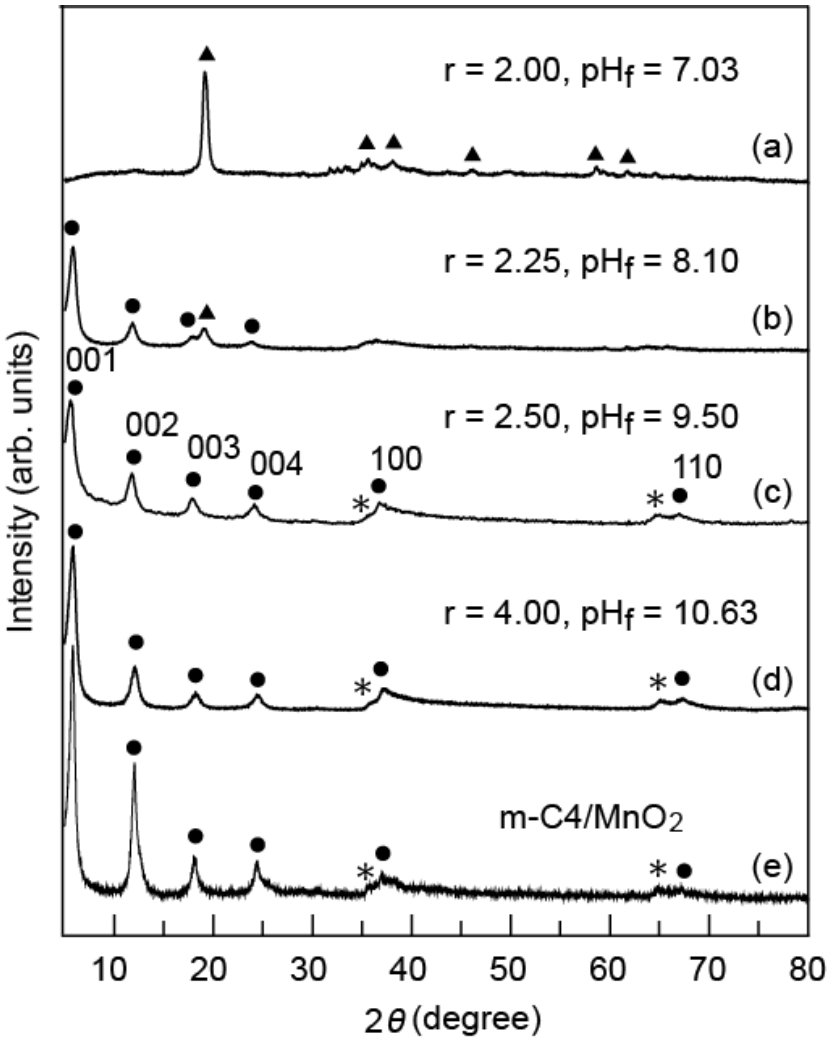

Figure 3.2. XRD patterns of products obtained by one-pot synthesis of $Mn(II)Cl_2$, H_2O_2, and *n*-butylamine for 24 hrs with (a) $r = 2.00$, (b) $r = 2.25$, (c) $r = 2.50$, and (d) $r = 4.00$, compared with the pattern of (e) m-C4/MnO_2 obtained by the multi-step reaction. (▲) β-MnOOH phase, (●) C4/MnO_2 phase, and (∗) unindexed peak. pH_f denotes the final pH of the solution.

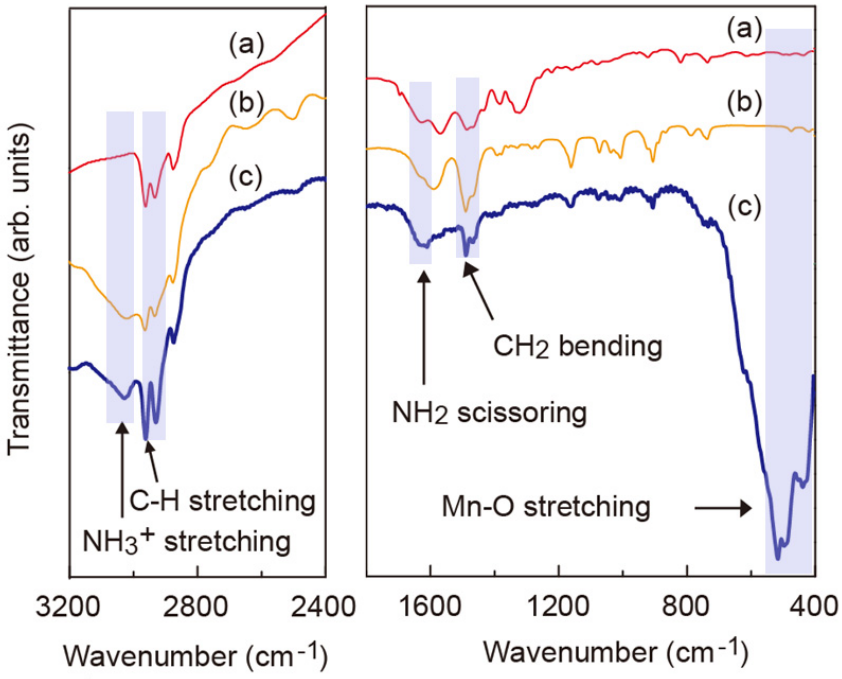

Figure 3.3. FT-IR spectra of (a) *n*-butylamine, (b) *n*-butylammonium chloride, and (c) C4/MnO_2 obtained by the one-pot method (r = 4.00) for 6 hrs. Arrows indicate the Mn–O lattice vibrational (ca. 500 cm^{-1}), NH_2 scissoring (1630 cm^{-1}), CH_2 bending (1470, 1490 cm^{-1}), C-H stretching (2930, 2960 cm^{-1}), and NH_3^+ stretching (3030 cm^{-1}) modes.

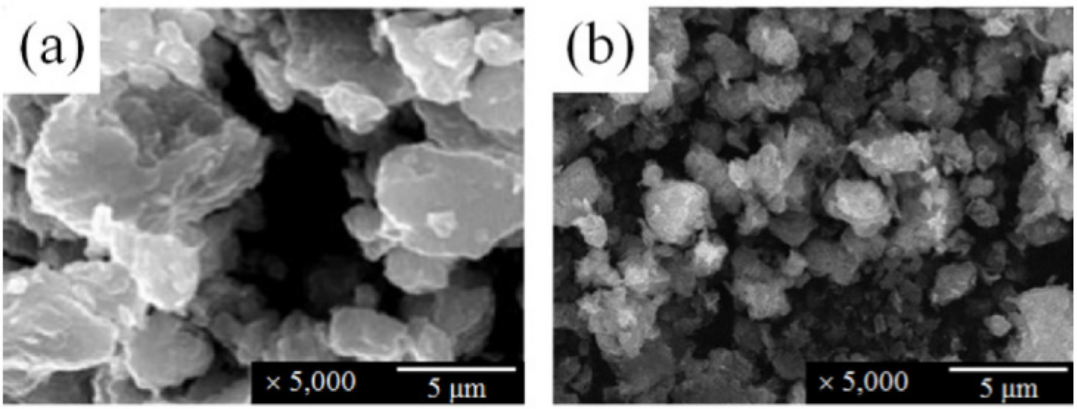

Figure 3.4. SEM images of C4/MnO_2 obtained by (a) the one-pot reaction (r = 4.00) and (b) the multi-step reaction.

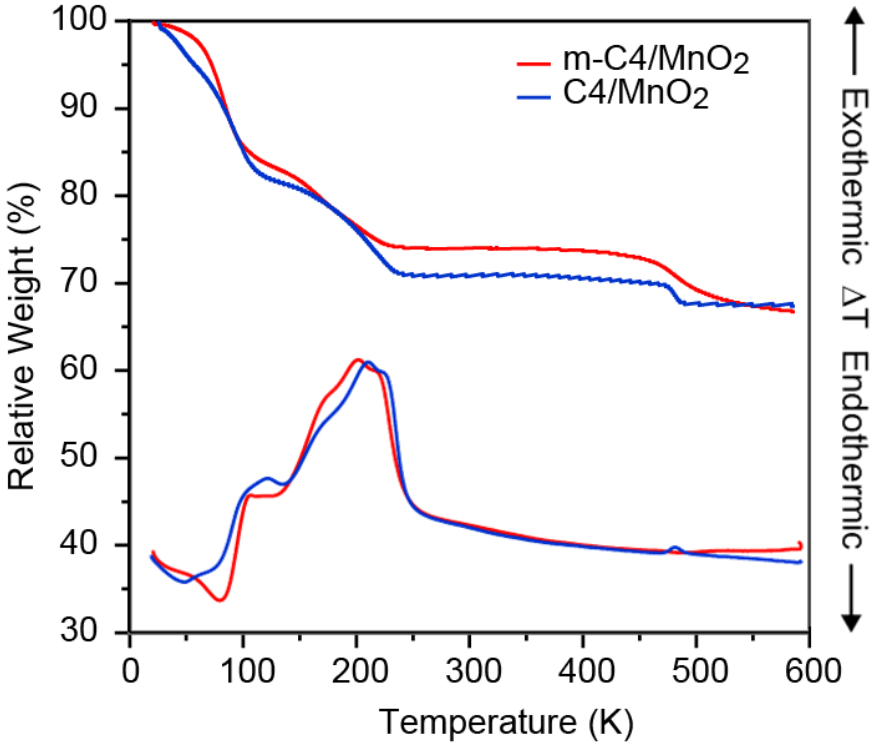

Figure 3.5. TG-DTA curves of C4/MnO_2 and m-C4/MnO_2. Based on the assumption that the first weight loss (17.6 % for C4/MnO_2 and 15.8 % for m-C4/MnO_2) and second weight loss (11.3 % C4/MnO_2 and 10.0 % m-C4/MnO_2) are due to the elimination of H_2O molecules and the combution of n-butylammonium cations respectively, the chemical formulas can be estimated as (n-butylammonium)$_{0.19}MnO_2 \cdot 1.2H_2O$ for C4/MnO_2 and (n-butylammonium)$_{0.16}MnO_2 \cdot 1.0H_2O$ for m-C4/MnO_2.

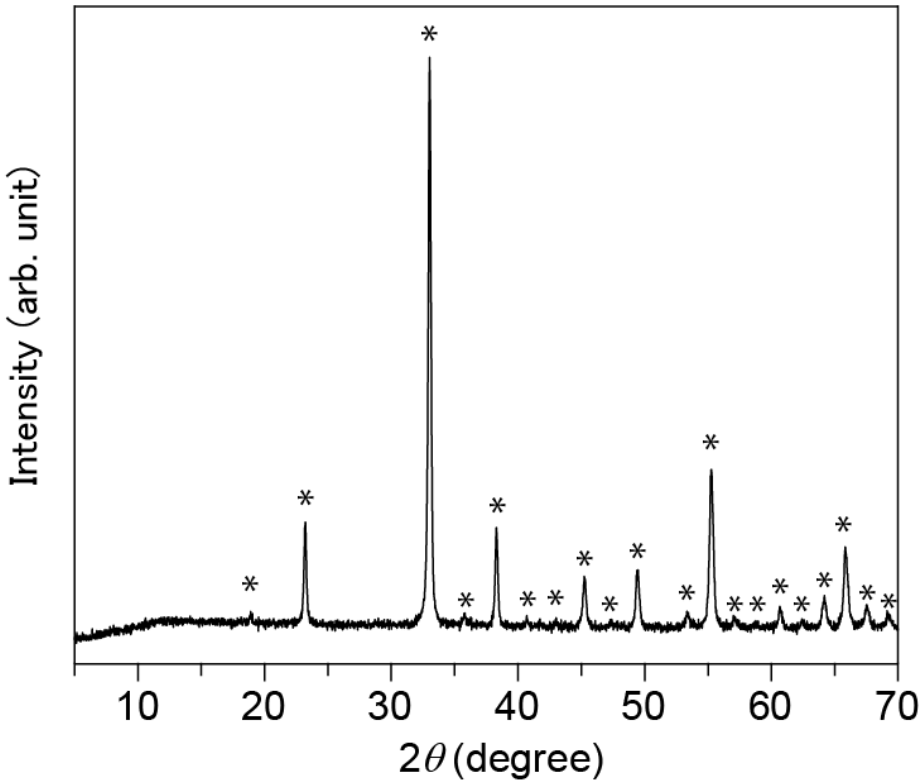

Figure 3.6. XRD pattern of the C4/MnO_2 after the TG-DTA measurement. All of the XRD peaks are identified as α-Mn_2O_3.

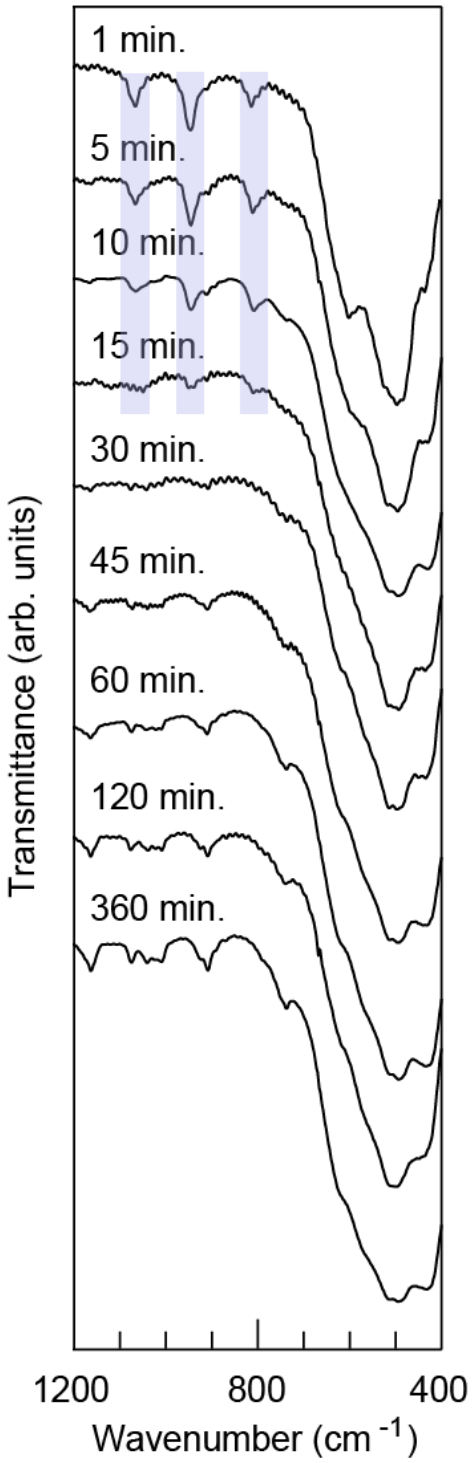

Figure 3.7. IR spectra of the products obtained by one-pot reaction with each reaction time. Three bands at 821, 955, and 1073 cm^{-1}, and two bands at 499 and 611 cm^{-1} corresponds to hydrogen-bonded O–H deformation vibration, and Mn–O vibration in β-MnOOH. For ≥ 30 minutes, the additional peaks between 800 to 1200 cm^{-1} correspond to interlayer *n*−butylammonium.

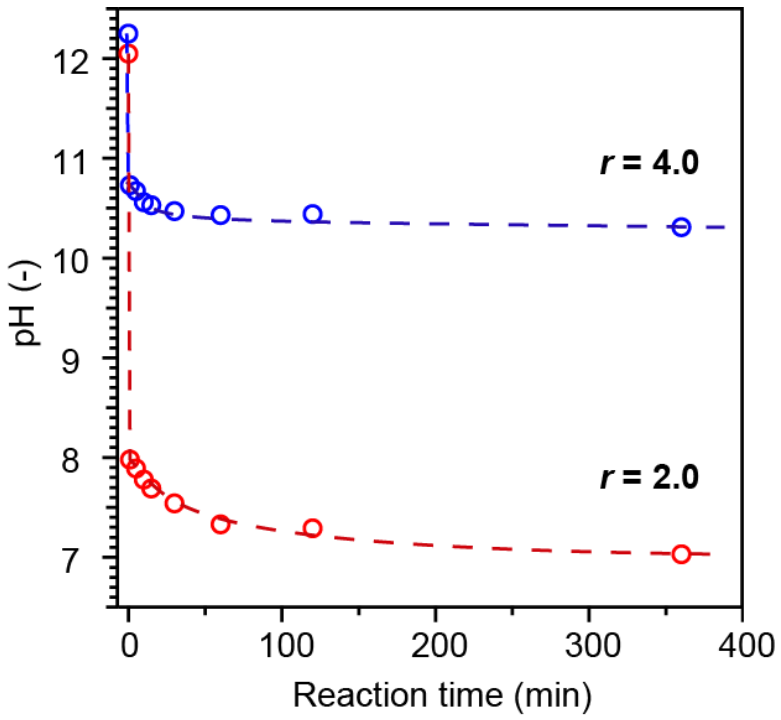

Figure 3.8. The variation of pH for $r = 4.0$ (blue) and $r = 2.0$ (red). Errors are within the markers.

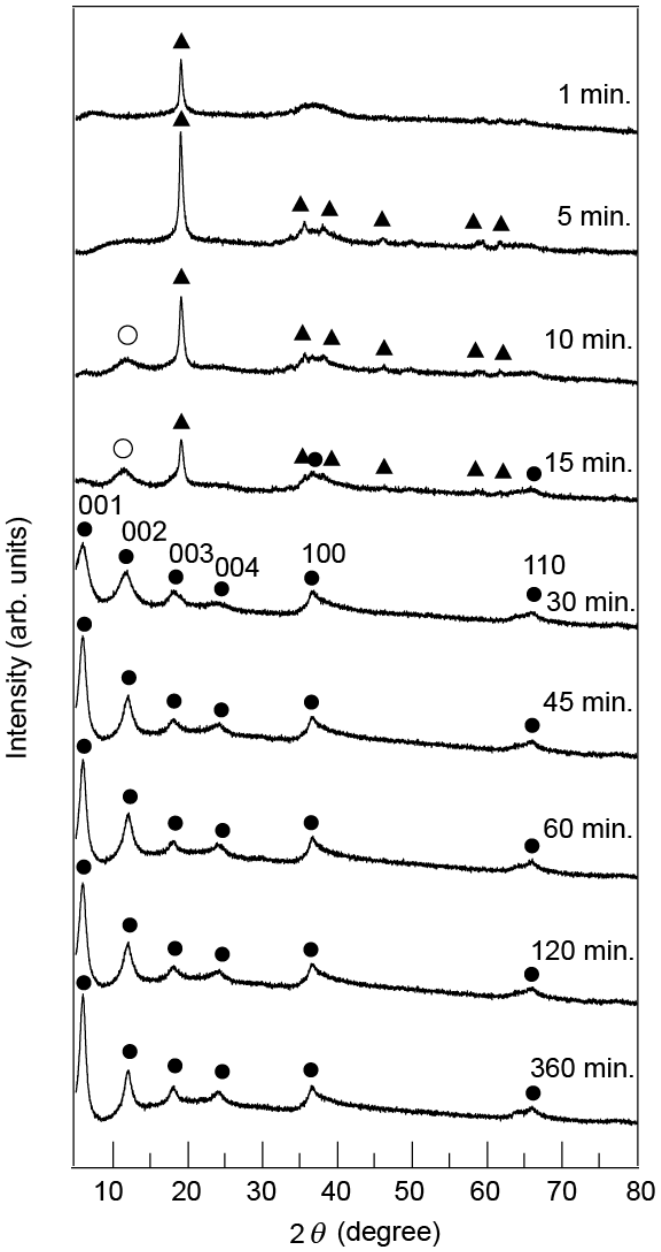

Figure 3.9. XRD patterns of the products obtained by the one-pot reaction (r = 4.00) at various reaction times: (▲) β-MnOOH phase, (○) $H_xMnO_2 \cdot yH_2O$ phase, and (●) C4/MnO_2 phase.

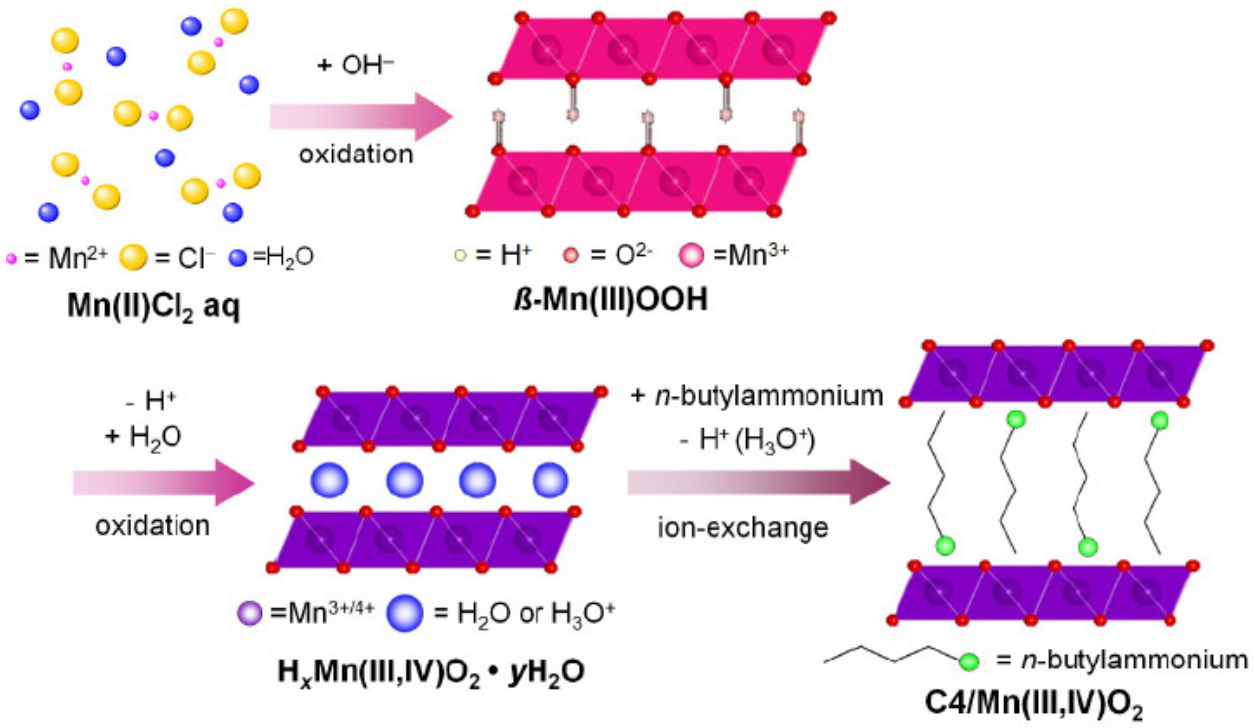

Figure 3.10. Schematic reaction steps of C4/MnO_2 in the one-pot reaction.

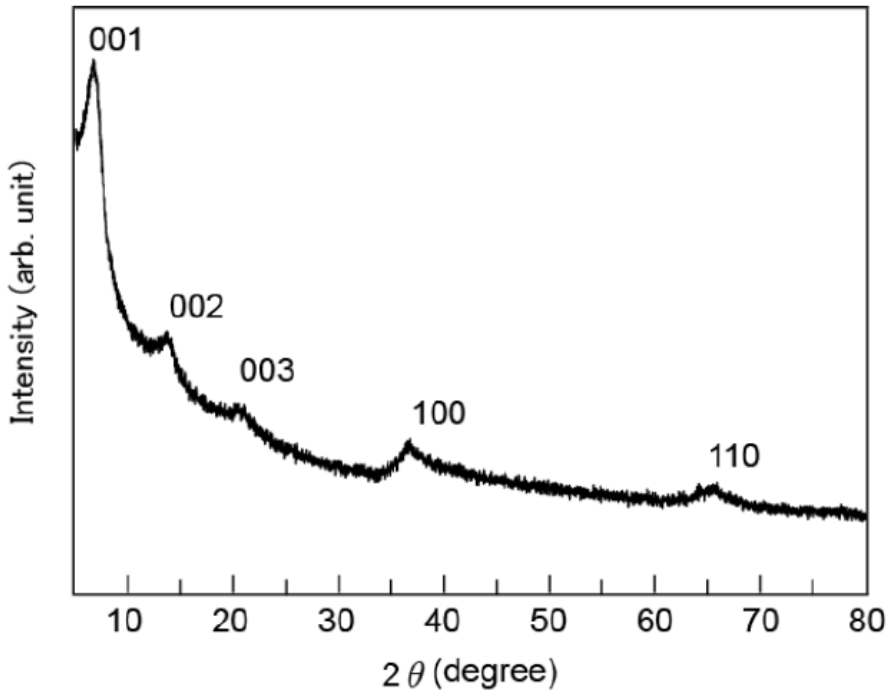

Figure 3.11. XRD pattern of C2/MnO_2 (r = 4.00).

Table 3.1. Interlayer distances and chemical species obtained at each reaction times (r = 4.00)

Reaction time (min)	Interlayer distance (Å)	Products
1	4.65	β-MnOOH
5	4.65	β-MnOOH
10	4.65, 7.26, 15.20	β-MnOOH, $H_xMnO_2 \cdot yH_2O$, C4/MnO_2
15	4.65, 7.26, 15.20	β-MnOOH, $H_xMnO_2 \cdot yH_2O$, C4/MnO_2
30	15.20	C4/MnO_2
45	15.20	C4/MnO_2
60	15.20	C4/MnO_2
120	15.20	C4/MnO_2
360	15.20	C4/MnO_2

Chaper 4:

Shape Deformable Nanocomposite Composed of Manganese Oxide Nanosheets

4.1 Introduction

Inorganic layered materials have been the recipient of a tremendous amount of interest due to a wide range of applications utilizing their unique two-dimensionally confined space.[1] A special fascination is that ionic organic guests can be intercalated to form functional organic/inorganic alternating layered hybrids when the interlayer space has ion-exchange ability.[2] The design and selection of the ionic organic guests not only impart the functionalities but also control the electrostatic interactions with the oppositely-charged inorganic hosts. The latter feature spurs the development of hybrid soft materials such as low-melting[3] and viscoelastic[4] solids, and hydrogel.[5] The shape deformability allows us to process the thin films or other desired forms and to use in restricted space.

Manganese oxides have become increasingly important as potential materials for many areas of electrochemical and catalytic applications.[6,7] In particular, a layered manganese oxide, birnessite, has

been promising candidates as cathodes in lithium ion batteries,[6,8] electrochemical capacitors[9] and catalysts,[10] and ion sieves,[11] due to their unique mixed valency and redox activity of the host, and tunable pore sizes. It is also noteworthy that the birnessite is the only manganese oxide that exfoliates into negatively-charged nanosheets[12,13] and accommodates the organic cations in the interlayer space.[12–15] So far, the colloidal suspension of the MnO_2^{x-} (x ~ 0.2) nanosheets has afforded several hybrid materials with different aggregation forms, such as bulk lamellar crystalline solids[11] and thin films fabricated by Langmuir-Blodgett (LB)[13] and layer-by-layer methods.[16] Here, a viscoelastic nanocomposite composed of the MnO_2^{x-} nanosheets are presented.

Although there have been a variety of viscoelastic clay nanocomposites[4] including hydrogels,[5] which are composed of clay mineral nanosheets such as hectorite and montmorillonite, they do not contain any transition metals, and thereby, limited properties associated with the catalysis, electrochemistry, and magnetism. In addition, most of them require lengthy processing involving *in-situ* polymerization, melt blending, and so on. Here, The author proposed the facile synthetic method for viscoelastic nanocomposites composed of MnO_2 nanosheets. the author's procedure was hinted at by foregoing works by Bourlinos *et al.*, who have synthesized several "ionic" liquids by combining cationic silyl-grafted metal oxide nanoparticles and long-chain sulfonate anions.[17] It is notable that this cation is comprised of (i) trimethoxysilyl group for immobilization on the MnO_2 nanosheet, (ii) two decyl groups for reducing inter-unit interactions, and (iii) quaternized ammonium group for charge compensation.

4.2. Experimental Section

A. Synthesis

In a typical synthesis, to 10 cm^3 of 0.1 M dark brown alkaline aqueous colloidal suspension of MnO_2^{x-} nanosheets synthesized by a facile room-temperature single-step reaction (Figure 4.1a),[13] was added 2 cm^3 of 0.69 M $[(CH_3O)_3Si(CH_2)_3N(CH_3)(C_{10}H_{21})_2]Cl$ methanol solution (40–42 wt%, Gelest). A black

spherical precipitate of *ca.* 8 mm in diameter was obtained after mixing with vigorous stirring for less than an hour at room temperature (Figure 4.1b). After being stirred overnight, the clayish solid was separated from the transparent supernatant, rinsed with copious amount of distilled water with being kneaded by mortar and pestle, and then dried *in vacuo* (dried nanocomposite; DNC).

B. Characterization

Powder XRD measurements were carried out with a MAC Science M18XHF diffractometer using Cu Kα radiation at a scanning rate of 0.01° s–1 in a 2θ range of 5–80°. EDS experiments were conducted with a JEOL JSM-5510LVN Scanning Electron Microscope operated at 20 kV. TG/DTA thermograms were taken on a Shimadzu DTG-60M instrument under nitrogen atmosphere (10 °C min^{-1} heating rate). FT-IR spectra were measured on KBr pellets or in dispersed KBr pellets with a Perkin-Elmer 1000 Series spectrophotometer. UV-Vis-NIR spectra were measured on quartz substrates or in dispersed KBr pellets using a Shimadzu UV-3100 spectrophotometer. Rheology measurements were conducted on a Thermo Scientific HAAKE MARS II rheometer at 25 °C. The moduli *G*' and *G*" were measured on frequency sweep from 10^2 and 10^{-3} Hz under a constant strain of 0.5%, and on strain sweep from 10^{-4} to 10% at a constant frequency of 1 Hz. Ionic conductivities were measured using a Wayne Kerr impedance analyzer 6440B over the frequency range between 20 Hz and 3 MHz. The nanocomposite was filled in a conductivity cell constructed with a pair of ITO glasses (surface resistance: 10 Ω/ cm^2) as electrodes and acetate films as a spacer (cell constant: 6.0×10^{-2} cm^{-1}), and the cell was placed in a temperature (25–70 °C) and humidity (50–95% RH) controlled chamber ESPEC SH-221.

4.3 Results and Discussions

The DNC gradually is brittle initially, and becomes viscoelastic after the air-exposure, and the resulting wet nanocomposite (WNC) can be easily deformed by applying an external stress, as seen in Figure 4.1c. Thin film mechanically coated on a quartz substrate has a thickness of less than 100 nm,

which was estimated assuming the linear relationship between the absorbance and the number of MnO_2 layers deposited by the LB method.[13] Since the weight gradually increases during the air-exposure and attains an 11% increase after a few days, the enhanced viscoelasticity is understood as a consequence of the adsorption of water molecules. The appearance of a broad band assigned to the O–H stretching vibration at around 3400 cm^{-1} supports the water adsorption (Figure 4.2). Differential thermal analysis (DTA) profile of WNC shows an endothermic peak at around 120 °C, arising from the dehydration of the adsorbed water molecules (Figure 4.3). The weight loss at the off-set temperature of the peak (*ca.* 10%) is in agreement with the increased weight of DNC during the air-exposure. On further heating, there is an exothermic peak assigned to the elimination of organic part at around 200 °C.

The electronic absorption spectrum of WNC exhibits a shoulder at around 380 nm (3.3 eV; Figure 4.4), which is ascribed to a d–d transition from 3d t_{2g} to 3d e_g levels of the Mn^{4+} ion in the MnO_2^{x-} nanosheets.[12,13] The estimated band gap (2.4 eV) is similar to that of colloidal suspension of MnO_2^{x-} nanosheets (*ca.* 2.5 eV). The presence of the ammonium cations was verified by the aliphatic C–H stretching vibration at 2800–3000 cm^{-1} (Figure 4.5). The presence of asymmetric Si–O–Si stretching vibration at 1112 cm^{-1} (polycyclic species) with a shoulder at *ca.* 1045 cm^{-1} (linear and branched species) is firm evidence of the formation of the cross-linked siloxane graft network (Figure 4.6).[18,19] The disappearance of C–O stretching vibration, which was observed for $[(CH_3O)_3Si(CH_2)_3N(CH_3)(C_{10}H_{21})_2]Cl$ at 1163 cm^{-1}, is indicative of the hydrolysis of methoxy groups followed by the graft polymerization. In relation, a weak signal at 913 cm^{-1}, assigned to the Si–OH group, indicates a relatively small amount of residual silanols and thus a high degree of cross-linking. Energy-dispersive X-ray spectroscopy (EDS) revealed that the nanocomposite has a Si/Mn ratio of nearly 1:1 and contains *ca.* 10% of Cl against Si (Figure 4.7). The Si/Mn ratio is in good agreement with the proposed surface-imprinted structure shown in Figure 4.6.

Powder X-ray diffraction (XRD) pattern of WNC revealed the formation of the lamellar structure with a basal spacing of 3.03 nm (Figure 4.8a). Given that the thickness of the MnO_2 layer is 0.52 nm,[12] a $(CH_2)_3SiO$ part (rigid length: *ca.* 1.2 nm) and a $C_{10}H_{21}N$ part (rigid length: *ca.* 1.7 nm) of the cation

would be slightly tilted from the *c* axis perpendicular to the MnO_2 layer. The crystallite size, calculated from the Scherrer equation, was 14.5 nm, which corresponds to an average of 4–5 alternating units of MnO_2 and organic layers (Figure 4.8b). Since the interlayer distance remains unchanged after the air-exposure, the adsorbed water molecules would be mainly intercalated in the space between the MnO_2 slabs (site B in Figure 4.8b) instead of the interlayer space in a slab (site A in Figure 4.8b).

Figure 4.9 shows the dynamic storage (*G*', elasticity) and shear-loss (*G*", viscosity) moduli of WNC on frequency (*f*) sweep with a strain amplitude of 0.5% at 25 °C. The ratio *G*"/*G*' (= loss tangent tanδ) of 0.14–0.67 is consistent with the viscoelastic behavior of WNC, as shown in Figure 4.1c. Interestingly, the dynamic viscosity (η^*) steadily decreases with increasing the frequency, which indicates the shear-thinning behavior. The yield stress, under which a phase transition from quasi-solid (*G*' > *G*") to quasi-liquid (*G*' < *G*") states occurs, is about 7×10^3 Pa (Figure 4.10).

Since a $N(CH_3)_2(C_{10}H_{21})_2$ cation with no trimethoxysilyl group, used in place of $(CH_3O)_3Si(CH_2)_3N(CH_3)(C_{10}H_{21})_2$ cation, gave a more brittle nanocomposite, the siloxane network as well as the adsorbed water molecules is indispensable for the viscoelastic character. It is possible that the coating of hydrophobic siloxane network on the MnO_2 nanosheet induces the viscoelastic character, relative to the reduced interactions between the MnO_2 slabs and water molecules. Moreover, the absence of a diffraction peak corresponding to the periodic arrangement of interlayer alkyl chains,[15] which was found for the brittle nanocomposites formed by use of $(CH_3O)_3Si(CH_2)_3N(CH_3)_2(C_nH_{2n+1})$ cations with a single longer alkyl group (n = 14, 18), strongly indicates the importance of the van der Waals interactions between the alkyl chains in determining the viscoelasticity.

As seen in Figure 4.11a and 4.11b, the ac conductivity (σ) steadily increases with increasing the relative humidity (RH), and the conductometric sensitivity to humidity is much higher than those of the reported MnO_2.[20] Since the ac conductivity of the dried nanocomposite is beyond the measurement limit (*ca.* 10^{-9} S cm^{-1}), the proton, which should be present in site B near the MnO_2 slabs due to the Lewis acidic nature of MnO_2^{x-}, must be responsible for the conductivity by the aid of water network. At 25 °C and 95% RH, a Debye relaxation process was observed at about 400 kHz and the proton conductivity is

1.9×10^{-5} S cm^{-1}. At 95% RH, temperature dependence of σ follows the Arrhenius equation $\sigma(T) = \sigma_0 \exp(-E_a/k_B T)$ with an activation energy (E_a) of 0.40 eV, and the σ value at 70 °C reaches as high as 1.3×10^{-4} S cm^{-1} (Figure 4.11c and 4.11d). These conducting features are comparable to those of $V_2O_5 \cdot 0.5H_2O$ xerogel with lamellar structure,[21] and the high E_a value indicates that the proton conduction in WNC is dominantly governed by the Grotthuss mechanism,[22] in which the protons transfer between the water molecules in the network to form H_3O^+. Experimental fact that the lower RH (50%), namely the gappy water network, leads to the higher E_a (0.73 eV) as well as the lower σ (5.5×10^{-7} S cm^{-1} at 25 °C) supports the Grotthuss-type proton migration.

4.4 Conclusions

In summary, the author successfully obtained the first viscoelastic nanocomposite composed of negatively-charged MnO_2 nanosheets, by a room-temperature one-pot processing. The nanocomposite can be easily deformed by applying an external stress; for example, mechanical stress gives a free-standing thin film with a thickness of less than 100 nm. It appears that (i) trimethoxysilyl group and (ii) double long alkyl groups (both for reducing inter-slab interactions) are indispensable for obtaining the viscoelastic nanocomposite in the present system. By the aid of (iii) quaternized ammonium group (for charge compensation), the present procedure would open up an exploration of new and more versatile viscoelastic nanocomposites composed of negatively-charged transition metal oxide nanosheets with a wide variety of metal elements, intralayer structures, and compositions. Specifically, facile fabrication of the shape-deformable nanocomposite with the redox activity would hold great promise for electrochemical devices and catalysts. Further detailed evaluation of the rheological properties, including the time-temperature superposition and linear viscoelasticity, will be the subject of future works.

References

[1] Auerbach, S. M.; Carrado, K. A.; Dutta, P. K.; Dekker, M. *Handbook of Layered Materials,* New York, 2004.

[2] (a) Gómez-Romerom, P.; Sanchez, C. *Functional Hybrid Materials*, Wiley-VCH, Germany, 2003. (b) Suib, S. L.; Chem. Rev. 1993, 93, 803. (c) Ogawa, M.; Kuroda, K. Chem. Rev. **1995**, *95*, 399. (d) Hoertz, P. G.; Mallouk, T. E. *Inorg. Chem.* **2005**, *44*, 6828.

[3] (a) Shimojima, A.; Sugahara, Y.; Kuroda, K. *Bull. Chem. Soc. Jpn.* **1997**, *70*, 2847. (b) Fujii, K.; Fujita, T.; Iyi, N.; Kodama, H.; Kitamura, K.; Yamagishi, A. *J. Mater. Sci. Lett.* **2003**, *22*, 1459. (c) Bourlinos, A. B.; Chowdhury, S. R.; Jiang, D. D.; An, Y-U.; Zhang, Q.; Archer, L. A.; Giannelis, E. P. *Small*, **2005**, *1*, 80.

[4] (a) Giannelis, E. P.; Krishnamoorti, R.; Manias, E. *Adv. Polym. Sci.* **1999**, *138*, 107. (b) Krishnamoorti, R.; Yurekli, K. *Curr. Opin. Colloid Interface Sci.* **2001**, *6*, 464.

[5] (a) Okada, A.; Usuki, A.; *Macromol. Mater. Eng.* **2006**, *291*, 1449. (b) Haraguchi, K.; *Curr. Opin. Solid State Mater. Sci.* **2007**, *11*, 47. (c) Wang, Q.; Mynar, J. L.; Yoshida, M.; Lee, E.; Lee, M.; Okuro, K.; Kinbara, K.; Aida, T. *Nature,* **2010**, *463*, 339.

[6] (a) Armstrong, A. R.; Bruce, P. G. *Nature*, **1996**, *381*, 499. (b) Thackeray, M. M.; Johnson, C. S.; Vaughey, J. T.; Li, N.; Hackney, S. A. *J. Mater. Chem.* **2005**, *15*, 2257.

[7] (a) Shen, Y. F.; Zerger, R. P.; DeGuzman, R. N.; Suib, S. L.; McCurdy, L.; Potter, D. I.; O'Young, C. L. *Science,* **1993,** *260,* 511. (b) Cao, H.; Suib, S. L. *J. Am. Chem. Soc.* **1994**, *116*, 5334.

[8] (a) Wang, L.; Takada, K.; Kajiyama, A.; Onoda, M.; Michiue, Y.; Zhang, L.; Watanabe, M.; Sasaki, T. *Chem. Mater.* **2003**, *15*, 4508. (b) Wang, Y. –G.; Wu, W.; Cheng, L.; Wang, C. –X.; Xia, Y. –Y. *Adv. Mater.* **2008**, *20*, 2166.

[9] (a) Brousse, T.; Toupin, M.; Dugas, R.; Athouël, L.; Crosnier, O.; Bélanger, D. *J. Electrochem. Soc.* **2006**, *153*, A2171. (b) Devaraj, S.; Munichandraiah, N. *J. Phys. Chem. C,* **2008**, *112*, 4406.

[10] (a) Lvov, Y.; Munge, B.; Giraldo, O.; Ichinose, I.; Suib, S. L.; Rusling, J. F. *Langmuir*, **2000**, *16*, 8850. (b) Espinal, L.; Suib, S. L.; Rusling, J. F. *J. Am. Chem. Soc.* **2004**, *126*, 7676.

[11] (a) Feng, Q.; Kanoh, H.; Ooi, K. *J. Mater. Chem.* **1999**, *9*, 319. (b) Suib, S. L. *J. Mater. Chem.* **2008**, *18*, 1623.

[12] (a) Liu, Z.-h.; Ooi, K.; Kanoh, H.; Tang, W.-p.; Tomida, T. *Langmuir,* **2000**, *16*, 4154. (b) Omomo, Y.; Sasaki, T.; Wang, L.; Watanabe, M. *J. Am. Chem. Soc.* **2003**, *125*, 3568. (c) Liu, Z.; Ma, R.; Ebina, Y.; Sasaki, T. *Chem. Mater.* **2007**, *19*, 6504.

[13] Kai, K.; Yoshida, Y.; Kageyama, H.; Saito, G.; Ishigaki, T.; Furukawa Y.; Kawamata, J. *J. Am. Chem. Soc.* **2008**, *130,* 15938.

[14] (a) Paterson, E. *Am. Mineral.* **1981**, *66*, 424. (b) Wong, S. –T.; Cheng, S. *Inorg. Chem.* **1992**, *31*, 1165. (b) Ammundsen, B.; Wortham, E.; Jones, D. J.; Roziere, J. R. *Mol. Cryst. Liq. Cryst.* **1998**, *311*, 327. (c) Liu, Z.-h.; Ooi, K.; Kanoh, H.; Tang, W.; Yang, X.; Tomida, T. *Chem. Mater.* **2001**, *13*, 473. (d) Omomo, Y.; Sasaki, T.; Watanabe, M. *Solid State Ionics,* **2002**, *151*, 243. (e) Wang, L.; Ebina, Y.; Takada, K.; Kurashima, K.; Sasaki, T. *Adv. Mater.* **2004**, *16*, 1412. (f) Chen, C-H.; Crisostomo, V. M. B.; Li, W-N.; Xu, L.; Suib, S. L. *J. Am. Chem. Soc.* **2008**, *130*, 14390.

[15] Wortham, E.; Bonnet, B.; Jones, D. J.; Rozière, J.; Burns, G. R. *J. Mater. Chem.* **2004**, *14*, 121.

[16] (a) Wang, L.; Sakai, N.; Ebina, Y.; Takada, K.; Sasaki, T. *Chem. Mater.* **2005**, *17*, 1352. (b) Sakai, N.; Ebina, Y.; Takada, K.; Sasaki, T. *J. Electrochem. Soc.* **2005**, *152*, E384. (c) Sakai, N.; Ebina, Y.; Takada, K.; Sasaki, T. *J. Phys. Chem. B*, **2005**, *109*, 9651.

[17] (a) Bourlinos, A. B.; Herrera, R.; Chalkias, N.; Jiang, D. D.; Zhang, Q.; Archer, L. A.; Giannelis, E. P. *Adv. Mater.* **2005**, *17,* 234. (b) Bourlinos, A. B.; Chowdhury, S. R.; Herrera, R.; Jiang, D. D.;

Zhang, Q.; Archer, L. A.; Giannelis, E. P. *Adv. Funct. Mater.* **2005**, *15,* 1285. (c) Bourlinos, A. B.; Stassinopoulos, A.; Anglos, D.; Herrera, R.; Anastasiadis, S. H.; Petridis, D.; Giannelis, E. P. *Small,* **2006**, *2*, 513.

[18] (a) Dong, H.; Brennan, J. D. *Chem. Mater.* **2006**, *18,* 4176. (b) Smith, A. L.; Anderson, D. R. *Appl. Spectrosc.* **1984**, *38*, 822.

[19] The siloxane graft network could be formed on both sides of MnO_2 layers. According to the EDS data (Si/Mn ratio ~ 1), the domain of the network, which was formed on each side of the layers, would be interpenetrated in each interlayer space.

[20] (a) Xu, C.; Miyazaki, K.; Watanabe, T. *Sens. Actuators B*, **1998**, *46*, 87. (b) Doescher, M. S.; Pietron, J. J.; Dening, B. M.; Long, J. W.; Rhodes, C. P.; Edmondson, C. A.; Rolison, D. R. *Anal. Chem.* **2005**, *77*, 7924.

[21] (a) Barboux, P.; Baffier, N.; Morineau, R.; Livage, J. *Solid State Ionics*, **1983**, *9-10*, 1073. (b) Livage, J. *Chem. Mater.* **1991**, *3*, 578.

[22] Agmon, N. *Chem. Phys. Lett.* **1995**, *244*, 456.

[23]

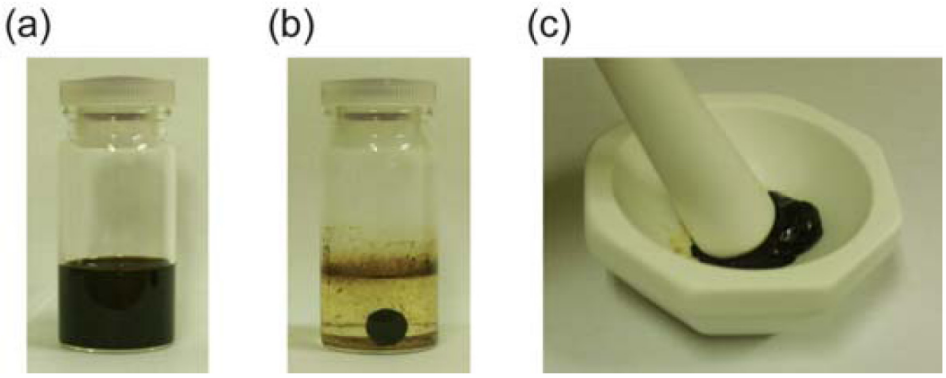

Figure 4.1. Photographs of (a) 0.1 M colloidal suspension of MnO_2 nanosheets, (b) black spherical precipitate after adding $[(CH_3O)_3Si(CH_2)_3N(CH_3)(C_{10}H_{21})_2]Cl$ methanol solution and stirring overnight at room temperature, and (c) shape deformation of WNC.

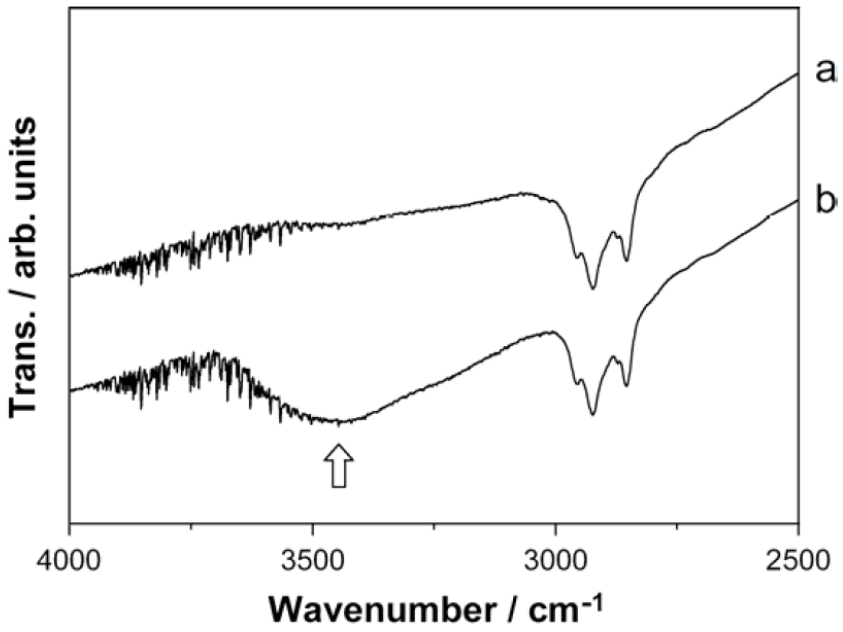

Figure 4.2. Infrared spectra of (a) DNC and (b) WNC coated on a KBr pellet. An arrow indicates the O–H stretching vibration of adsorbed water molecules.

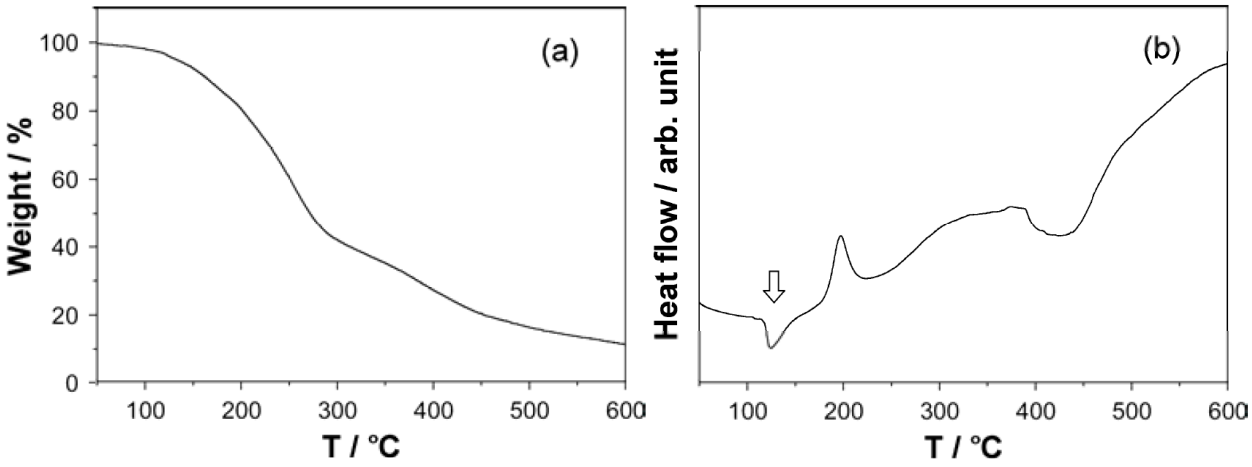

Figure 4.3. (a) TG and (b) DTA thermograms of WNC on heating process. An arrow indicates an endothermic peak, associated with the dehydration of the adsorbed water molecules.

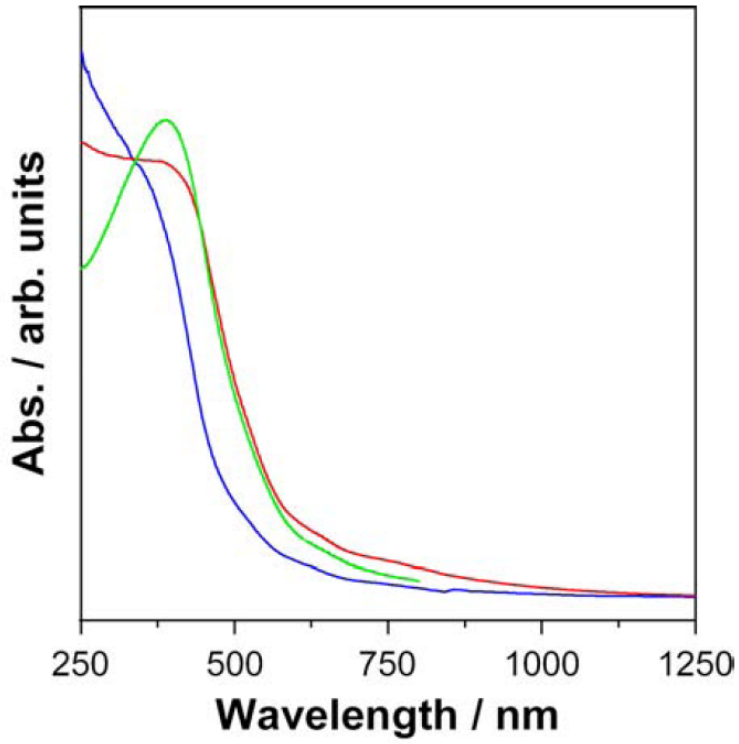

Figure 4.4. UV-Vis spectra of WNC mechanically coated on a quartz substrate (red line), WNC dispersed in a dispersed KBr pellet (blue line), and 10^{-4} M colloidal suspension of MnO_2 nanosheets (green line).

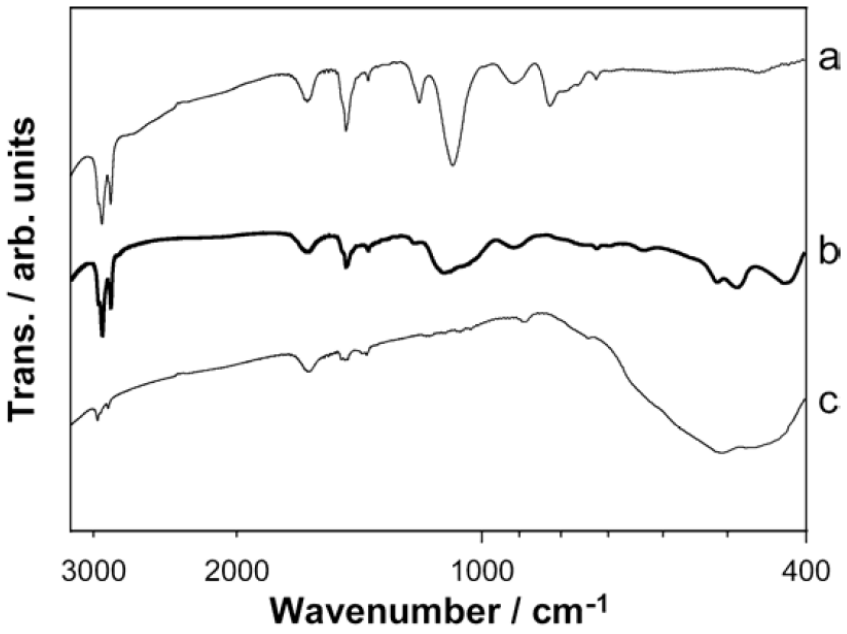

Figure 4.5. Infrared spectra of (a) $[(CH_3O)_3Si(CH_2)_3N(CH_3)(C_{10}H_{21})_2]Cl$, (b) WNC, and (c) tetrabutylammonium/MnO_2, dispersed in compressed KBr pellets.

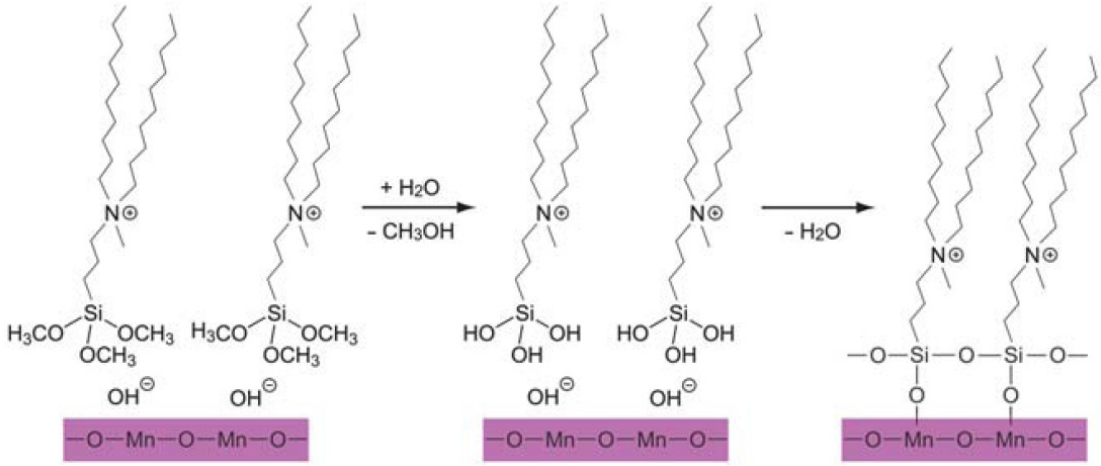

Figure 4.6. Proposed pathway of the formation of the present nanocomposite. The first step is the hydrolysis reaction of methoxy groups, and the second step is the graft polymerization reaction in alkaline condition to form the siloxane network imprinted on the MnO_2 nanosheet.

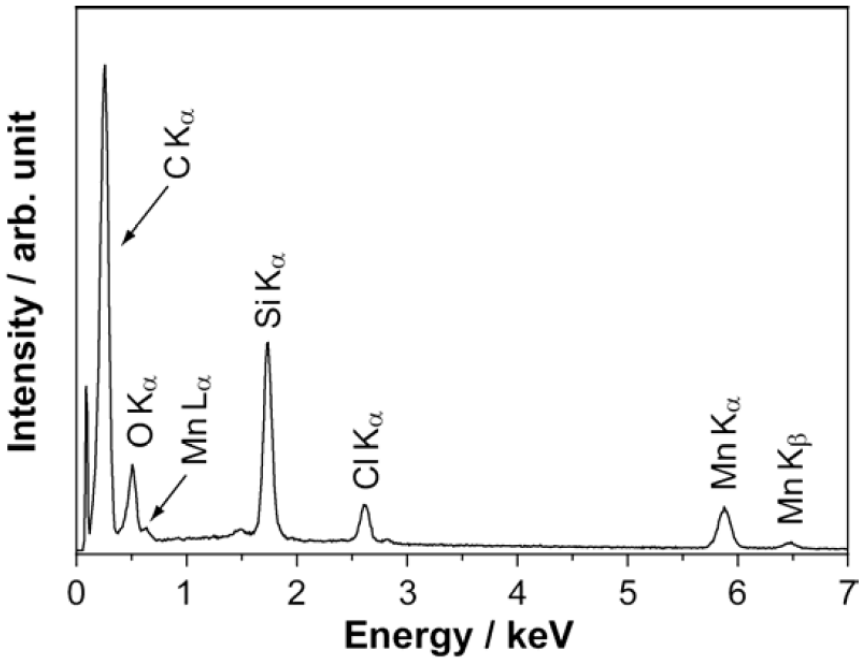

Figure 4.7. EDS spectrum of DNC.

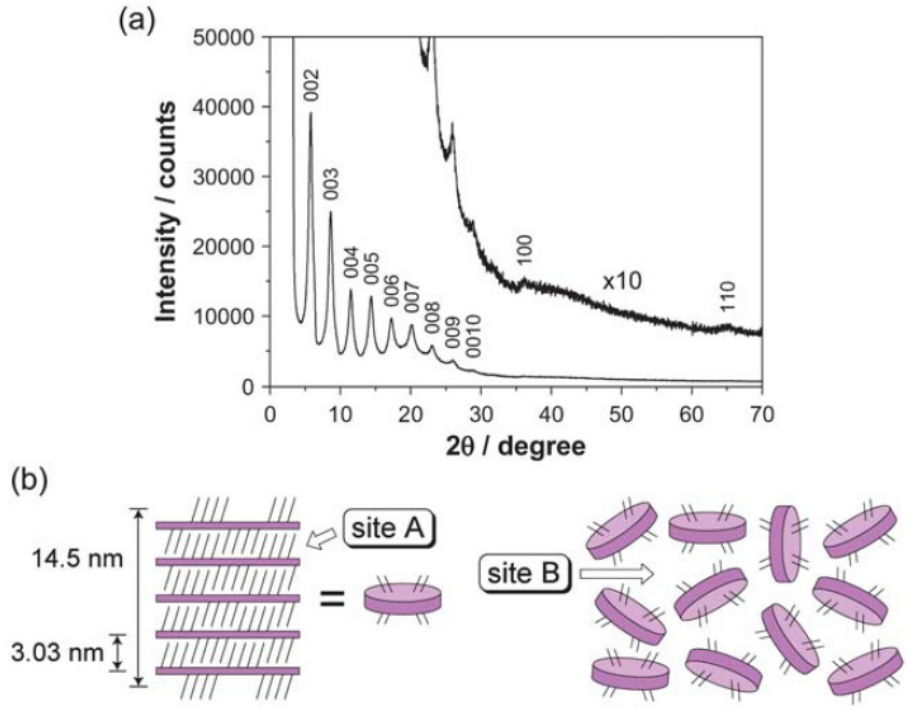

Figure 4.8. (a) Powder XRD pattern of WNC at room temperature. (b) Schematic models of aMnO2 slab (left) and the nanocomposite structure (right).

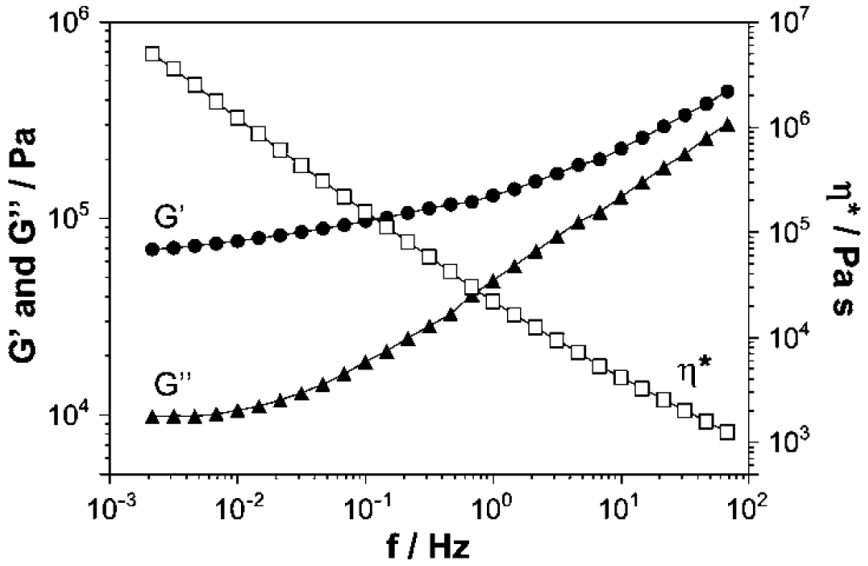

Figure 4.9. Frequency dependence of dynamic storage (G', closed circles) and shear-loss (G", closed triangles) moduli, and dynamic viscosity (η^*, open squares) of WNC with a strain amplitude of 0.5% at 25 °C.

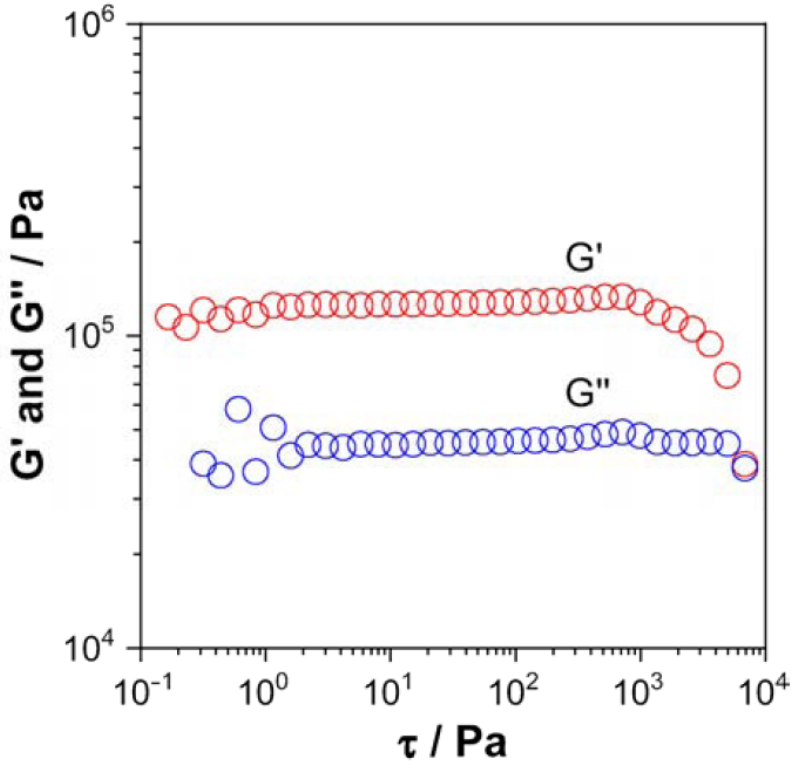

Figure 4.10. Stress dependences of dynamic storage (*G*', red circles) and shear-loss (*G*", blue circles) moduli of WNC at a constant frequency of 1 Hz at 25 °C.

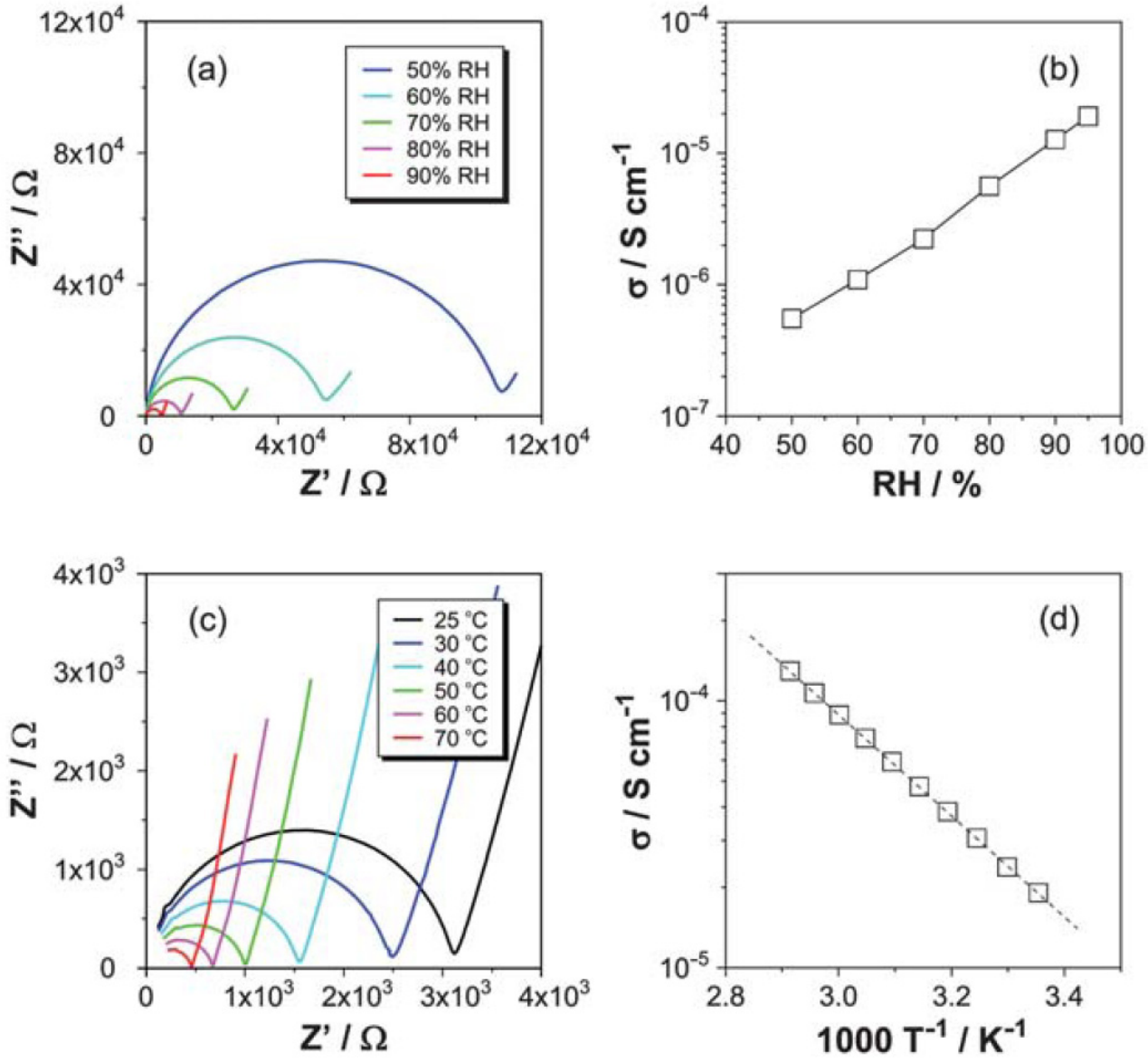

Figure 4.11. Humidity dependence of (a) impedance Nyquist plot and (b) proton conductivity at 25 °C, and temperature dependence of (c) impedance Nyquist plot and (d) proton conductivity at 95% RH. In (d), a dotted line represents the calculated conductivity for the Arrhenius law with Ea . 0.40 eV.

Chaper 5:

Electrochemical Characterization of Single-Layer MnO_2 Nanosheets as a High-Capacitance Pseudocapacitor Electrode

5.1 Introduction

In recent years, the development of rechargeable high power energy storage devices has attracted intense research interest due to growing demand for power systems such as acceleration units in electric vehicles or backup systems or emergency power supplies in mass transport systems, etc.[1] Among various methods of energy storage, supercapacitors or pseudocapacitors are possible candidates for these high power energy storage systems.[2] In particular, puseudocapacitors with organic electrolytes show high power and high energy density due to utilization of both surface ion adsorption and redox reactions, together with wider potential windows due to the electrochemical stability of the organic electrolytes.[2a,3,4] Such pseudocapacitors are charge-storage devices characterized by intermediate electrochemical properties between batteries and conventional capacitors.[2a,3]

Various conductive polymers or metal oxides have been investigated as pseudocapacitor electrodes. Regarding conducting polymers, polythiophene and polyacetylene have been investigated intensely. However, their cycle life is poor.[5] Among metal oxides, RuO_2 shows a high specific capacity of about 760 F g^{-1} with excellent cyclability,[6] although ruthenium is very expensive and toxic. Vanadium oxides,[7] iron oxides,[8] nickel oxides,[9] and manganese oxides[10] have also been investigated. In particular, manganese oxides are promising because of their low cost,[11] high electrochemical activity,[12c] and environmentally friendly nature.[11]

To improve the properties as a pseudocapacitor electrode, morphological control of active materials to increase the electrochemically active surface area and/or the construction of nanocomposites with several current collectors (such as carbon or metal foams) have been examined to enhance charge transport to the active materials.[13] Thus, nanostructured metal oxides (e.g., thin platelets of K_xMnO_2, $Co(OH)_2$ nanorods, etc.),[14] or composite materials with a current collectors (e.g., $Ni(OH)_2$/Ni foam, K_xMnO_2/carbon fiber, and K_xMnO_2/graphene, etc.) have been examined as pseudocapacitor electrodes.[13a,15]

Recently, ultrathin films (~ 1 nm in thickness) consisting of exfoliated layered inorganic compounds, termed as "nanosheets", have been obtained via exfoliation of layered inorganic compounds (e.g., $RbCa_2Nb_3O_{10}$, K_xMnO_2, $Al_{1/3}Mg_{2/3}(OH)_2 \cdot 1/3NO_3$, etc.).[16] One of the important features of these nanosheets is their considerably large specific surface area.[16b,16c] Therefore, a highly efficient pseudocapacitor electrode can be developed by utilizing these surfaces for charge storage. Several approaches to highly efficient electrode materials have been examined by using multilayered nanosheet assemblies (e.g., restacked RuO_2 nanosheets, MnO_2/carbon nanotubes, $Ni_{1/3}Mg_{2/3}(OH)_2$/graphene, etc.).[17] Kadoma *et al*. examined a composite electrode comprised of MnO_2 nanosheets and acetylene black (AB), showing its galvanostatic charge/discharge characteristics and the surface structure.[19] This composite electrode utilizes the nanosheet surface more effectively than bulk materials. However, in the past, MnO_2 nanosheets have been typically synthesized via exfoliation of layered parent compound, and such nanosheets always contain a portion of nonexfoliated or restacked materials (~ 50 %).[17a] In Ref.

[19], the composite electrode was prepared by adding AB powder to colloidal suspension of MnO_2 nanosheets and subsequent drying. This process inevitably yields a large amount of unexfoliated materials and excess alkali (e.g. ternary-alkylammonium hydroxide used for exfoliation). Therefore, in order to efficiently use these nanosheets as charge storage electrodes, removing such unexfoliated materials and excess alkali is desirable.

To solve these problems, in this study the author conducted an alternative synthetic procedure of the nanosheets, direct synthesis of the single-layer nanosheets (monosheets) via a one-pot solution procedure.[20] This method can obtain MnO_2 monosheets without any purification (e.g. centrifugation), because the reaction procedure does not includes any exfoliation step. In this capter, the author prepared the MnO_2 monosheets by the one-pot process, and then prepared the MnO_2/AB composite via electrostatic adsorption of MnO_2 monosheets on AB surfaces. This composite structure is sustained by electrostatic interactions; thus the excess alkalis and Cl^- ions included in starting materials can be removed by washing. Structural analysis and several electrochemical properties (galvanostatic discharge capacity, specific capacitance, cyclability, and rate performance) of the obtained MnO_2/AB composite were investigated. This MnO_2/AB showed considerable high specific capacitance exceeding the theoretical maximum value of manganese oxide capacitor and high galvanostatic capacity exceeding that of the previously examined MnO_2 composites.

5.2. Experimental Section

A. Synthesis and Sample Preparation

Single layer MnO_2 nanosheets were synthesized through a one-pot procedure.[20a] In this preparation, 40 mL of mixed aqueous solution prepared from 12 mL of 1.0 M tetramethylammonium hydroxide (TMA·OH), 2 mL of 30 wt% H_2O_2 and 16 mL of distilled water were poured into $MnCl_2$ aq (0.3 M, 20 mL) with stirring, and kept stirring for 12 hrs at 25 °C. The composite formulation procedure referred

the Kadoma's method[19]; the obtained reddish-brown MnO_2 suspension was diluted by 140 mL distilled water, and 5 g of acetylene black (STREM CHEMICALS) were added into the suspension to give 10 wt % of MnO_2 in composite, and then stirred for 12 hrs. After stirring, the supernatant became colorless, which indicates the completion of adsorption of MnO_2 nanosheets onto the AB. The obtained MnO_2/AB composite was filtered, washed with distilled water until the filtrate become neutral, and then vacuum-dried at 100 °C for 2 days.

B. Characterization

Powder X-ray diffraction (XRD) measurements were carried out with a Bruker D8 diffractometer using Cu Kα radiation at a scanning rate of 0.01 ° s^{-1} in a 2θ range of 5–80 °. Powder samples were mounted on glass slides. Scanning electron microscopy (SEM) experiments were conducted with a JEOL JSM-5510LVN instrument operating at 20 kV. Samples were mounted on a carbon tape. Transmission electron microscopy (TEM) was performed using Hitachi H9000NAR operating at 100 kV. Samples were dispersed in methanol, and deposited on a cupper grid.

C. Electrochemical Measurements

The electrochemical measurements were carried out with a three-electrode-type cell in an Ar-filled glovebox at room temperature. The MnO_2/AB composite electrode for this measurement was composed of 90 wt% MnO_2/AB composite and 10 wt % poly(tetrafluoroethylene) (PTFE). Lithium foil was used as counter and reference electrodes, with current collectors of aluminum foil. The electrolyte used was 1 mol dm^{-3} $LiClO_4$ in 1:1 (v/v) ethylene carbonate (EC)/dimethyl carbonate (DMC) solution. Charge-discharge properties are examined galvanostatically at 10 μAcm^{-2} in an Ar-filled glovebox at room temperature. The cutoff potentials were set at 2.0 and 4.3 V (vs Li/Li^+). Cyclic voltammetry (CV) experiments were performed from 2.0 to 4.0 V (vs Li/Li^+) at a scan rate of 1 mV s^{-1} to 200 mV s^{-1}. The specific capacitance C (F g^{-1}) was calculated by integrating the CV curve to obtain the voltammetric

charge (Q_{total}). The voltammetric charge related to the presence of AB in the composite electrode was subtracted from the value of Q_{total} to obtain the charge only related to MnO_2 nanosheets (Q). Finally, Q was divided by the mass of the composite electrode (m) considering the amount of active material (MnO_2) in the electrode (9 wt%) and the width of the potential window (ΔV), which gives $C = Q/(m \cdot \Delta V)$. Before electrochemical measurements, 1 CV cycle was conducted to remove the residual TMA^+ ions on the MnO_2 surfaces.

5.3 Results and Discussions

5.3.1 Structural characterization of MnO_2/AB composite

The XRD pattern of the MnO_2/AB composite is shown in Figure 5.1, in comparison with TMA/MnO_2 obtained by simply drying the MnO_2 suspension without AB.[20a] The TMA/MnO_2 sample shows interlayer reflections at 9.2°, 18.4° and 27.7°, and asymmetric in-plane reflections at 36.6° and 66.7°, implying a turbostratic layered structure, which can be indexed with a hexagonal cell of c = 9.65 Å and a = 2.86 Å.[20a]. The MnO_2/AB composite exhibits no interlayer reflections (*i.e.* 00*l*), except for only two asymmetric peaks. The peak positions of in-plane 100 and 110 reflections agree with those of TMA/MnO_2. Considering that the multilayered nanosheets thin films start to show the interlayer reflections when the stacking number grows to three or more,[21] it is inferred that the MnO_2 nanosheets are deposited onto the AB surface with making less stacking formation, at most bilayer forms. The author examined the absorption character by varying the MnO_2/AB ratio, and found that the adsorption amount is at maximum 23 wt%, which suggests that the adsorption is purely electrostatic between the MnO_2 sheets and AB surface. All MnO_2/AB samples in this study have a 10 wt% loading amount, so based on these observations, the author expect all of the MnO_2 sheets to be single layers.

SEM images of parent AB and MnO_2/AB composites are shown in Figures 5.2a and 5.2b, respectively. The parent AB shows aggregated particles of around 50-100 nm. On the other hand, the MnO_2/AB

composite is a mixture of AB aggregates and MnO_2 nanosheets. The SEM images suggest that the lateral sizes of the MnO_2 nanosheets are around 100 – 200 nm, and are larger than the primary particle sizes of AB.

The similar composite structure is confirmed by TEM (Figures 5.3a and 5.3b); the composite is a mixture comprised of AB aggregates and MnO_2 nanosheets of weak and uniform contrast. The lateral sizes of MnO_2 nanosheets are several hundred nanometers, and show wrinkles reflecting the flexibility due to the ultrathin nature (0.5 nm in thickness). As seen in the adsorbed structure of the composite, MnO_2 nanosheets do not make intimate contact with AB; it is also inferred by the SEM image which showing distinct MnO_2 sheet edges. For charge transport, it is desirable that active materials make intimate contact to current collectors. While such a MnO_2-coated structure can provide sufficient surface area for charge storage.

5.3.2 Electrochemical characterization

The galvanostatic charge-discharge curve (2nd cycle) of the MnO_2/AB composite is shown in Figure 5.4. The discharge profile is linear in the whole voltage range, as reported by Kadoma *et al*.[19] Despite the same experimental conditions and weight ratio of MnO_2 of the composite (10 wt%), the discharge capacity is more than two times larger than their composite. One difference with their sample is the purity of the MnO_2 nanosheets; the one-pot preparation gives few unexfoliated impurities.[20a] Such a high monosheet ratio should facilitate the electrochemical reaction occurring at the electrode/electrolyte interfaces.

The adsorbed MnO_2 nanosheets will produce the high-surface areas for Li^+ ion adsorption. Here, the composite electrode does not act as a battery, but a capacitor (pseudocapacitor). The capacitor-like behavior of the electrode is confirmed in the linear charge-discharge profiles (Figure 5.4); this characteristic in the discharge curve is similar to other pseudocapacitor electrodes comprised of RuO_2,[6] MnO_2,[4b] Fe_3O_4,[8c] etc. Hence, the author examined specific capacitance, cycling and rate performance of the composite electrode as a pseudocapacitor electrode. Cyclic voltamograms of parent AB and

MnO_2/AB composite at a scan rate of 1 mV s^{-1} are shown in Figure 5.5. For MnO_2/AB, the nearly rectangular CV curve with broad redox peaks centered at 3.2 V (vs Li^+/Li) corresponds to single-electron transfer between Mn^{3+}/Mn^{4+}. The dilated shape without any clear redox peaks corresponds to the non-faradaic adsorption of Li^+ ions at the electric double layer of the MnO_2 surface. The observed CV curve demonstrates that the MnO_2/AB composite is indeed functioning as a pseudocapacitor.

In comparison to the MnO_2/AB composite, the CV area of just the parent AB decreased notably. The calculated capacities based on the total mass of the electrodes are 88 F g^{-1} (MnO_2/AB) and 16 F g^{-1} (parent AB), respectively. This large difference means that the MnO_2 nanosheets exhibit a large specific capacity. The calculated specific capacity (i.e. based on MnO_2 mass, 10 wt%) is 739 F g^{-1}. This value exceeds the theoretical capacitance of MnO_2 calculated based on a one-electron redox reaction (555 F g^{-1}). Again, the origin of such high specific capacitance can be explained as the increase in the electric double layer capacitance due to the high surface area of MnO_2 monosheets (theoretical surface area ~ 980 m^2/g). To the best of my knowledge, the obtained value is the highest among the composites comprised of MnO_2/carbon materials (e.g. MnO_2/CNTs, K_xMnO_2/AB, MnO_2/graphene, etc.).[11,14a,18,22]

Figure 5.6 shows the cycling performance of the MnO_2/AB electrode. The high capacitance of the nanosheets (670 F g^{-1}-MnO_2) still remained after 10 cycles. To achieve higher cycle stability of this composite electrode, enhancement of the structural stability of the MnO_2 framework (via replacing of Mn^{3+} with several tri-valent metal ions, such as Co^{3+}, or Al^{3+}, etc.), or further enhancement of the interaction between the MnO_2 sheets and AB (e.g., hydrothermal treatment of the composite electrode) may be effective.

The rate capability of MnO_2/AB (26 % at 100 mV s^{-1}, and 19 % at 200 mV s^{-1} in terms of capacitance retention) is comparable to that of other MnO_2 pseudocapacitors.[4a,4b,13a,14a,23] As seen in Figure 7, in regard to absolute value of the specific capacitance, our composite electrode displayed a capacitance of 175 F g^{-1} despite at a high scan rate of 100 mV s^{-1}. This value exceeds the specific capacitance of conventional carbon-based supercapacitors (100-120 F g^{-1}) in organic electrolyte with low scan rate.[2] Such results indicate that my composite electrode has a potential as a pseudo capacitor electrode which

can be used in high current density conditions. The reduction in specific capacitance with increasing scan rate may stem from the high charge transfer resistivity of the composite due to loose contact between MnO_2 monosheets and AB surface. To improve the interfacial connection, hydrothermal treatment of the composite electrode or the use of a carbon support with large specific surface area where MnO_2 nanosheets can be adsorbed may be beneficial. The latter is also beneficial to increase the loading amount of MnO_2 nanosheets relating to total capacity of the electrode. Mechanical pressing may also be helpful.

5.4 Conclusions

The author fabricated MnO_2/carbon composite comprised of MnO_2 monosheets and acetylene black (AB) by simply mixing the MnO_2 nanosheet suspension and AB dispersion. The adsorption of MnO_2 monosheets onto the AB was observed by the color change of the supernatant solution from reddish brown to colorless. The XRD of the MnO_2/AB composite only exhibited in-plane reflections of MnO_2 sheet and those originating from AB, which suggests that the MnO_2 nanosheets were adsorbed onto the AB surface as single layer. SEM and TEM measurements showed that the lateral sizes of MnO_2 nanosheets are larger than the sizes of AB aggregates, and the MnO_2 sheets covered the outer surface of the AB aggregates. The electrochemical performance of the MnO_2/AB composite was characterized by an excellent high specific capacitance of 739 F g^{-1}, and such high capacitance remained after 10 cycles. Furthermore, this composite showed 175 F g^{-1} of the specific capacitance at 100 mV s^{-1}, which exceeds that of conventional carbon-based supercapacitor in organic electrolyte. The poor rate capability of this composite electrode can be associated with the poor electronic conductivity.

References

[1] (a) Service, R. F. *Science* **2006**, *313*, 902. (b) Miller, J. R.; Burke, A. F. *Electrochem. Soc. Interf.*, **2008**, *17*, 53.

[2] (a) Simon, P.; Gogotsi, Y. *Nature Mater.* **2008**, *7*, 845. (b) Kötz, R.; Carlen, M. *Electrochimica Acta*, **2000**, *45*, 2483.

[3] Naoi, K.; Simon, P. *Electrochem. Soc. Interface* **2008**, *17*, 34.

[4] (a) Nam, K-W.; Lee,C-W.; Yang, X-Q.; Cho, B. W.; Yoon, W-S.; Kim, K-B. *J. Power Sources* **2009**, *188*, 323. (b) Nam, K-W.; Ma, S-B.; Yoon, W-S.; Yang, X-Q.; Kim, K-B. *Electrochem. Comm.* **2009**, *11*, 1166. (c) Wen, S.; Lee, J-W.; Yeo, I-H.; Park, J.; Mho, S-i. *Electrochim. Acta*. **2004**, *50*, 849. (d) Kim, I-H.; Kim, J-H.; Cho, B-W.; Lee, Y-H.; Kim, K-B. *J. Electrochem. Soc.* **2006**, *153*, A989.

[5] Snook, G. A.; Kao, P.; Best, A. S. *J. Power Sources* **2011**, *196*, 1.

[6] Zheng, J. P.; Cygan, P. J.; Jow, T. R. *J. Electrochem. Soc.* **1995**, *142*, 2699.

[7] (a) Veronica, A.; Bruce, D. *Comp. Rend. Chim.* **2010**, *13*, 130. (b) Grace, W.; Zhong, S. H.; Ling, C. Y.; Subodh G, M.; Madhavi, S. *J. Mater. Chem.* **2010**, *20*, 6720. (c) Winny, D.; Debra R, R.; Bruce, D. *Electrochem. Solid-State Lett.* **2000**, *3*, 457.

[8] (a) Nagarajan, N.; Zhitomirsky, I.; *J. Appl. Electrochem.* **2006**, *36*, 1399. (b) Lokhande, C. D.; Gujar, T. P.; Shinde, V. R.; Mane, R. S.; Han, S-H. *Electrochem. Comm.* **2007**, *9*, 1805. (c) Chen, J.; Huang, K.; Liu, S. *Electrochim. Acta* **2009**, *55*, 1. (d) Santos-Pena, J.; Crosnier, O.; Brousse, T. *Electrochim. Acta* **2010**, *55*, 7511.

[9] (a) Prasad, K. R.; Miura, N.; *Appl. Phys. Lett.* **2004**, *85*, 4199. (b) Meher, S. K.; Justin, P.; Ranga Rao, G. *Appl. Mater. Interfaces* **2011**, *3*, 2063. (c) Nam, K-W.; Kim, K-H.; Lee, E-S.; Yoon, W-S.; Yang, X-Q.; Kim, K-B. *J. Power Sources* **2008**, *182*, 642.

[10] (a) Staiti, P.; Lufrano, F. *J. Power Sources* **2009**, *187*, 284. (b) Dubal, D. P.; Dhawale, D. S.; Salunkhe, R. R.; Lokhande, C. D. *J. Electroanal. Chem.* **2010**, *647*, 60. (c) Yuan, A.; Wang, X.; Wang, Y.; Hu, J. *Energ. Conv. Manage.* **2010**, *51*, 2588. (d) Brousee, T.; Toupin, M.; Dugas, R.; Athouel, L.; Crosnier, O.; Belanger, D. *J. Electrochem. Soc.* **2006**, *153*, A2171.

[11] (a) Lee, H. Y.; Goodenough, J. B. *J. Solid State Chem.* **1999**, *144*, 220. (b) Hu, C-C.; Tsou, T-W. *Electrochem. Comm.* **2002**, *4*, 105. (c) Xiao, W.; Xia, H.; Fuh, J. Y. H.; Lu, L. *J. Power Sources* **2009**, *193*, 935. (d) Bélanger, D.; Brousse, T.; Long, J. W. *Electrochem. Soc. Interface* **2008**, *17*, 49.

[12] (a) Takagi, A.; Watanabe, M.; Hashizume, H.; Yamada, H.; Nakazawa, H. *J. Am. Chem. Soc.* **2003**, *125*, 5479. (b) Ebina, Y.; Sasaki, T.; Harada, M.; Watanabe, M. *Chem. Mater.* **2002**, *14*, 4390. (c) Wang, L.; Takada, K.; Kajiyama, A.; Onoda, M.; Michiue, Y.; Zhang, L.; Watanabe, M.; Sasaki, T. *Chem. Mater.* **2003**, *15*, 4508. (d) Tomko, T.; Rajagopalan, R.; Lanagan, M.; Foley, H. C. *J. Power Sources* **2011**, *196*, 2380.

[13] (a) Yan, J.; Fan, Z.; Wei, T.; Qian, W.; Zhang, M.; Wei, F. *Carbon* **2010**, *48*, 3825. (b) Mishra, A. K.; Ramapr, S. *J. Phys. Chem. C* **2011**, *115*, 14006. (c) Zhao, X.; Johnston, C.; Grant, P. S. *J. Mater. Chem.* **2009**, *19*, 8755. (d) Kim, I-H.; Kim, J-H.; Cho, B-W.; Lee, Y-H.; Kim, K-B. *J. Electrochem. Soc.* **2006**, *153*, A989.

[14] (a) Feng, Z-P.; Li, G-R.; Zhong, H-H.; Wang, Z-L.; Ou, Y-N.; Tong, Y-X. *Electrochem. Comm.* **2009**, *11*, 706. (b) Jiang, J.; Liu, J.; Ding, R.; Zhu, J.; Li, Y.; Hu, A.; Li, X.; Huang, X. *ACS Appl. Mater. Interfaces* **2011**, *3*, 99. (c) Gupta, V.; Kusahara, T.; Toyama, H.; Gupta, S.; Miura, N. *Electrochem. Comm.* **2007**, *9*, 2315.

[15] (a) Yang, G-W.; Xu, C-L.; L, H-L. *Chem. Comm.* **2008**, *48*, 6537. (b) Yu., G.; Hu, L.; Vosgueritchian, M.; Wang, H.; Xie, X.; McDonough, J. R.; Cui, X.; Cui, Y.; Bao, Z. *Nano Lett.* **2011**, *11*, 2905.

[16] (a) Schaak, R. E.; Mallouk, T. E. *Chem. Mater.* **2002**, *14*, 1455. (b) Osada, M.; Sasaki, T. *J. Mater. Chem.* **2009**, *19*, 2503. (c) Ma, R.; Sasaki, T. *Adv. Mater.* **2010**, *22*, 5082.

[17] (a) Fukuda, K.; Saida, T.; Sato, J.; Yonezawa, M.; Takasu, Y.; Sugimoto, W. *Inorg. Chem.* **2010**, *49*, 4391. (b) Sugimoto, W.; Iwata, H.; Yasunaga, Y.; Murakami, Y.; Takasu, Y. *Angew. Chem. Int. Ed.* **2003**, *42*, 4092. (c) Zheng, H.; Tang, F.; Jia, Y.; Wang, L.; Chen, Y.; Lim, M.; Zhang, L.; Lu, G. *Carbon* **2009**, *47*, 1534. (d) Gao, Z.; Wang, J.; Li, Z.; Yang, W.; Wang, B.; Hou, M.; He, Y.; Liu, Q.; Mann, T.; Yang, P.; Zhang, M.; Liu, L. *Chem. Mater.* **2011**, *23*, 3509. (d) Wang, L.; Wang, D.; Dong, X. Y.; Zhang, Z. J.; Pei, X. F.; Chen, X. J.; Chen, B.; Jin, J. *Chem. Comm*. **2011**, *47*, 3556.

[18] Ma, S-B.; Lee, Y-H.; A, K-Y.; Kim, C-M.; O, K-H.; Kima, K-B. *J. Electrochem. Soc.* **2006**, *153*, C27.

[19] Kadoma, Y.; Uchimoto, Y.; Wakihara, M. *J. Phys. Chem. B* **2006**, *110*, 174.

[20] (a) Kai, K.; Yoshida, Y.; Kageyama, H.; Saito, G.; Ishigaki, T.; Furukawa, Y.; Kawamata, J. *J. Am. Chem. Soc.* **2008**, *130*, 15983. (b) Tae, E. L.; Lee, K. E.; Jeong, J. S.; Yoon, K. B. *J. Am. Chem. Soc.* **2008**, *130*, 6534.

[21] Dong, X.; Osada, M.; Ueda, H.; Ebina, Y.; Kotani, Y.; Ono, K.; Ueda, S.; Kobayashi, K.; Takada, K.; Sasaki, T. *Chem. Mater.* **2009**, *21*, 4366.

[22] Xu, C.; Kang, F.; Li, B.; Du, H. *J. Mater. Res.* **2010**, *25*, 1421.

[23] Ma, S-B.; Nam, K-W.; Yoon, W-S.; Yang, X-Q.; Ahn, K-Y.; Oh, K-H.; Kim, K-B. *Electrochem. Comm.* **2007**, *9*, 2807.

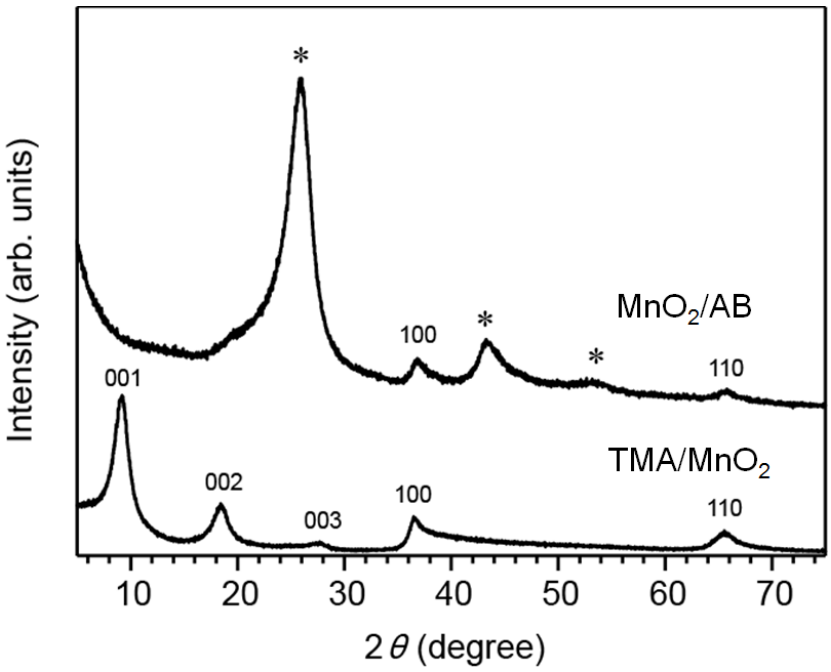

Figure 5.1. XRD patterns of TMA/MnO_2 (stacked sample) and MnO_2/AB composite. Asterisks represent the contribution of acetylene black.

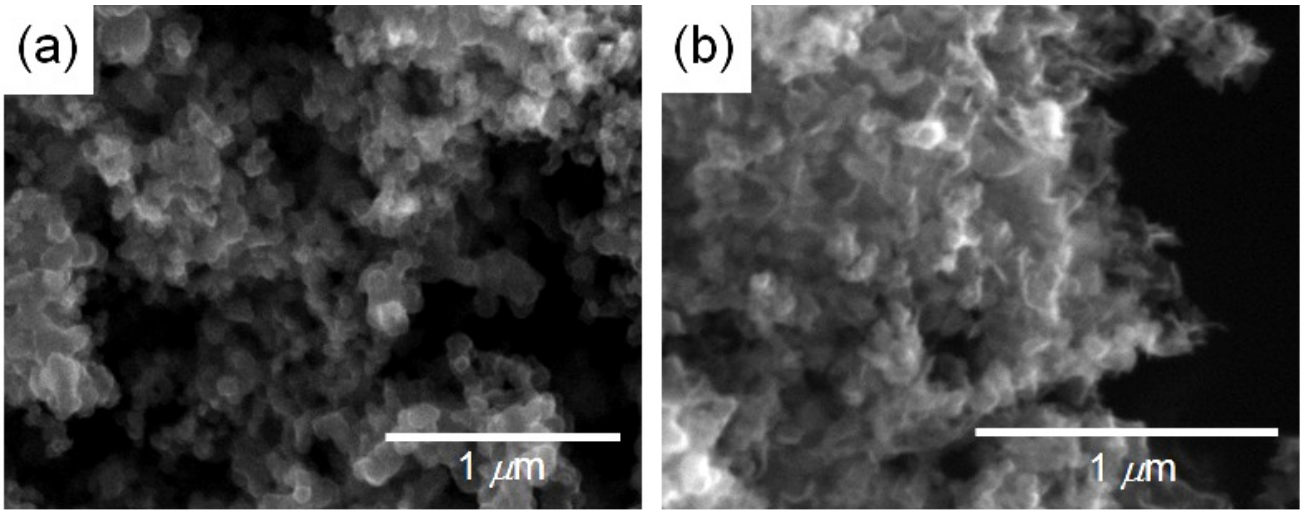

Figure 5.2. SEM images of (a) parent AB, and (b) MnO_2/AB composite.

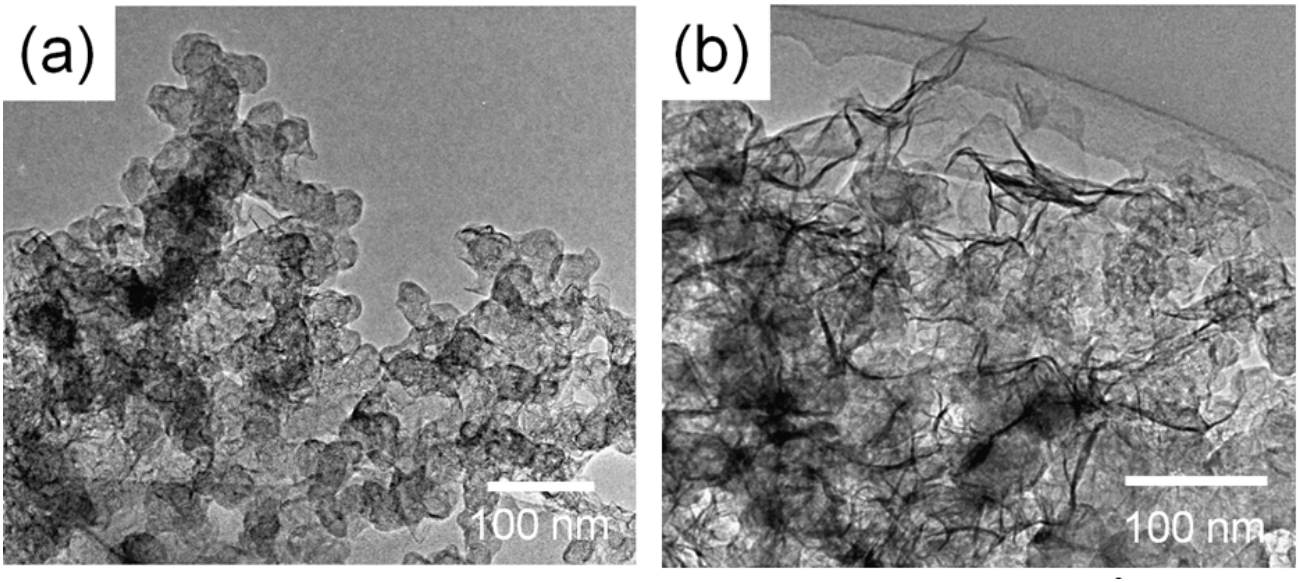

Figure 5.3. TEM images of (a) parent AB, and (b) MnO_2/AB composite.

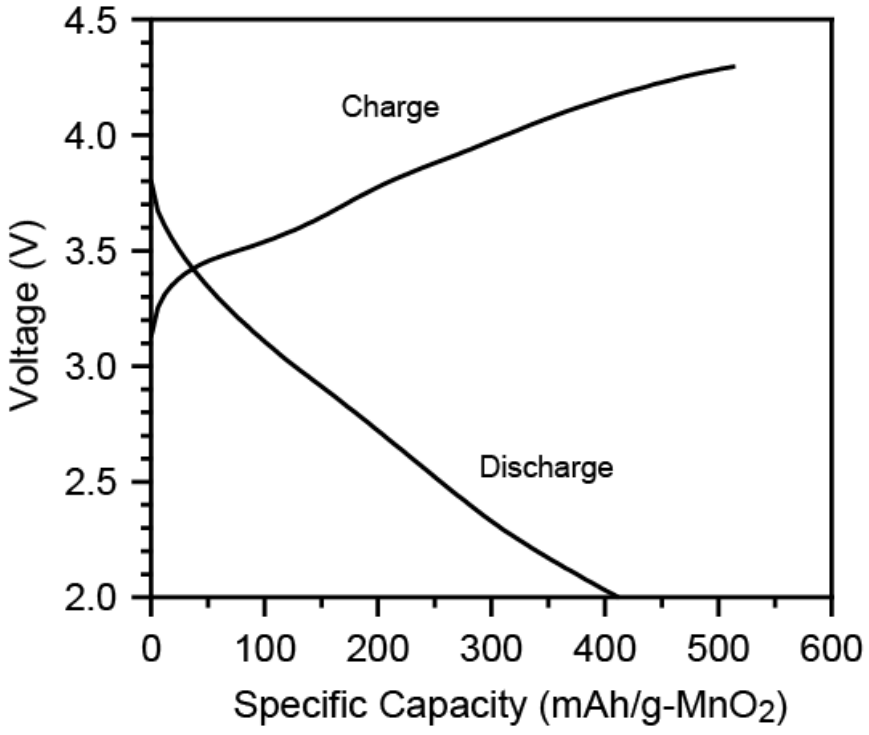

Figure 5.4. Galvanostatic charge-discharge curve (2nd cycle) of MnO_2/AB composite.

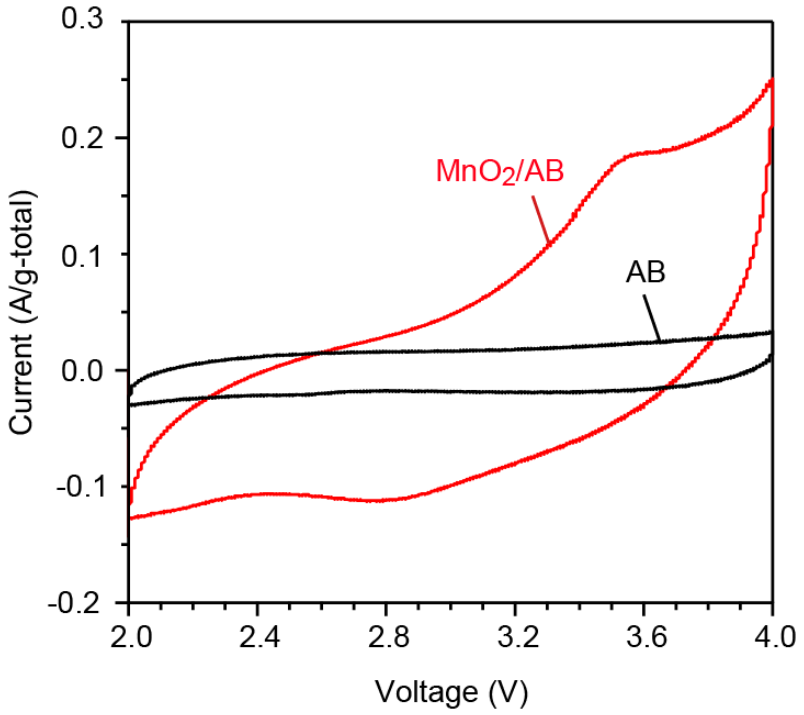

Figure 5.5. Cyclic voltammograms of AB and MnO_2/AB composite at a scan rate of 1 mV/s

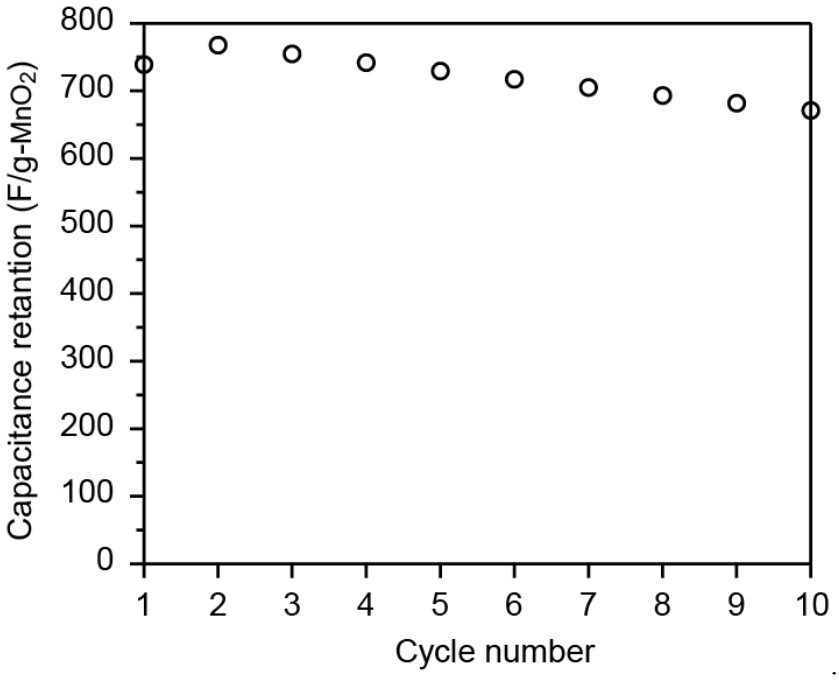

Figure 5.6. Cyclability of MnO_2/AB composite at a scan rate of 1 mV/s.

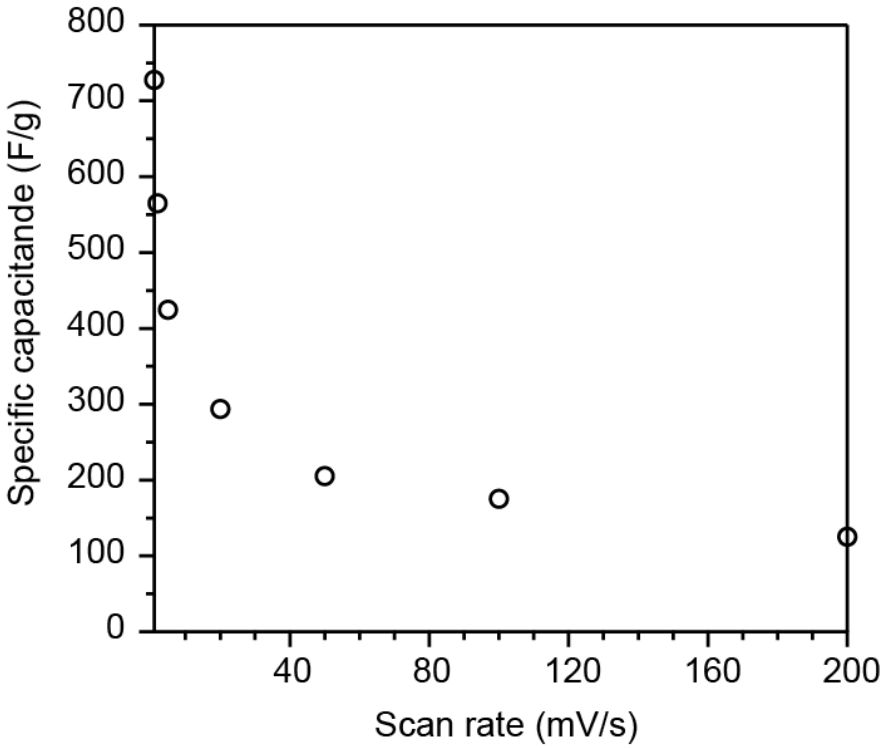

Figure 5.7. Specific capacitance of MnO_2/AB at various scan rates.

General Conclusions

The author explored new bottom-up processes to obtain the MnO_2 nanosheets and applied this method to obtained the layered organic/MnO_2 hybrids, and Co ion doped MnO_2 nanosheets. The author also investigated the application of MnO_2 nanosheets as functional viscoelastic nanocomposite, and high efficient electrode materials.

In Chapter 1, the author explored a novel rapid and facile route to access a colloidal suspension of MnO_2 monosheets in a high yield. Despite the author's single-step approach cuts the processing time to less than a day and eliminates the treatments with the use of special equipment, their structural, spectroscopic, and magnetic properties are comparable to those of the MnO_2 monosheets (or their aggregate) obtained by the conventional multistep processing. Also, the author's processing empowers to fabricate the high-purity organic-inorganic layered hybrids and LB films composed of the MnO_2

monosheets; the electrostatic build-up of these nanostructures possibly allows to explore high-efficient catalysis, electrode, or several functional organic/inorganic hybrids due to its enhanced yield and facility of the synthesis.

In Chapter 2, the author synthesized the $(Mn_{1-x}Co_x)O_2$ nanosheets through an one-pot method using mixed solution consisted of $MnCl_2$ and $CoCl_2$. The cell volumes of these lamellar aggregates showed linier shrinkage upon the Co substitution, in the region of $0 \leq x \leq 0.20$. This is strong evidence of the successful doping of Co into MnO_2 layers up to $x = 0.20$. The substitution effects were observed in UV-Vis spectra and magnetic properties; the optical band gap energies and antiferromagnetic interaction between magnetic ions were increased in related to the shortening of M-O bond length via replace of Mn with Co. The magnetic moments of these lamellar aggregates $K_y(Mn_{1-x}Co_x)O_2 \cdot zH_2O$ are consistent with chemical compositions estimated by EDS, and suggested that the charge density of inorganic layer is inert upon Co-for-Mn substitution. These results agree to the constant average valence of transition metal ions estimated from the chemical compositions of the lamellar aggregates.

In Chapter 3, facile bottom-up one-pot reaction of layered alkyl ammonium/MnO_2 hybrids are attained. This reaction completed within a day and does not require any complex precursors. Unlike previous reports using redox-active organic species or complex Mn precursors, the author's one-pot approach only requires the organic species to be basic and water-soluble. Thus, the author's method is flexible since a range of organic species for intercalation can be added to the reaction mixture. The author have also investigated the formation mechanism of the author's one-pot reaction, and conclude that the following 3 steps are involved: (1) formation and crystal growth of β-Mn(III)OOH, (2) topotactic oxidation of β-MnOOH to form the protonated layered manganese oxide $H_xMnO_2 \cdot yH_2O$, and (3) ion-exchange of interlayer H^+ (or H_3O^+) with *n*-butylammonium and formation of layered C4/MnO_2. Furthermore, solubility of the alkyl amines is important to form the layered alkyl ammonium/MnO_2 hybrids, and an adequate excess of alkyl amine with respect to manganese ions is necessary.

In Chapter 4, the first viscoelastic nanocomposite composed of negatively charged MnO_2 nanosheets are obtained by a room-temperature one-pot process. The nanocomposite can be easily deformed by applying an external stress; for example, mechanical stress gives a free-standing thin film with a thickness of less than 100 nm. It appears that (i) a trimethoxysilyl group and (ii) double long alkyl groups (both for reducing inter-slab interactions) are indispensable for obtaining the viscoelastic nanocomposite in the present system. By the aid of (iii) a quaternized ammonium group (for charge compensation), the present procedure would open up an exploration of new and more versatile viscoelastic nanocomposites composed of negatively charged transition metal oxide nanosheets with a wide variety of metal elements, intralayer structures, and compositions. Specifically, facile fabrication of the shape-deformable nanocomposite with the redox activity would hold great promise for electrochemical devices and catalysts.

In Chapter 5, the MnO_2/carbon composite comprised of MnO_2 monosheets and acetylene black (AB) is fabricated via simply mixing the MnO_2 nanosheet suspension and AB dispersion. The adsorption of MnO_2 monosheets onto the AB was observed by color change of the supernatant solution from reddish brown to colorless. The XRD of the MnO_2/AB composite only exhibited in-plane reflections of MnO_2 sheet and peaks originated from AB, and suggested that the MnO_2 nanosheets were adsorbed onto the AB surface as single-layer. SEM and TEM measurement showed that the lateral sizes of MnO_2 nanosheets are larger than the sizes of AB aggregates, and MnO_2 sheets are covered over the outer surface of AB aggregates. The electrochemical performances of the MnO_2/AB composite were characterized by excellent high specific capacitance of 739 F/g, and such high capacitance was remained after 10 cycles. This composite showed poor rate capability, however, the high capacitance of 175 F/g still remained at a high scan rate of 100 mV/s. The poor rete capability of this composite electrodde can be associated with the poor electronic conductivity.

In summary, the author demonstrated that the simple one-pot procedures can produce the MnO_2 nanosheets and layered organic/MnO_2 hybrids with short reaction times, low temperature and high-yield. The obtained nanosheets and hybrids can utilize as the functional viscoelastic nanocomposite and a charge-storage devices through the construction of appropriate nanostructures. The author believes that such bottom-up approaches are effective for the actual applications, and are applied in high-performance functional materials, such as catalysis, electrodes, porous materials, etc..

List of Publications

Chapter 1

Room-Temperature Synthesis of Manganese Oxide Monosheets

Kazuya Kai, Yukihiro Yoshida, Hiroshi Kageyama, Gunzi Saito, Tetsuo Ishigaki, Yu Furukawa, and Jun Kawamata

J. Am. Chem. Soc. **2008**, *130,* 15938-15943.

Chapter 2

One-Pot Synthesis of Co-Substituted Manganese Oxide Nanosheets and Physical Properties of These Lamellar Aggregates

Kazuya Kai, Marine Cuisinier, Yukihiro Yoshida, Yoji Kobayashi, Hiroshi Kageyama, and Gunzi Saito

in preparation.

Chapter 3

Preparation and Formation Mechanism of a *n*-Butylammonium/MnO2 Layered Hybrid *via* a One-Pot Synthesis under Moderate Condition

Kazuya Kai, Yukihiro Yoshida, Yoji Kobayashi, Hiroshi Kageyama and Gunzi Saito

J. Chem. Soc., Dalton Trans. **2011**, doi: 10.1039/C1DT11145K

Chapter 4

Shape Deformable Nanocomposite Composed of Manganese Oxide Nanosheets

Yukihiro Yoshida, Kazuya Kai, Hiroshi Kageyama and Gunzi Saito

J. Mater. Chem. **2011**, *21,* 5863-5866.

Chapter 5

Electrochemical Characterization of Single-Layer MnO_2 Nanosheets as a High-Capacitance Pseudocapacitor Electrode

Kazuya Kai, Yoji Kobayashi, Yuki Yamada, Kohei Miyazaki, Takeshi Abe, Yoshiharu Uchimoto, and Hiroshi Kageyama

In preparation

The following papers are not included in this thesis

Spectroscopic Studies of Hybrid Thin Films Consisting of a Clay Tetrathiafulvalene

Ryuichi Seike, Nozomi Okawahara, Yu Furukawa, Jun Kawamata, Kazuya Kai, Yukihiro Yoshida, and Gunzi Saito

Clay Sci. Soc. Jap., Clay Sci. **2008**, *13*, 199-204.

Room-Temperature Single-Step Synthesis of MnO_2 Nanosheets

Kazuya Kai, Yukihiro Yoshida, Hiroshi Kageyama, Gunzi Saito, Tetsuo Ishigaki, and Jun Kawamata

Low Temp. & Mater. Sci. Kyoto Univ. **2009**, *14*, 19-27.

Viscoelastic Nanocomposite Composed of Titania Nanosheets: Multiple Conductometric Sensitivities

Yukihiro Yoshida, Kazuya Kai, Hiroshi Kageyama, and Gunzi Saito

J. Chem. Soc., Dalton Trans. **2011**, *40*, 7291-7294.